Snow–Atmosphere Exchange in Complex Terrain: Turbulent and Advective Controls on Snow Sublimation and Surface Energy Fluxes

Eli Schwat

A dissertation
submitted in partial fulfillment of the
requirements for the degree of

Doctor of Philosophy

University of Washington

2025

Reading Committee:

Jessica Lundquist, Chair

Elie Bou-Zeid

Michelle DiBenedetto

Program Authorized to Offer Degree:
Civil and Environmental Engineering

University of Washington

Abstract

Snow–Atmosphere Exchange in Complex Terrain: Turbulent and Advective Controls on Snow Sublimation and Surface Energy Fluxes

Eli Schwat

Chair of the Supervisory Committee:
Jessica Lundquist
Civil and Environmental Engineering

This dissertation examines turbulent and advective processes controlling the snow-atmosphere exchange of water vapor, heat, momentum, and turbulent kinetic energy (TKE) in the mountainous East River Valley of Colorado. We used measurements spanning spatial and temporal scales, from eddy covariance point measurements to Doppler lidar measurements of wind fields that span the width of a mountain valley.

For Chapter 2, we measured snow sublimation and found that 10% of the seasonal snowpack is lost to the process. We also found that sublimation of suspended, blowing snow induced positive water vapor flux divergence, and, as a result, sublimation estimates are sensitive to instrument deployment height. By quantifying sublimation in a Colorado River headwater catchment, we addressed sublimation's potential role in declining streamflow efficiency. While models suggest sublimation removes 20–40% of snowpack, our observations indicated it removes less, although future measurement campaigns should investigate sublimation rates above forests and on exposed ridges. To future field campaigns, we suggest that eddy covariance systems should be deployed near the top of the blowing snow layer, which was around 10 m at our field site.

For Chapter 3, we measured strong wind shear at the tops of mountain ridges and the occasional formation of rotors and vortices in the lee of a prominent ridge. During these

highly turbulent events, TKE propagated down into the valley, and near-surface mixing and sublimation rates increased. Surface fluxes during these events were under-predicted by Monin-Obukhov similarity theory, the predominant method for predicting surface fluxes in weather and land surface models. Our observations suggested that similarity theory fails to predict surface fluxes in complex terrain because the theory assumes that the near-surface TKE budget involves only shear and bouyancy. In complex terrain, TKE transport can be an important term in the near-surface TKE budget. Additionally, we found that eddies transporting TKE also carried upper-atmosphere dry air to the surface. This finding indicates that future surface flux parameterizations should account for non-local exchange in complex terrain.

For Chapter 4, we estimated the full surface energy balance over isolated patches of snow. We used an infrared video camera to estimate horizontal sensible heat advection, an eddy covariance system to measure vertical heat fluxes, a scanning lidar to quantify snow melt, and a radiometer to measure radiative fluxes. We found that once the fractional snow-covered area fell below $\sim$50%, horizontal heat advection supplied $\sim$50% of the energy consumed by melting snow. This result suggests that advective processes should be incorporated into snowmelt models and motivates further investigation into whether advection influences snowpack disappearance and streamflow timing. Our field measurements of sensible heat advection also diverged from the predictions of an idealized model, potentially reflecting the geometry of the observed snow patch. Future studies should therefore aim to measure sensible heat advection over snow patches situated within the complex and often concave landforms where they typically persist.

TABLE OF CONTENTS

LIST OF FIGURES

LIST OF TABLES

ACKNOWLEDGMENTS

First, I would like to thank all of the professors and scientists that have mentored me over the past 5 years. When I first came to UW for my master's degree, I was advised by Drs. Erkan Istanbulluoglu and Alexander Horner-Devine, who were always exceptionally kind to me, and continue to advise me today. Their personalities and interesting science are the reason I came to UW. After completing my master's degree, when I joined the Sublimation of Snow project, I was lucky to meet a number of scientists outside of UW, who have had a big impact on my research and my professional development. In particular, I would like to thank Dr. Ethan Gutmann, whose science and whimsical manner has inspired me. Finally, thank you to my advisor Dr. Jessica Lundquist, whose excitement and enthusiasm for science and field work is infectious. I knew I wanted to work with Dr. Lundquist when she described her Sublimation of Snow project to me, and then immediately sent me a review paper about ocean spray. Apparently blowing snow and ocean spray have a lot of similarities. It was this cross-disciplinary thinking, and this appreciation for physics and math that underpin all science, that brought me into Dr. Lundquist's Mountain Hydrology lab. I suppose the offer to spend two months on skis (for science!) also helped. Working with Dr. Lundquist has opened up many unique opportunities for me. I am extremely grateful.

I would also like to thank the numerous student groups at UW who have supported me throughout the past 5.5 years. Thank you to the Environmental Fluid Mechanics group, with whom I emerged from the Covid pandemic and spent many Thursday nights at Big Time. Thank you to the Mountain Hydrology group, with whom I've ran, biked, skied, barbecued, baked pizzas, roadtripped, and purchased Goodwill sport coats. All of the students in these groups are exceptional human beings, and I am lucky to have met them all.

Finally, I thank my family. Mom and Dad, thank you for supporting me. Holidays are always the highlight of my year, and that is due to your efforts and success in bringing family together. As a teenager, you inspired me to be a good student. Perhaps, I've been too good a student, or at least a student for too long. Thank you to Herbie and Ruby, for being the only siblings I will ever have. Excellent job. Finally, to Cayenne and Gilly. Cayenne, you have seen the best of me and the worst of me, your love has never wavered, and you even seem interested in the plots I make at 11pm on the couch. Gilly, for me, you have only infinite love and eternal forgiveness. I owe you a lot of good, long walks.

Chapter 1

INTRODUCTION

1.1 Background

Around the world, alpine snow serves as a key source of freshwater and an essential part of regional water supplies. Understanding the role of alpine snow in the water balance is critical. However, there are many challenges to measuring and modeling alpine snow, some of which are related to a lack of understanding about fluxes of water vapor, heat, and momentum in the atmospheric boundary layer (ABL), the lowest portion of the atmosphere that interacts with the earth's surface. Fluxes are especially difficult to measure and model in the ABL over mountains, which are also referred to as "complex terrain". It is those fluxes in complex terrain — the exchange of mass and energy between the earth's surface and the atmosphere — that we will focus on in this dissertation.

Water vapor fluxes Sublimation of snow — the phase change between ice and water vapor — represents the largest source of uncertainty in snow hydrology models apart from precipitation inputs [*Slater et al.*, 2001; *Xia et al.*, 2017]. Estimates of sublimation as a portion of winter snowfall range from less than 1% to more than 50% [*Mott et al.*, 2018; *Svoma*, 2016]. Understanding how much of the snowpack is lost to sublimation is critical to understanding how much snow-water is available in natural and human-inhabited watersheds.

Sensible heat fluxes Understanding sensible heat fluxes, the exchange of heat (temperature), is also critical to better understanding water resources. Sensible heat fluxes determine how the earth's surface warms the atmosphere, and the opposite, how the atmosphere warms the earth's surface. The temperature of the earth's surface determines how much sublimation

and snow melt can occur, both critical processes in the alpine water balance.

Momentum fluxes Understanding momentum fluxes in complex terrain is also essential for understanding the movement of water between the earth's surface and atmosphere. Momentum fluxes control the speed and direction of winds, and winds control how the state of the ABL evolves. The state of the ABL can, in turn, influence surface temperatures, surface sublimation rates, and precipitation processes [*Kötsche et al.*, 2025]. In numerical weather models, coarse resolutions mean that modeled winds often do not match observed winds [*Adler et al.*, 2023]. But even when specialized, high resolution models accurately reproduce complex flow phenomena in mountains [e.g. *Rotach et al.*, 2008; *Weigel and Rotach*, 2004; *Weigel et al.*, 2007], interactions between the flow phenomena and the surface are not modeled, because surface fluxes are modeled using a first-order turbulence closure (Monin-Obukhov Similarity Theory) that relates turbulent fluxes to mean, near-surface gradients of velocity, temperature, and humidity.

Challenges to modeling fluxes in complex terrain Uncertainty about water vapor, heat, and momentum fluxes in alpine catchments stems, in part, from challenges to modeling fluxes. The predominant theory for predicting fluxes at the earth's surface, Monin-Obukhov Similarity Theory (MOST), makes a number of assumptions that are violated in alpine catchments, including that the landscape is flat and that the surface is horizontally homogenous. Despite attempts to provide suitable alternative parameterizations [*Stiperski and Calaf*, 2023; *Cox et al.*, in review], MOST is still used to estimate surface fluxes and published model results estimating sublimation rates and other fluxes are uncertain (Sexstone et al., 2018; Xiao et al., 2018; Strasser et al., 2008).

Fluxes over snow are also difficult to parameterize because the ABL over snow is most often stable — the surface is colder than the air above it. During stable conditions, models can produce an unrealistic stability feedback, whereby radiative cooling of the snow surface at night increases stability, decreases turbulent exchange, which further increases stability [*Lapo*

et al., 2019]. In the real world, turbulent energy generated by waves and other sub-mesoscale motions stops the ABL from becoming increasingly stable, although these motions are not well represented in models [*Sun et al.*, 2012]. While some strategies have been invented to avoid the stability feedback in land surface models, such as setting a minimum wind speed [*Andreas et al.*, 2010], inaccurate sensible heat fluxes are still associated with widespread bias in surface temperatures [*Slater et al.*, 2001] and air temperatures [*Lapo et al.*, 2019] predicted by land surface models. These model issues further preclude accurate estimates of near-surface humidity and wind speed, which control water vapor and momentum fluxes.

Fluxes in complex terrain are also difficult to parameterize because we do not completely understand the flow phenomena that result from the interaction between synoptic winds and complex topography, nor do we understand how those interactions may exert control on fluxes at the surface. At the global scale, models have exhibited a "westerly bias", too strong and too westerly surface winds. Although this bias has been addressed by implementing so-called "gravity wave drag parameterizations", which increase drag on the atmosphere over mountain ranges, the exact mechanisms that result in increased drag are not understood [*Rotach et al.*, 2015]. While the influence of complex terrain on momentum transport has been confirmed, its influence on the exchange of heat and water vapor is only beginning to be understood [*Rotach et al.*, 2015]. In recent decades, new instruments have provided high resolution, two-dimensional observations of flow phenomena that control momentum and surface heat exchange, including mountain waves, recirculating flows, and turbulent wakes [*Turnipseed et al.*, 2004; *Litt et al.*, 2015; *Lehner et al.*, 2019].

Challenges to measuring fluxes in complex terrain In the face of model uncertainty, researchers generally turn to eddy covariance (EC) measurements of surface fluxes. Unfortunately, EC systems are expensive, deploying them is logistically challenging, and, as a result, EC measurements in alpine catchments are rare. Even when ECs are deployed, their placement at standard measurement heights of 2–5 meters may not accurately measure surface fluxes, particularly when fluxes in the surface layer vary with height ("vertical

flux divergence"). Vertical flux divergence is common over snow and ice covered complex terrain [*Grachev et al.*, 2016; *Peltola et al.*, 2021; *Mahrt et al.*, 2018] and can result from a number of atmospheric phenomena, including very stable conditions, blowing snow sublimation, sub-mesoscale (valley-scale) motions, and lateral and vertical advection. To most accurately estimate surface fluxes, EC measurements at multiple heights above the surface may be required, and additional observations are necessary to identify the causes of vertical flux divergence. For example, blowing snow sensors can positively identify blowing snow conditions [*Trouvilliez et al.*, 2015] and Doppler wind lidars can identify sub-mesoscale flows [*Lehner et al.*, 2019]. In the case of horizontal heterogeneity, such as near a transition from forest to prairie or in the presence of melting, patchy snow, a single measurement tower may not suffice for estimating surface fluxes. In such a case, horizontal gradients in humidity and temperature result in large lateral advection of water vapor and heat, which requires multiple horizontally distributed towers to quantify [*Harder et al.*, 2017; *Granger et al.*, 2006; *Kochendorfer and Paw U*, 2011; *Lee*, 1998; *Paw U et al.*, 2000; *Mott et al.*, 2011].

In summary, our ability to predict near-surface fluxes of water vapor, heat, and momentum in snow-covered complex terrain is hampered by imperfect models and a lack of measurements. To improve our process understanding, we require coincident, spatially distributed observations, from eddy covariance towers measuring fluxes at the plot scale to radars and lidars measuring atmospheric flow at the valley scale. While such observations are critical for improving numerical weather and land surface models, they are also critical for improving our understanding of the water cycle. To improve our understanding of hydrology, we must understand fluxes between the earth's surface and the ABL.

1.2 Motivation and Observations

To better understand surface fluxes in complex mountain terrain, we draw on observations from three coordinated field campaigns that operated between 2021–2023 in Colorado's East River Valley: the Sublimation of Snow (SOS) campaign, the Surface Atmospheric Integrated Field Laboratory (SAIL), and the Study of Precipitation, the Lower Atmosphere, and Sur-

face for Hydrometeorology (SPLASH) [*Lundquist et al.*, 2024; *Feldman et al.*, 2023; *Boer et al.*, 2023]. These efforts were motivated in part by the importance and uncertainty of snow-based water resources in the Colorado River Basin, which supplies water to roughly 40 million people and 2.2 million hectares of farmland [*Tillman et al.*, 2022]. High-elevation snowpacks, such as those in the East River Valley, generate about 70% of the basin's total streamflow. Since the onset of the ongoing Millennium Drought in 2000, however, streamflow has declined more sharply than precipitation alone would suggest, pointing to shifts in post-snowfall hydrological processes that reduce streamflow efficiency [*Hogan and Lundquist*, 2024]. Against this backdrop, the SOS, SAIL, and SPLASH campaigns jointly deployed a rich network of instruments, including more than four surface meteorology and flux stations (some with vertically stacked eddy covariance systems), radars, Doppler wind lidars, blowing snow flux sensors, and many other specialized instruments. Together, these observations offer the level of spatial and temporal detail needed to probe the processes that control surface–atmosphere exchange in mountain environments.

1.3 Outline

We used measurements from the three field campaigns to complete three research objectives, which are organized into three chapters, Chapters 2–4, outlined below. In Chapter 5, we conclude this dissertation by summarizing the objectives completed in Chapters 2–4 and discussing the broader impacts of the work, open questions, and future areas for research.

Chapter 2 *Estimating snow sublimation in complex terrain: A season of intensive field measurements and the role of vertical water vapor flux divergence.*

- **Objective**: Measure sublimation rates throughout a single winter season, examine why measured sublimation rates vary with instrument height, and recommend the minimum instrumentation necessary to accurately measure sublimation rates in complex terrain.

- This work was published in *Journal of Hydrometeorology* and is reproduced from the following citation.

Schwat, E., Hogan, D., Paw U, K. T., Cox, C. J., Butterworth, B. J., Gutmann, E., Vano, J. A., and Lundquist, J. D. (2025). Estimating snow sublimation in complex terrain: A season of intensive field measurements and the role of vertical water vapor flux divergence. Journal of Hydrometeorology. https://doi.org/10.1175/JHM-D-25-0022.1

Chapter 3 *Elevated shear layers and top-down turbulence increase surface-atmosphere exchange in snow-covered complex terrain.*

- **Objective**: Examine when and how sub-mesoscale orographic flows control near-surface turbulent exchange over snow and lead to errors in modeled surface fluxes.

- This chapter is in preparation for submission to the *Journal of Geophysical Research: Atmospheres*.

  Schwat, E., Hogan, D., Gutmann, E., Cox, C., Adler, B., Feldman, D.R., and Lundquist, J. D. Elevated shear layers and top-down turbulence increase surface-atmosphere exchange in snow-covered complex terrain.

Chapter 4 *Measuring sensible heat advection over patchy, melting snow: Beyond point measurements.*

- **Objective**: Investigate the magnitude of sensible heat advection during the melt season when snow becomes patchy, and estimate the contribution of advection to snow melt.

- This chapter is in preparation for submission to *The Cryosphere*.

  Schwat, E., Haugeneder, M., Hogan, D., Gutmann, E., and Lundquist, J. D. Measuring sensible heat advection over patchy, melting snow: Beyond point measurements.

Chapter 2

ESTIMATING SNOW SUBLIMATION IN COMPLEX TERRAIN: A SEASON OF INTENSIVE FIELD MEASUREMENTS AND THE ROLE OF VERTICAL WATER VAPOR FLUX DIVERGENCE

2.1 Introduction

Understanding the role of snow sublimation in the mountain water balance is critical to understanding water resources, as sublimation represents a net loss of water from snowpack "reservoirs." Uncertainty about sublimation-related water loss is of particular concern in the Colorado River Basin, which supplies water to 40 million people and 2.2 million hectares of irrigated land [*Tillman et al.*, 2022] and has experienced a 19% decrease in naturalized streamflow despite near-constant precipitation over the last century [*Udall and Overpeck*, 2017]. Yet, estimates of seasonal sublimation in seasonally snow-covered regions vary widely, from 0.6–60% as a percentage of total winter snowfall [*Mott et al.*, 2018; *Svoma*, 2016].

Snow sublimation is generally estimated by the bulk aerodynamic or eddy covariance (EC) methods [*Svoma*, 2016; *Reba et al.*, 2012], though both methods have limitations in the snowy, complex terrain where significant water resources reside [e.g. high elevation snow generates about 70% of Colorado River streamflow, *Christensen et al.*, 2004]. Bulk aerodynamic methods are highly sensitive surface roughness parameterizations [*Reba et al.*, 2014] and may be unreliable in complex terrain [*Stiperski and Calaf*, 2023].

In place of bulk aerodynamic methods, the EC method is used to measure sublimation, but deployments in snowy, complex terrain are rare and the underlying assumptions of the EC method may not apply. Blowing snow, highly stable conditions, drainage winds, and other sub-mesoscale (e.g. valley-scale) motions may cause fluxes to vary vertically (vertical

turbulent flux divergence), which means that an EC instrument may measure different fluxes depending on its height above the surface [*Sigmund et al.*, 2022; *Grachev et al.*, 2016; *Peltola et al.*, 2021; *Mahrt et al.*, 2018]. The possibility of vertical turbulent flux divergence (VTFD) implies that deploying one EC instrument, the standard for sublimation studies [e.g. *Reba et al.*, 2012; *Sexstone et al.*, 2016] may not accurately measure sublimation. Additionally, if advection of water vapor is significant, EC instruments are insufficient for measuring total sublimation, and should be accompanied by spatially distributed instruments that can measure horizontal and vertical humidity gradients [*Lee*, 1998; *Harder et al.*, 2017]. Previous field studies have observed horizontal advection of water vapor across vegetation boundaries [*Kochendorfer and Paw U*, 2011; *Wang et al.*, 2024] and over patchy snow [*Harder et al.*, 2017], although no studies, to the best of our knowledge, have measured advection over contiguous snow cover in complex terrain, where vertical advection may arise due to horizontal flow convergence and horizontal advection may arise due to drainage winds [*Paw U et al.*, 2000]. In general, the impacts of advective processes on turbulent flux measurements in complex terrain remain understudied [*Stiperski and Rotach*, 2016].

Additionally, while blowing snow sublimation has been identified as an important mechanism for water vapor exchange in Antarctica [*Sigmund et al.*, 2022] and Canadian prairies [*Pomeroy and Essery*, 1999], instruments that directly observe blowing snow have only rarely been deployed in seasonally snow-covered complex terrain [mostly in the European Alps and Canadian Rockies, e.g. *Vionnet et al.*, 2013; *Trouvilliez et al.*, 2015; *Xie et al.*, 2023; *Aksamit and Pomeroy*, 2016, 2017, 2018] and even more rarely in tandem with EC flux instruments (*Pomeroy and Essery*). The importance of blowing snow sublimation for the mountain water balance in the Western US remains an open question.

Between November 2022 and June 2023, the Sublimation of Snow (SOS) campaign deployed four instrument towers with EC and blowing snow sensors in the Rocky Mountains, CO, USA. Initial findings indicate that the largest sublimation rates coincided with the largest blowing snow fluxes, and that EC water vapor fluxes vary with instrument height [*Lundquist et al.*, 2024]. In this study, we utilize SOS measurements to estimate sublimation

and examine the occurrence of and relationships between VTFD, blowing snow, and moisture advection, in order to answer the following research questions:

1. How and why do sublimation rates vary in time (throughout the winter season, during blowing snow conditions)?

2. How and why do EC water vapor fluxes vary horizontally and vertically in space?

3. What instrumentation is necessary to accurately estimate sublimation in complex terrain?

In the following, we first introduce the SOS campaign study site and instrumentation. We then discuss our methods, including how we process turbulence measurements and estimate moisture advection. We then present our results, including an overview of sublimation rates and surface conditions throughout the winter season, a comparison of spatially distributed EC water vapor fluxes, and estimates of water vapor advection.

2.2 Study site

The Sublimation of Snow (SOS) campaign deployed over 100 instruments at Kettle Ponds (elevation 2861 m), a shallowly sloping site ($\sim$3°) in the center of the mountainous East River Valley, a tributary of the upper Colorado River (Figure 2.1a) [*Lundquist et al.*, 2024].

Kettle Ponds is on the valley floor, among one meter high rolling topography (Figure 2.1b), adjacent to a v-shaped canyon containing the East River (Figure 2.1d). Only 1-meter-tall bushes grow within approximately 200 meters of the site, and snow mostly buries them during the snow season (Figure 2.1e, f).

Four hundred meters downvalley of Kettle Ponds ("Annex" site, Figure 2.1a, d, f), the Study of Precipitation, the Lower Atmosphere and Surface for Hydrometeorology (SPLASH) campaign operated a flux and micrometeorological tower during the same period as the SOS

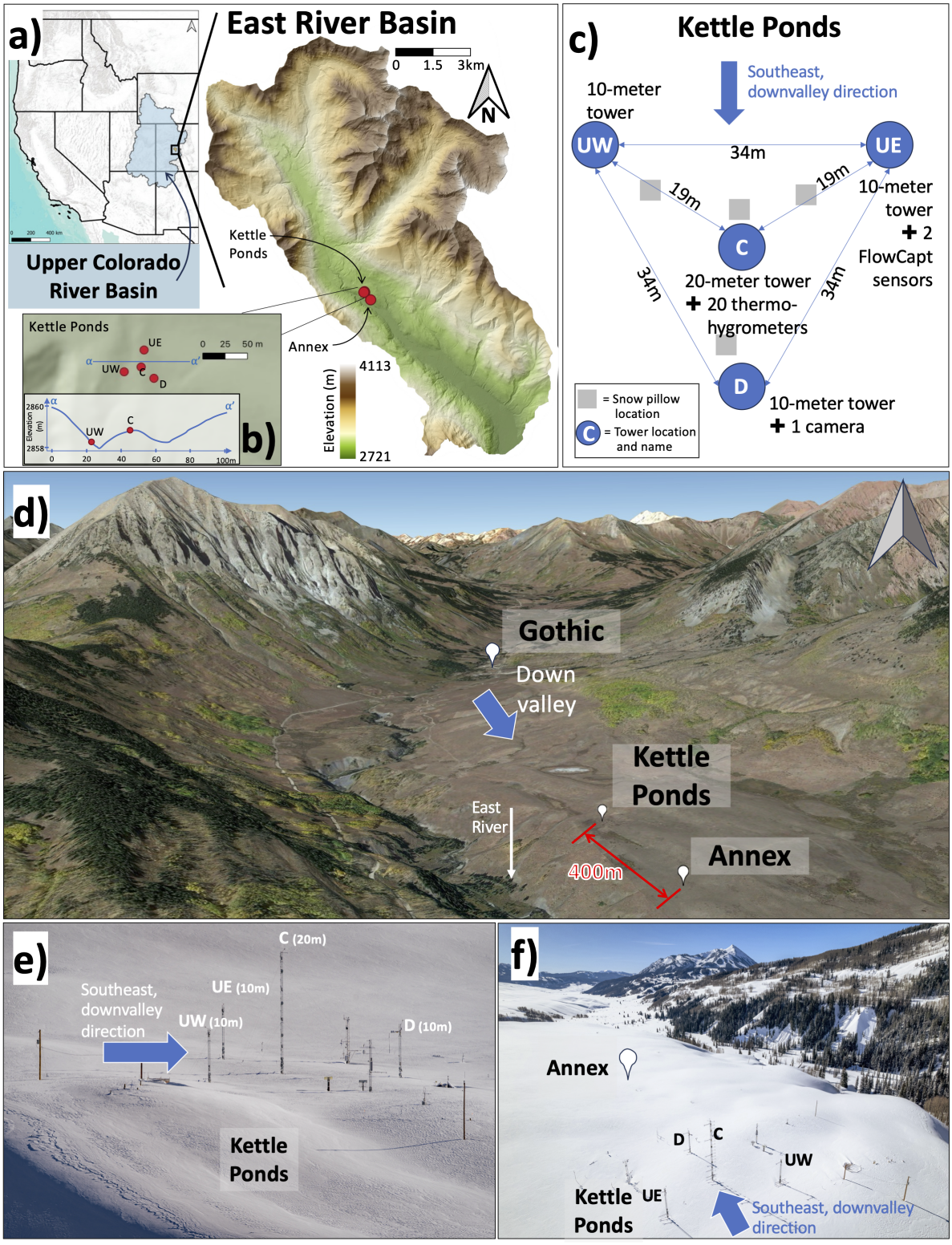

Figure 2.1: *Caption on next page.*

Figure 2.1: a) Location of the Kettle Ponds and Annex field sites. Hillshade and elevation from a 3-meter digital elevation model (DEM) [*Wainwright and Williams*, 2017]. b) Close up of the DEM at Kettle Ponds. Red dots mark the instrument tower locations. The inset plot shows an elevation transect illustrating 1-meter high rolling topography among the towers. c) Orientation of the towers deployed at Kettle Ponds for the Sublimation of Snow campaign [*Lundquist et al.*, 2024]. *Tower C* had 7 eddy covariance instruments; *towers UW, UE,* and *D* each had 3. d) Google Earth rendering of the East River valley (Images from 2019-10-2, Landsat/Copernicus, copyright 2024 Maxar Technologies). e) and f) Winter-time imagery of the sites, courtesy of Jeremy Snyder.

campaign [*Boer et al.*, 2023; *Cox et al.*, 2025b]. The Surface Atmosphere Integrated Field Laboratory (SAIL) campaign [*Feldman et al.*, 2023] also coincided with the SOS campaign.

2.2.1 Instrumentation

Four towers were raised at Kettle Ponds, arranged in a triangle, with one 20-meter tower in the center and three 10-meter towers at each corner (Figure 2.1c) [*UCAR/NCAR-Earth Observing Laboratory*, 1990; *Lundquist et al.*, 2024]. Towers are named by location, with *tower UW* indicating its upvalley-west location, *UE* upvalley-east, *C* for center, and *D* for downvalley. Winds blow predominantly down-valley (winds from 292–342°, 49% of time) and upvalley (winds from 92-152°, 24% of time). Nearby power lines provided electricity for all instruments.

EC instruments, comprised of a CSAT3 sonic anemometer and an EC150 open-path infrared gas analyzer (IRGA), were placed at 1, 3, and 10 meters above ground level (AGL) on *towers UW, UE*, and *D*, and at heights 1, 2, 3, 5, 10, 15, and 20 meters AGL on *tower C* (Table 2.1). Temperature and relative humidity (T, RH) sensors were placed at one meter intervals between 1–20 meters on *tower C*. Two FlowCapt FC4 blowing snow flux

Table 2.1: Instruments deployed for the Sublimation of Snow (SOS) campaign and utilized in this work. All SOS instruments are deployed at Kettle Ponds (Figure 2.1). For a full description of all instruments deployed, see *Lundquist et al.* [2024].

Instrument Name	Model	Measurement	Tower (see Figure 2.1), instrument heights
Eddy covariance, a 3D sonic anemometer and an open-path infrared gas analyzer (IRGA)	Campbell Scientific CSAT3 and EC150	Water vapor flux ($\overline{w'\rho_v'}$), sensible heat flux ($\overline{w'T'}$), 3-D wind speed ($\langle u, v, w \rangle$)	c: 2, 3, 5, 10, 15, 20 meters; D, UW, and UE: 3, 10 meters
Thermohygrometer	Sensirion SHT85 + fan	Air temperature (T), relative humidity (RH), and water vapor mixing ratio (σ) using nanobarometer P	c: 2-20 meters, every 1 meter
Nanobarometer	Paroscientific 6000	Pressure (P), allows calculation of potential temperature, saturation mixing ratio	c: 10 meters
Pyranometer and pyrgeometer (heated)	Kipp and Zonen CM21 and CG4	Upwelling and downwelling shortwave and longwave radiation	d: 9 meters
Infrared radiometers	Apogee SIF-III	Upwelling longwave radiation (8 - 14 μm), to infer surface temperature (T_s) and surface water vapor mixing ratio (σ_0) assuming saturation at the snow surface. Sensors were mounted pointing at 45° from nadir, upvalley.	c: 3 meters
Acoustic blowing snow sensor	ISAW FlowCapt FC4	Horizontal blowing snow fluxes. Any time period with a blowing snow flux measurement greater than zero is classified as blowing snow. The smallest flux the instrument can measure is 0.001 g/m^2/s [*Trouvilliez et al.*, 2015].	UE: 0-1 and 1-2 meters (sensors are one meter long tubes)
Web camera	Microseven M7B5MP Ultra HD	Photographs, hourly	d: 4.5 meters

sensors were on *tower UE* between 0–1 and 1–2 meters. We measured snow depth at the site using a scanning lidar [*Lundquist et al.*, 2024]. During the 2022-2023 winter, the snowpack at Kettle Ponds reached a maximum depth of 1.55 meters in late March and instruments placd at one meter AGL were intermittently buried. We exclude 1-meter EC measurements from our analysis and only utilize 1-meter T/RH measurements when those instruments were not buried. No instruments used in this study were moved during the campaign and measurements referenced by their height (e.g., the 3-meter EC) refer to their height AGL even though their position relative to the snow surface varied. Instruments made nearly continuous measurements during their deployment (November 2022 to June 2023), with a max outage length of two days (22–23 April 2023) due to power loss.

2.2.2 Time period

We used data only from the "snow-on season," defined as the period of continuous snow cover beneath all four towers, to avoid measuring ground evaporation and flux errors due to patchy snow [*Haugeneder et al.*, 2024; *Harder et al.*, 2017]. Hourly photographs indicate this period lasted from 30 November 2022 to 8 May 2023.

2.3 Methods

2.3.1 Blowing snow measurements

Two FlowCapt FC4 sensors measured blowing snow fluxes between 0–1 and 1–2 meters AGL (Table 2.1). When partially buried, the sensors still work because they detect the acoustic signal produced by a snowflake hitting the sensor [*Chritin et al.*, 1999]. To investigate the relationship between blowing snow and sublimation, we labeled all 30-minute periods as during (or not during) blowing snow, identified by a mean blowing snow flux greater than (equal to) zero.

2.3.2 Micrometeorological measurements

To describe weather conditions at the site, we utilized the vertical profile of 20 T/RH sensors, Apogee radiometer measurements of snow surface temperature [T_s, assuming snow emmisivity of 0.99, *Andreas et al.*, 2004], net shortwave and longwave radiometer measurements of net radiation ($R_n = SW_{in} - SW_{out} + LW_{in} - LW_{out}$), and nanobarometer measurements of pressure, P (Table 2.1). RH measurements were bias-corrected based on post-calibrations performed in a humidity chamber after the end of the field campaign [*NSF NCAR/EOL ISFS Team*, 2024]. To estimate water vapor advection (Section 2.3.2.3.4), we calculated absolute humidity (ρ_v) from RH, P, and T [*Wallace and Hobbs*, 2006].

2.3.3 Eddy covariance measurements

For this study, we utilized EC measurements of mean wind speed ($\langle \overline{u}, \overline{v}, \overline{w} \rangle$), covariance water vapor flux ($\overline{w'\rho_v'}$), and covariance sensible heat flux ($\overline{w'T'}$) from all ECs at and above two meters (Table 2.1). Before calculating mean and covariances quantities from 20 Hz sonic anememometer and IRGA measurements, we performed tilt corrections, identified an appropriate Reynolds averaging length (τ = 30 minutes), and cleaned the raw data. After calculating 30-minute means and covariance fluxes, we cleaned the fluxes and applied recommended corrections. Note that although we label each 30-minute water vapor flux measurement as during or not during blowing snow (Section 2.3.2.3.1), ECs cannot distinguish between blowing snow sublimation and snowpack surface sublimation. All sublimation measurements in this paper potentially represent a combination of the two processes.

Tilt corrections

We transformed sonic anemometer $\langle \overline{u}, \overline{v}, \overline{w} \rangle$ from local earth coordinates into streamwise coordinates by applying a sectorial planar fit with 10, 36°-wide sectors [*Stiperski and Rotach*, 2016; *Sun*, 2007; *Wilczak et al.*, 2001]. Relative to a non-sectorial planar fit, the sectorial method decreased mean positive $\overline{w}$ (see Supplemental Section a). We calculated separate

sectorial planar fits for each month to adjust for the snow surface that changes over time [*Lundquist et al.*, 2024, see their Figure 3]. The median calculated tilt angle 0.233° (minimum 0.002°, maximum 3.78°).

Selecting a Reynolds averaging length

To determine an appropriate Reynolds averaging length (τ) for EC water vapor fluxes, we calculated $\overline{w'\rho_v'}$ cospectra over daytime hours (0900–1700) for every day of the study period using the multiresolution decomposition (MRD) method [*Howell and Mahrt*, 1997; *Vickers and Mahrt*, 2003]. We focus on the daytime when most sublimation occurs, which we verified by comparing daytime and nighttime fluxes. We classified each day's cospectrum as unstable or stable using the 0900–1700 mean sensible heat flux ($\overline{w'T'}$, $\tau = 30$ minutes) measured at 3 meters on *tower C*. We then calculated a composite cospectrum for each height and stability class by taking the mean across each τ bin (Figure 2.2). For measurements between 2–5 meters (Figures 2.2a–c), $\tau = 30$ minutes is within the spectral gap [where the cospectral curve goes to zero, *Vickers and Mahrt*, 2003]. For stable days (n=114 of 160 days), the 10–20 meter composite cospectra do not reach zero near $\tau = 30$ minutes (Figure 2.2d–f), but nearly all cospectral power is at scales smaller than 30 minutes. We utilized $\tau = 30$ minutes for all turbulent flux calculations.

Note that stable cospectra are greater than unstable cospectra (Figure 2.2, all panels), indicating that more sublimation occurs during stable conditions. This is counterintuitive, as unstable conditions over non-frozen surfaces generally accompany large evaporation rates. The opposite is observed over snow because sublimation rates are greatest during days with blowing snow, when stable conditions are common, and on sunny spring days, when stable conditions also persist. Stable conditions persist over snow on sunny spring days because while air temperatures can rise above zero, the snow surface stays at 0°C.

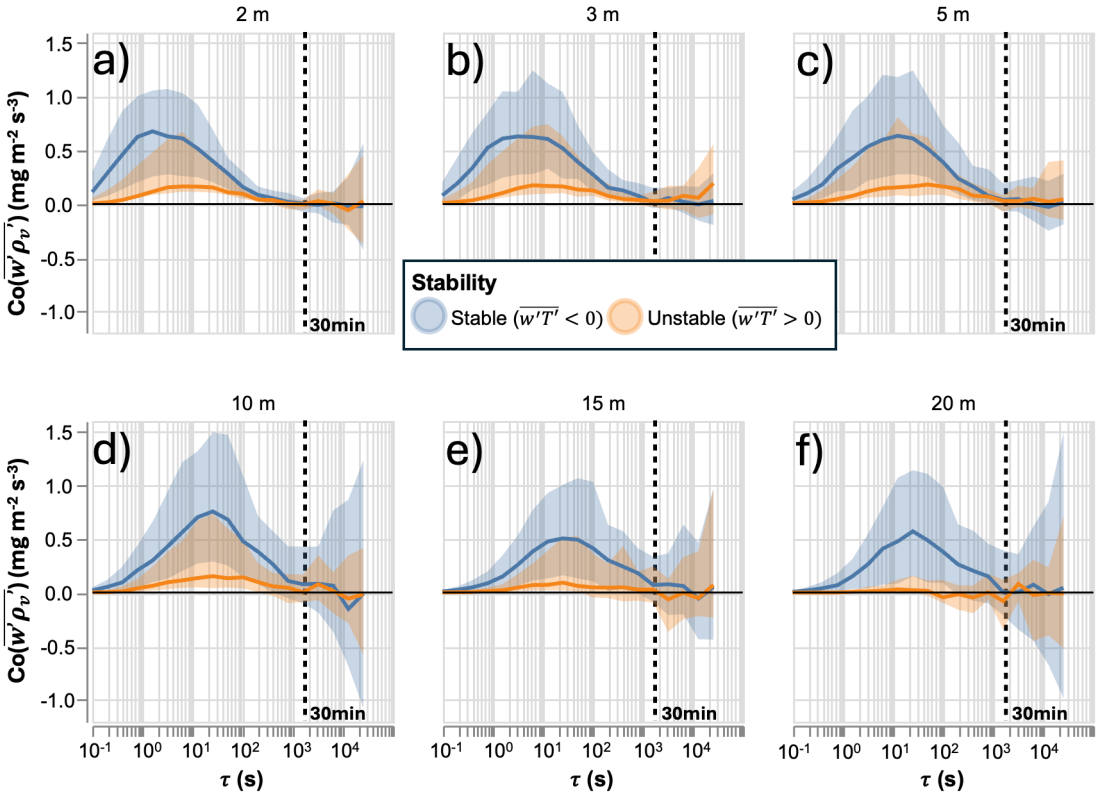

Figure 2.2: Composite cospectra of water vapor fluxes ($\overline{w'\rho_v'}$) measured at six heights on *tower C* during stable (n = 114 days) and unstable (n = 46 days) conditions. To calculate the composite cospectra, individual cospectra were calculated for each day during the snow-on period (30 November 2022 to 8 May 2023) using 20 Hz measurements between the hours of 0900 and 1700. Cospectra were calculated with the multi-resolution decomposition method [*Howell and Mahrt*, 1997]. Lines show the median cospectral power across all days for each τ bin. Shaded areas show the 25th and 75th quartiles. Days are categorized by stability, where stability is determined by the daily (0900–1700) mean sensible heat flux ($\overline{w'T'} < 0$ is stable and $\overline{w'T'} > 0$ is unstable), from the *tower C*, 3-meter eddy covariance. Vertical dashed lines mark $\tau = 30$ minutes, the Reynolds averaging length used for turbulent fluxes in this study.

Data cleaning

EC instruments at Kettle Ponds collected a nearly continuous record of fluxes during our measurement period. Of the 7676 30-minute periods during the 160 day snow-on season (Section 2.22.2.2), the 3-meter *tower C* EC collected data 92% of the time (7080 30-minute periods), an impressive statistic nearly repeated for all 12 instruments at the site (Table 2.2).

We cleaned EC data following *Mauder et al.* [2013, 2021], which reduced the number of valid fluxes. We removed 20 Hz data flagged by the sonic anemometer or IRGA, as well as spikes in w and ρ_v [*Mauder et al.*, 2013, their equation 1]. We then calculated 30-minute fluxes. Then, we discarded any 30-minute flux with more than >25% of its 20 Hz measurements flagged. We also tested 5% and 10% thresholds, which did not considerably impact results. We chose the 25% threshold to retain more data and reduce reliance on gap-filling (see end of this section). Finally, we applied a plausibility filter, removing fluxes outside the range -0.2 to 0.2 g/m^2/s (-568 to 568 W/m^2). We also tested the stationarity of 30-minute fluxes according to the method of *Foken and Wichura* [1996] (Table 2.2). We did not remove data based on this test, as we are primarily interested in estimating the long-term water vapor budget [*Mauder et al.*, 2013]. Data recovery is reported in Table 2.2. Sonic anemometer diagnostic flags primarily resulted in discarded data during blowing snow, and IRGA diagnostic flags during high humidity (Appendix A). Blowing snow did not pose a major challenge to measuring sublimation; measurements were affected only during the single most intense blowing snow event of the year (Appendix A).

The data cleaning process introduced gaps into the seasonal record of water vapor fluxes. For all estimates of total seasonal sublimation presented in this work, we filled gaps using the mean diurnal variation method with a seven-day window [*Falge et al.*, 2001]. For presented seasonal mean sublimation rates, we did not fill data gaps.

Table 2.2: Number of 30-minute water vapor flux measurements removed by different filtering steps. Flags utilized for data filtering are provided by the EC150 open path gas analyzer (IRGA) and the CSAT3 sonic anemometer. Implausible water vapor fluxes are outside the range -0.2 to 0.2 g/m^2/s (-568 to 568 W/m^2). Non-stationarity is identified according to the method of *Foken and Wichura* [1996].

		number of 30-minute averages					percent
height	tower	total	valid	flagged by EC150	flagged by CSAT3	implausible values	non-stationary
3	UE	7676	6873	73	20	0	40%
10	UE	7676	6929	78	14	3	63%
3	d	7676	6814	79	25	1	37%
10	d	7676	6832	64	14	1	61%
3	UW	7676	6936	79	17	0	42%
10	UW	7676	6836	66	11	3	60%
2	C	7676	7081	77	14	0	40%
3	C	7676	7080	72	11	0	44%
5	C	7676	7367	66	15	0	52%
10	C	7676	7237	65	8	0	64%
15	C	7676	7535	143	13	1	66%
20	C	7676	7044	102	14	6	69%

Other corrections

We applied the *Schotanus et al.* [1983] correction to $\overline{w'T'}$ and the *Webb et al.* [1980] correction to $\overline{w'\rho_v'}$.

2.3.4 Conservation of water vapor

Theory

The scalar conservation equation for water vapor in the atmospheric boundary layer (ABL) is

$$\frac{\partial \rho_v}{\partial t} + \frac{\partial (u\rho_v)}{\partial x} + \frac{\partial (w\rho_v)}{\partial z} = S(x,z,t) \tag{2.1}$$

where the x coordinate is aligned with the local mean wind direction, z is perpendicular to the local terrain, and S is a water vapor source or sink term (e.g. blowing snow sublimation or formation of diamond dust) [*Lee*, 1998; *Finnigan*, 1999; *Paw U et al.*, 2000]. In this study, and those cited, we ignore molecular diffusion and restrict our study to two-dimensional flows. After Reynolds decomposition and averaging, Equation 2.1 becomes

$$\begin{aligned} \frac{\partial \overline{\rho_v}}{\partial t} + \overline{u}\frac{\partial \overline{\rho_v}}{\partial x} + \overline{\rho_v}\frac{\partial \overline{u}}{\partial x} + \overline{w}\frac{\partial \overline{\rho_v}}{\partial z} + \overline{\rho_v}\frac{\partial \overline{w}}{\partial z} \\ + \frac{\partial \overline{u'\rho_v'}}{\partial x} + \frac{\partial \overline{w'\rho_v'}}{\partial z} = \overline{S}(x,z,t). \end{aligned} \tag{2.2}$$

Accounting for two-dimensional continuity ($\frac{\partial \overline{u}}{\partial x} + \frac{\partial \overline{w}}{\partial z} = 0$) and assuming that $\frac{\partial \overline{u'\rho_v'}}{\partial x} << \frac{\partial \overline{w'\rho_v'}}{\partial z}$ [*Lee*, 1998; *Finnigan*, 1999], we simplify to

$$\frac{\partial \overline{\rho_v}}{\partial t} + \overline{u}\frac{\partial \overline{\rho_v}}{\partial x} + \overline{w}\frac{\partial \overline{\rho_v}}{\partial z} + \frac{\partial \overline{w'\rho_v'}}{\partial z} = \overline{S}(x,z,t). \tag{2.3}$$

The first term on the left-hand side of Equation 2.3 is the change in local moisture storage (storage change term), the second and third terms are the horizontal and vertical advection terms, respectively, and the fourth term is the vertical turbulent flux divergence (VTFD) term.

In the special case where there is no blowing snow sublimation or condensation of water vapor in the air ($\overline{S} = 0$), humidity changes slowly ($\frac{\partial \overline{\rho_v}}{\partial t} \approx 0$), humidity is horizontally

homogeneous ($\frac{\partial \overline{\rho_v}}{\partial x} = 0$), and there is no mean vertical velocity ($\overline{w} = 0$), then $\partial \overline{w'\rho_v'}/\partial z \approx 0$ and $\overline{w'\rho_v'}$ is constant with height ("constant flux layer"). The constant flux layer, the lower portion of the ABL where turbulent fluxes vary with height less than 10% [*Stull*, 1988], has the convenient implication that EC flux measurements at any height equal surface fluxes - i.e. $\overline{w'\rho_v'}$ equals the surface sublimation rate. Generally, studies using the EC method assume that fluxes measured at the instrument height equal surface fluxes.

Initial observations from the SOS campaign indicate that that is not the case, that $\partial \overline{w'\rho_v'}/\partial z \neq 0$ [*Lundquist et al.*, 2024]. To explore why, we estimated all terms in Equation 2.3, except $\overline{S}$, which cannot be measured directly. We found that the signal-to-noise ratio in $\frac{\partial \overline{\rho_v}}{\partial x}$ (measured between Kettle Ponds and Annex, Figure 1) was too small to confidently estimate the sign and magnitude of horizontal advection (Appendix B, C). We therefore further simplified Equation 2.3 to include just the terms that we can estimate, and add a residual term (Res),

$$Res = \frac{\partial \overline{\rho_v}}{\partial t} + \frac{\partial \overline{w'\rho_v'}}{\partial z} + \overline{w}\frac{\partial \overline{\rho_v}}{\partial z}. \tag{2.4}$$

Implementation

We estimated terms in Equation 2.4 using measurements from *tower C*. We calculated Res as the sum of the three terms. When blowing snow flux sensors indicate there is no blowing snow, we assume $\overline{S} = 0$, and non-zero Res indicates either that there is non-zero horizontal advection or error in our calculations for the three terms (compare Equations 2.3 and 2.4). When there is blowing snow, non-zero Res may represent a non-zero source term from blowing snow sublimation ($\overline{S} > 0$), non-zero horizontal advection, or error in our calculations.

Storage change term We estimated $\frac{\partial \overline{\rho_v}}{\partial t}$ by calculating the average $\overline{\rho_v}$ between 2 and 20 meters (Section 2.3.2.3.2), for each 30-minute period. We then evaluated the time derivative of vertically-averaged $\overline{\rho_v}$ using a central differencing scheme.

Vertical advection term We estimated $\overline{w}\frac{\partial\overline{\rho_v}}{\partial z}$ at z = 3, 5, 10, 15, and 20 meters. $\overline{w}$ is measured by ECs. To estimate $\frac{\partial\overline{\rho_v}}{\partial z}$ at each height, we fit a log-polynomial function to the vertical profile of $\overline{\rho_v}$ measurements.

$$\overline{\rho_v} = \alpha\Big(\ln\frac{z}{z_{0,\rho_v}}\Big)^2 + \beta\ln\frac{z}{z_{0,\rho_v}} + \overline{\rho_v}_0 \tag{2.5}$$

where $\overline{\rho_v}_0$ is $\overline{\rho_v}$ at the snow surface, estimated from T_s according to the saturation vapor pressure curve recommended by *Alduchov and Eskridge* [1996]. α and β are fitted constants. z_{0,ρ_v} is the scalar roughness length for humidity [0.001 meters, *Andreas*, 1987]. Equation 2.5 was inspired by *Grachev et al.* [2005, their equation 8], but allows us to include $\overline{\rho_v}_0$ measurements in the curve fitting process, which improves fitting because vertical humidity gradients are steepest closest to the snow surface. Equation 2.5 is fitted, and α and β calculated, at each 30-minute time step, with heights (z) adjusted for snow depth, using a non-linear least squares regression [*Vugrin et al.*, 2007; *Virtanen et al.*, 2020]. $\frac{\partial\overline{\rho_v}}{\partial z}$ is calculated analytically from Equation 2.5 with fitted α and β.

Vertical turbulent flux divergence (VTFD) We estimated the VTFD term using a finite difference approximation between a lower (z_1) and upper (z_2) measurement height,

$$\frac{\partial\overline{w'\rho_v'}}{\partial z} \approx \frac{\Delta\overline{w'\rho_v'}}{\Delta z} = \frac{\overline{w'\rho_v'}\big|_{z=z_2} - \overline{w'\rho_v'}\big|_{z=z_1}}{z_2 - z_1}. \tag{2.6}$$

We estimated VTFD between z_1 = 3 and z_2 = 10 m and between z_1 = 3 and z_2 = 20 m. Unlike with the vertical profile of $\overline{\rho_v}$, we did not fit a curve to $\overline{w'\rho_v'}(z)$, as there is no widely accepted functional form for its vertical structure, whereas $\overline{\rho_v}(z)$ is often assumed to follow a logarithmic profile (e.g., Monin-Obukhov Similarity Theory). Additionally, we only use estimates of the VTFD term to qualitatively identify the existence of divergence. The vertical advection term, on the other hand, is used to quantitatively refine estimates of sublimation using the net exchange equation (next section).

Net exchange of water vapor

If VTFD is non-zero, and there is advection or rapid humidity changes, EC estimates of surface sublimation can be improved upon by incorporating estimates of the advection and storage change terms. Following *Lee* [1998] and *Finnigan* [1999] we estimate the flux, or net exchange (NE), of water vapor across the boundary between the snow surface and the atmosphere by integrating Equation 2.4 (ignoring the residual term) between the surface, $z = 0$, and a measurement height, $z = H$, while assuming horizontal homogeneity,

$$NE = \overline{w'\rho'_{v0}} = \overline{w'\rho'_{vH}} + \int_0^H \left(\frac{\partial \overline{\rho_v}}{\partial t} + \overline{w} \frac{\partial \overline{\rho_v}}{\partial z} \right) dz, \tag{2.7}$$

where NE or $\overline{w'\rho'_{v0}}$ is the water vapor flux (sublimation rate) at the snow surface and the integral term represents a "correction" to the EC water vapor flux measured at a given height H, $\overline{w'\rho'_{vH}}$. Note that similar correction terms could be derived for the horizontal advection and source terms, if they were estimated. Equation 2.7 differs from the equation presented by *Lee* [1998] only because we have not assumed that $\overline{w}$ increases linearly with height. See *Lee* and *Finnigan* for a complete derivation and discussion of the net exchange method.

To estimate NE, we used a gridded numerical solution to Equation 2.7 with one-meter spacing (trapezoid rule), which requires estimates of $\overline{w}\frac{\partial \overline{\rho_v}}{\partial z}$ at one meter intervals. $\overline{\rho_v}$ is available at one-meter spacing from measurements. We evaluated $\frac{\partial \overline{\rho_v}}{\partial z}$ at one-meter intervals following the fitting process described in Section 2.3.2.3.4.2.3.4. $\overline{w}$ was linearly interpolated between *tower C* EC measurements of $\overline{w}$ (at 3, 5, 10, 15, and 20 meters), including $\overline{w} = 0$ at $z = 0$, for each time step. We calculated NE for each EC on *tower C*.

2.4 Results

In the following, we first present an overview of sublimation rates estimated using the EC method throughout the 2022-23 winter season. We then examine how $\overline{w'\rho'_v}$ varies vertically and why, by examining the transport terms in Equation 2.4. Finally, we estimate sublimation using the net exchange method (Equation 2.7).

2.4.1 Seasonal overview

Twelve EC instruments at Kettle Ponds measured total sublimation between 33–42 mm of snow water equivalent (SWE), which accounts for 7.6–9.6% of the season's maximum snowpack (measured by the snowpillow at *tower C*, Figure 2.3A). The average daily sublimation rate was 0.26 mm/day (measured at 10 meters on *tower C*). Rates were elevated in December (average 0.23 mm/day), depressed in January (0.10) and February (0.19), and increased in March (0.33) and April (0.49) (Figure 2.3B). The two-meter EC began systematically underestimating sublimation at the beginning of March when snow depth rose above one meter (see Supplemental Section b). Snow depth reached a maximum of 1.55 m on 30 March (Figure 2.3a).

Prior to mid-March, net radiation at the snow surface was consistently negative (Figure 2.3C), and daily sublimation was mostly associated with blowing snow (Figure 2.3B). Over half of the total sublimation in December (6.6 mm SWE) occurred during five days with blowing snow, December 12–14 (1.3 mm) and 21-22 (2.1 mm). After the spring equinox (March 20), net radiation became consistently positive (Figure 2.3C), and sublimation without blowing snow (surface sublimation) dominated (Figure 2.3B). Before (after) the spring equinox, blowing snow occurred 24 (18%) of the time and accounted for 78 (31%) of sublimation.

2.4.2 Spatial variation in measured sublimation rates

Seasonal sublimation measurements from 12 EC instruments on four towers varied by tower and height (Figure 2.4a). 3-meter measurements from different towers more closely agreed (38–40 mm) than 10-meter measurements (36–42 mm). Measurements increased from 3 to 10 m and decreased above. The 5- and 10-meter ECs measured 7% and 12% more sublimation than the 3-meter EC (40 and 42 vs. 38 mm), while the 15- and 20-meter ECs measured 12% and 10% less (33 and 34 mm).

To investigate when $\overline{w'\rho_v'}$ varied with height, we calculated seasonal mean $\overline{w'\rho_v'}$ for each EC during times without blowing snow, during nighttime and daytime, and during times

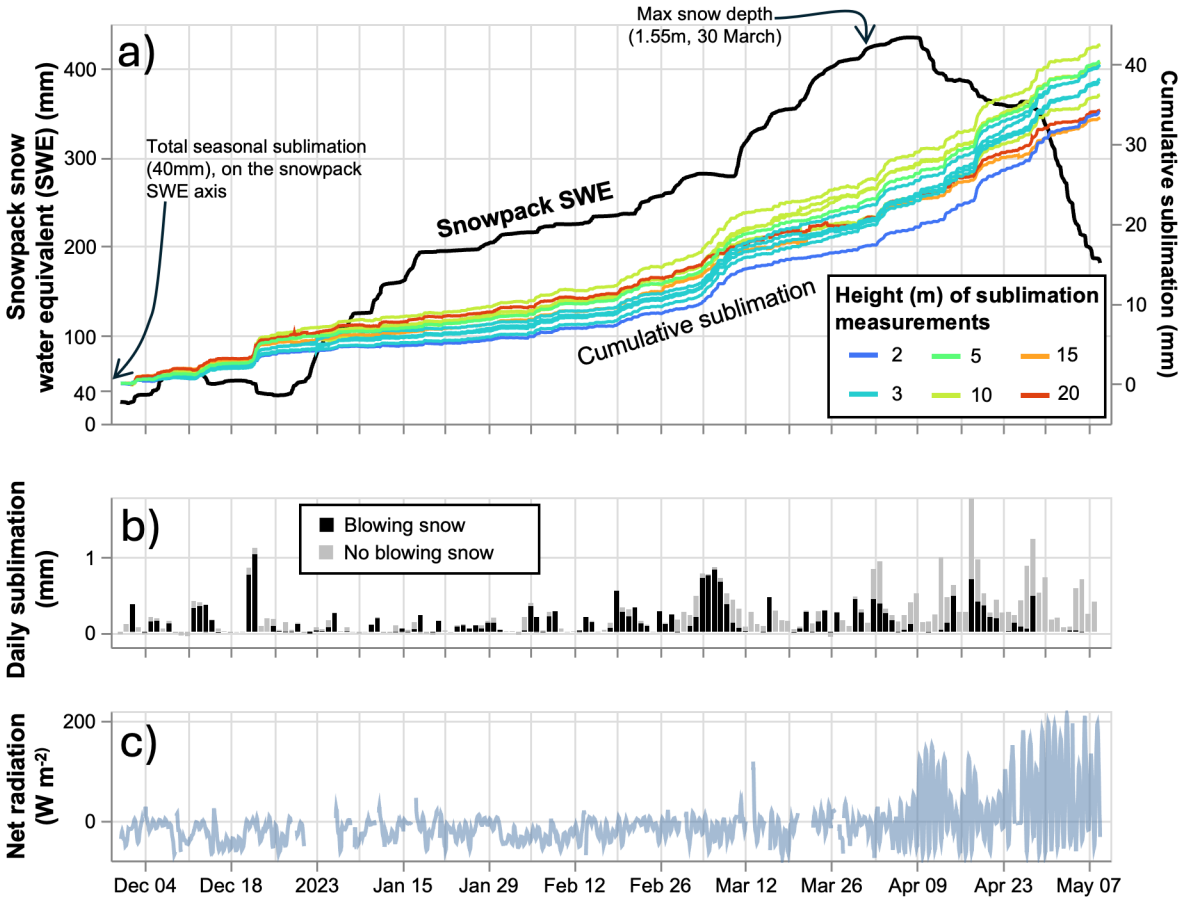

Figure 2.3: a) Snow water equivalent (SWE) of the snowpack measured by the fluidless snow pillow at *tower UE* (black line) and cumulative seasonal sublimation measured by 12 eddy covariance systems on four towers at different heights (colored lines). Data is included between 30 November 2022 to 8 May 2023, the time period with continuous snow cover across the Kettle Ponds field site. b) Daily sublimation, calculated as the sum of all 30-minute flux measurements from each day. Stacked, colored bars indicate how much of the daily sublimation is during blowing snow (black) and not during blowing snow (grey) according to FlowCapt sensor measurements of blowing snow flux. The total height of the stacked bars indicates daily total sublimation. Sublimation estimates are from the 3-meter EC on *tower C*. c) 60-minute averaged net radiation measured with two-way shortwave and longwave radiometers.

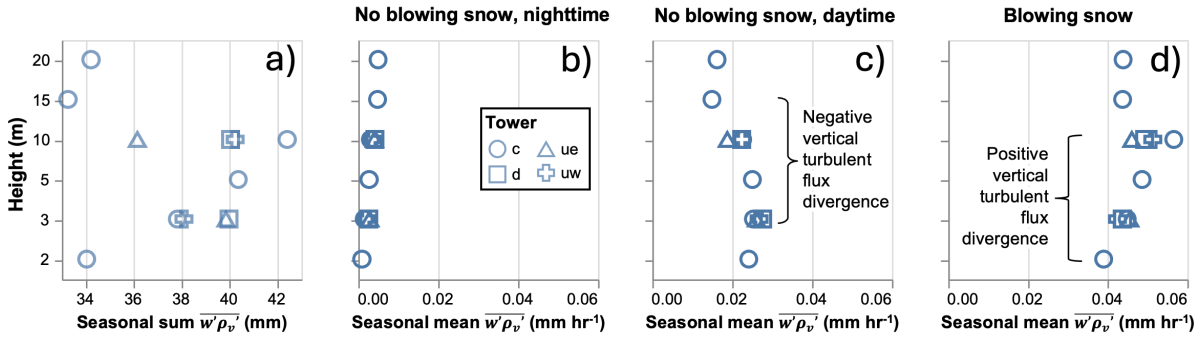

Figure 2.4: Sublimation estimates (water vapor flux measurements, $\overline{w'\rho_v'}$) from 12 eddy covariance instruments on four towers at different heights above the ground level. a) Total seasonal sublimation estimates from 12 instruments including measurements between 30 November 30 2022 to 8 May 2023, when snow cover was continuous across the Kettle Ponds field site. b) Seasonal mean $\overline{w'\rho_v'}$ across all 30-minute fluxes during times without blowing snow and during nighttime, c) without blowing snow and during daytime, and d) during blowing snow (nighttime and daytime). Times with blowing snow are identified using blowing snow flux measurements greater than zero. Daytime and nighttime are distinguished by sunrise and sunset. Shapes indicate the tower of the measurement.

with blowing snow (including both night and day) (Figure 2.4b–d). During nighttimes without blowing snow, fluxes were relatively close to zero (Figure 2.4b). During daytimes without blowing snow, *tower C* 5-meter mean $\overline{w'\rho_v'}$ was 0.8% less than the *tower C* 3-meter measurement, suggesting the existence of a shallow ($\leq$ 5 meter) constant flux layer (Figure 2.4c). Above 5 meters, fluxes decreased, with 10-, 15-, and 20-meter mean $\overline{w'\rho_v'}$ 10, 41, and 36 % less than the 3-meter measurement, respectively (negative VTFD, $\frac{\partial \overline{w'\rho_v'}}{\partial z} < 0$, Figure 2.4c). Negative VTFD above five meters appeared in every month of the observation period. During blowing snow, $\overline{w'\rho_v'}$ increased with height up to 10 meters, with 5- and 10-meter values 8% and 26% higher than at 3 meters (positive VTFD, $\frac{\partial \overline{w'\rho_v'}}{\partial z} > 0$, Figure 2.4d). Above 10 meters, values were within 2.5% of the 3-meter measurement.

2.4.3 Positive vertical turbulent flux divergence during blowing snow

We hypothesized that during blowing snow, suspended snow particles sublimate, add water vapor to the near-surface atmosphere ($\overline{S} > 0$, Equation 2.3), and balance the positive VTFD ($\frac{\partial \overline{w'\rho_v'}}{\partial z} > 0$) observed between 3 and 10 meters during blowing snow (Figure 2.4d). We examined mean $\overline{w'\rho_v'}$ from *tower C* ECs during blowing snow conditions of varying blowing snow intensity (as measured by the FlowCapt sensors) to explore this hypothesis. The mean blowing snow flux from all 30-minute periods with blowing snow was 0.011 g m^{-2} s^{-1} and only one event (21–22 December 2022) had blowing snow fluxes greater than 10 g m^{-2} s^{-1} (Figure 2.5a). Positive VTFD between three and 10 meters (the slope of $\overline{w'\rho_v'}(z)$) increased with blowing snow flux (Figure 2.5b). During the most extreme blowing snow event of the season (21–22 December 2022), 10-meter $\overline{w'\rho_v'}$ quadrupled 2-meter $\overline{w'\rho_v'}$ (Figure 2.5b). We also found that generally, as blowing snow fluxes increase, relative humidity decreases (Figure 2.5c).

We estimated terms in the water vapor budget (Equation 2.4) between 21–22 December 2022, which had the highest measured 3-meter mean wind speeds (14.2 m/s) and 0–1m blowing snow fluxes (49.7 g m^{-2} s^{-1}) of the season. These extreme winds, along with cold air, were ushered into the region by a deep upper-level trough and associated surface cold

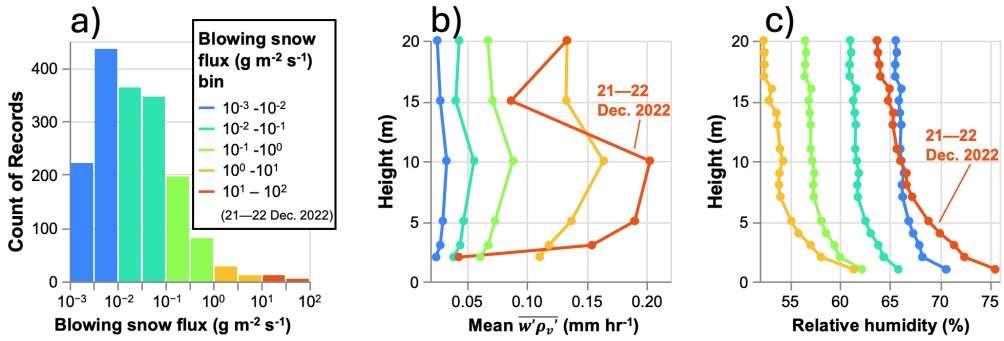

Figure 2.5: a) Distribution of blowing snow flux measurements. The log distribution has a lower limit at 10^{-3} because the Flowcapt instrument has a minimum detection threshold of 10^{-3} g m^{-2} s^{-1} [*Trouvilliez et al.*, 2015]. b) Mean vertical profiles of $\overline{w'\rho_v'}$ measured on *tower C*, using only fluxes during periods with blowing snow, binned by intensity of the measured blowing snow flux. Note that all data from the highest bin ($10^1 - 10^2$ g m^{-2} s^{-1}) are from 21–22 December 2022. c) The mean vertical profiles of relative humidity measured on *tower C*, for the same categories.

front [*Hogan et al.*, 2023]. Blowing snow began shortly before 2100 on 21 December 2022 and lasted until 2100 on 22 December, and, throughout the event, 0–1 meter blowing snow fluxes exceeded 1–2 meter fluxes (Figure 2.6a). 10- and 20-meter $\overline{w'\rho_v'}$ frequently doubled 3-meter $\overline{w'\rho_v'}$ (Figure 2.6b), resulting in a positive VTFD term ($\frac{\partial \overline{w'\rho_v'}}{\partial z}$, Figure 2.6c). Storage change and vertical advection terms were smaller than the VTFD term, resulting in a large positive Residual term (Figure 2.6c).

2.4.4 Negative vertical turbulent flux divergence during mid-day

While positive VTFD occurred during blowing snow conditions (Figure 2.4d), negative VTFD occurred during non-blowing snow conditions (Figure 2.4c). To identify what processes could be causing negative VTFD, we estimated terms in the water vapor budget (Equation 2.4) on 5 May 2023, a day with little synoptic activity on which we observed

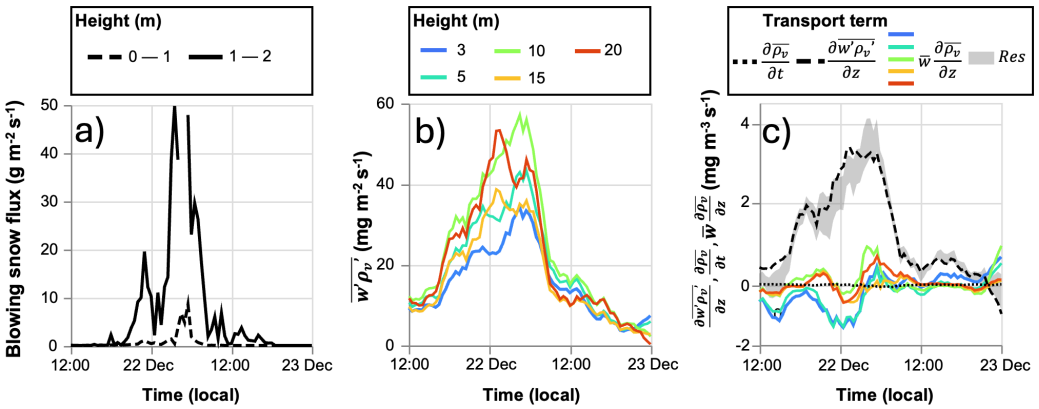

Figure 2.6: Blowing snow case study, 1200 21 December through 22 December 2022. a) Blowing snow fluxes measured by the FlowCapt sensors between 0–1m (solid line) and 1–2m (dashed line) above ground level. b) $\overline{w'\rho_v'}$ measured by eddy covariance instruments at multiple heights on *tower C*. c) Estimated vertical advection at multiple heights (solid lines, colors correspond to those in panel b), vertical turbulent flux divergence (black dashed line), and the storage change term (black dotted line) from the conservation of water vapor equation (Equation 2.4). Time series in panels b and c are smoothed using a rolling average with a 2-hour window.

negate VTFD (Figure 2.7a). The storage change term was relatively small and negative

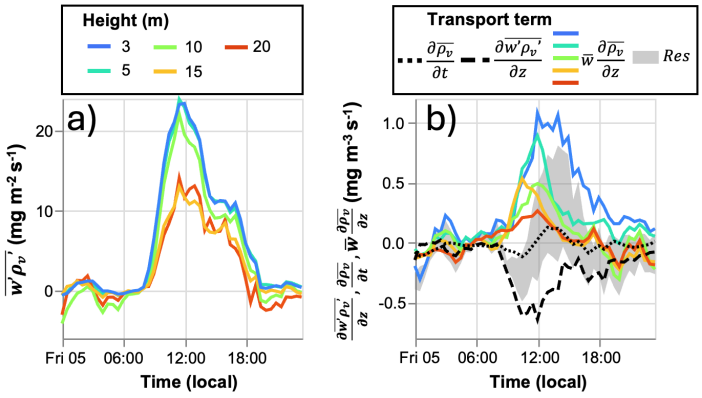

Figure 2.7: Case study of water vapor transport on 5 May 2023, a day with no blowing snow. a) $\overline{w'\rho_v'}$ measured by eddy covariance instruments on *tower C*. Line color indicates measurement height. b) Estimated vertical advection at multiple heights (solid lines, colors correspond to those in panel a), vertical turbulent flux divergence (black dashed line), and the storage change term (black dotted line) from the conservation of water vapor equation (Equation 2.4). Time series in both panels are smoothed using a rolling average with a 2-hour window.

VTFD was balanced by positive vertical advection for much of the day, resulting in a near-zero residual term (Figure 2.7b). Negative VTFD was not balanced, and the residual term was non-zero, for a few hours in the morning (0800–1100). We also explored the hypothesis that sub-mesoscale motions contaminated the higher level ECs, which could result in flux sensitivity to τ and cause negative VTFD [*Vickers and Mahrt*, 2003]. We found that varying τ did not remove the observed negative VTFD (see Supplemental Section c).

While positive vertical advection balances negative VTFD on 5 May, we wondered if vertical advection could explain the seasonal occurrence of negative VTFD during non-blowing snow conditions (i.e. Figure 2.4c). We found that the vertical advection term (due to the direction of $\overline{w}$) behaves differently during upvalley and downvalley winds. For

that reason, we divided all 30-minute periods without blowing snow into up and downvalley wind categories (Figure 2.8a, e) and calculated daily mean composite variables to examine seasonally averaged water vapor transport. We calculated mean vertical profiles of $\overline{\rho_v}$ (Figure 2.8b, f), mean $\overline{w}$ (Figure 2.8c, g), and daily mean water vapor transport terms (Figure 2.8d, h). During both upvalley and downvalley winds, nighttime was characterized by relatively small, positive, near-surface humidity gradients, and daytime by relatively large, negative gradients, indicating that water vapor deposition is possible at night and sublimation during the day (Figure 2.8b and f). $\overline{w}$ during upvalley winds was inconsistent, but mostly positive, and during downvalley winds, $\overline{w}$ was consistently positive at night and negative during the day (Figures 2.8c, g). During upvalley winds, vertical advection was near zero and VTFD was negative, resulting in a negative residual term (Figures 2.8d). During daytime downvalley winds, vertical advection terms were positive, balancing the negative VTFD term, resulting in a near-zero residual term (Figure 2.8h). The two terms did not balance, and *Res* was negative, for some daytime hours, between 0800–1100 and 1400–1600. During all wind conditions, the storage change term is relatively small. We discuss the water vapor transport terms further in Section 2.5.2.5.3.

2.4.5 Net exchange of water vapor

Because vertical advection and storage change are non-negligible at our site, EC measurements of $\overline{w'\rho_v'}$ may misrepresent sublimation rates. We calculated sublimation using the net exchange equation (Equation 2.7) for all EC instruments on *tower C* to better resolve total seasonal sublimation at Kettle Ponds. On average, the correction increased seasonal sublimation estimates by 5.5% (Figure 2.9). 15-meter sublimation estimates increased the most (6.9%) and 20-meter estimates the least (3.2%). Corrections to 3- and 10-meter ECs were just outside the uncertainty of the EC method estimates (uncertainty estimated from duplicated measurements, see Figure 2.9). The net exchange equation increased sublimation estimates more during times with downvalley winds and no blowing snow, when we observed consistent vertical advection (Figure 2.8h). During those times, 3-, 10-, and 20-meter subli-

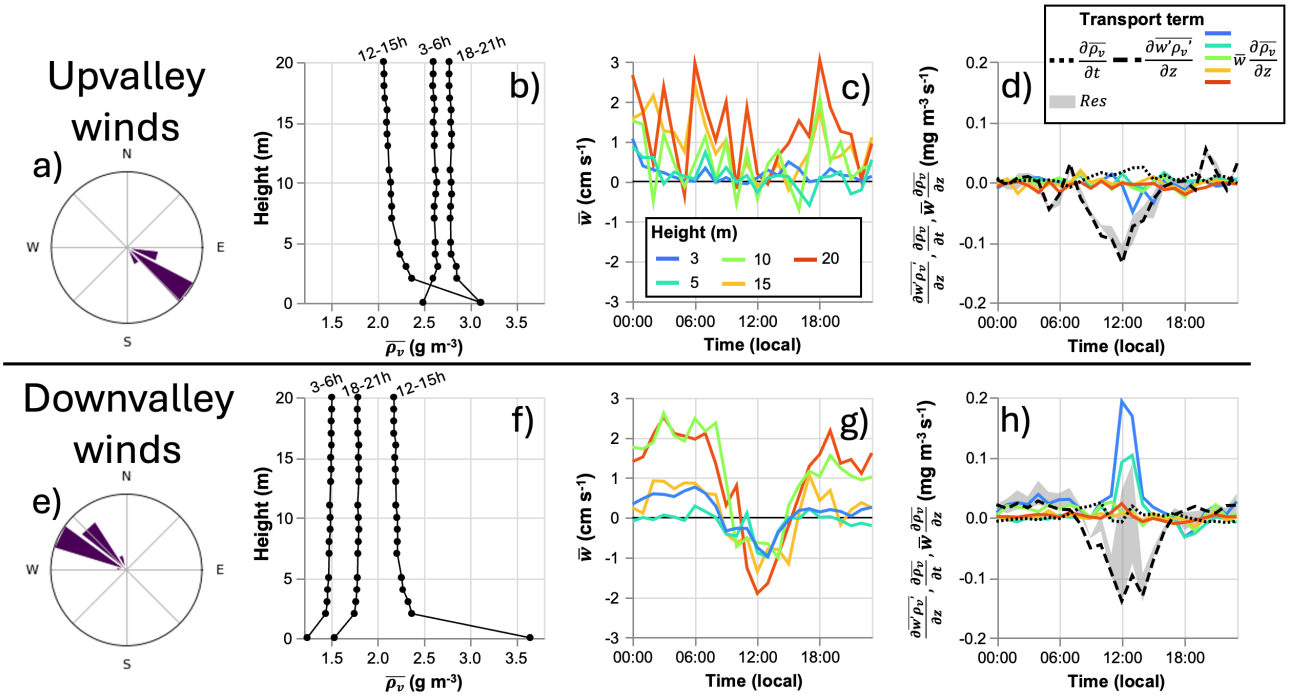

Figure 2.8: Mean diurnal cycles for various measurements, categorized by wind direction, during times without blowing snow, between 30 November 2022 and 8 May 2023. For each measurement, height, and wind category, hourly averages are calculated from all 30-minute averages without blowing snow. a) Upvalley winds include wind directions between 92–152°(n=1066 30-minute periods), e) downvalley winds between 292–342°(n=3011). b) and f) Composite vertical profiles of absolute humidity ($\overline{\rho_v}$), measured by T/RH sensors on *tower C*. Data is averaged across three-hour periods; selected three-hour periods illustrate the diurnal cycle. c) and g) Composite vertical wind velocity ($\overline{w}$) from sonic anemometers on *tower C*. d) and h) Composite estimates of vertical advection at multiple heights (solid lines, colors correspond to those in panels c and g), vertical turbulent flux divergence (black dashed line), and the storage change term (black dotted line) from the conservation of water vapor equation (Equation 2.4).

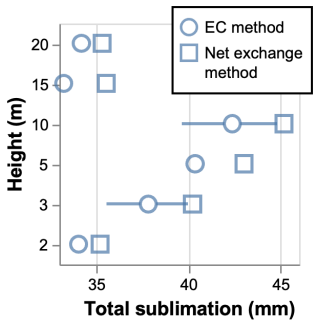

Figure 2.9: Total seasonal sublimation estimated by the eddy covariance and net exchange methods with instruments on *tower C*. EC method estimates (circles) correspond to the measurements from *tower C* in Figure 2.4a. Bars represent $\pm 2 * std$, where *std* is the standard deviation of seasonal sublimation measurements from four eddy covariance instruments on four different towers, at heights 3 and 10 meters (see Figure 2.4a).

mation estimates using the net exchange equation were 22, 23, and 26% larger, respectively, than estimates using the EC method. Corrections on individual days could be larger. For example, on 5 May 2023 (Figure 2.7), 3-, 10-, and 20-meter estimates using the net exchange method were 8.6, 36, and 77% larger than EC-method estimates.

2.5 Discussion

2.5.1 Seasonal sublimation estimates

Our estimates of seasonal sublimation using the EC method (7.6–9.6% of seasonal max SWE, 0.26 mm/day, Section 2.4.2.4.1) are less than those from other studies that deployed ECs at open sites in the Rocky Mountains, including *Reba et al.* [2012], who measured 16–41% (0.32–0.52 mm/day) on an exposed hillside over three years, and *Sexstone et al.* [2016], who measured 10–17% (0.33–0.38 mm/day) on a ridge over two years. Both of their sites likely have higher winds and therefore more frequent blowing snow than the valley-floor Kettle Ponds site. Sublimation estimates in even windier places, like the Canadian Prairies [1.8 mm/day, *Pomeroy and Essery*, 1999], are also larger than our measurements, indicating that

understanding wind and blowing snow suspension and sublimation is critical to quantifying sublimation.

Daily-averaged sublimation rates at Kettle Ponds were also lower than 30 of the 31 estimates compiled by *Jackson and Prowse* [2009, includes both EC-measured and modeled results]. Among their compiled estimates, the highest sublimation rates (0.71 and 1.2 mm/day) were recorded above forest canopies [*Molotch et al.*, 2007; *Nakai et al.*, 1999]. Model outputs from *Strasser et al.* [2008, see their Figure 14] indicate that unvegetated valley-floor sites have the lowest sublimation rates within a watershed and forested valley floors experience higher rates. These comparisons suggest that Kettle Ponds may experience some of the lowest sublimation rates in the watershed. To better constrain total sublimation in mountain valleys, future studies should deploy blowing snow sensors and EC instruments across a range of microenvironments, including at open sites, above forest canopies, and on exposed ridges. Measuring forested sites is especially important due to their high sublimation rates and the uncertainty in modeled canopy sublimation introduced by parameterizations of canopy snow interception, unloading, and sublimation [*Lundquist et al.*, 2021].

Before the spring equinox, net radiation was negative, and sublimation rates were low, except during blowing snow events. After the equinox, net radiation became positive and sublimation increased, with less contribution from blowing snow. This indicates a seasonal shift from blowing-snow-driven to radiation-driven sublimation (Section 2.4.2.4.1). Such variability, on seasonal timescales due to the changing surface energy balance and on daily timescales due to the variability of blowing snow, highlights why sublimation measured on a few days cannot reliably represent seasonal totals and may help explain why published sublimation estimates vary so widely [*Mott et al.*, 2018].

One limitation of the SOS campaign is that it lasted only one season. While prior multi-year studies observed little interannual variation in total sublimation [*Sexstone et al.*, 2016; *Reba et al.*, 2012], our results show that a few blowing snow events dominated mid-winter sublimation. This suggests that interannual variability in storm frequency could influence seasonal sublimation totals. Future work should explore how synoptic variability influences

sublimation rates.

2.5.2 Positive vertical turbulent flux divergence during blowing snow

During blowing snow events, vertically distributed EC instruments measured positive VTFD ($\frac{\partial \overline{w'\rho_v'}}{\partial z} > 0$, Figures 2.5b and 2.6c). During a 21–22 December 2022 blowing snow event, we found that vertical advection and storage change were relatively small, and the residual term approximately equaled the VTFD term (Figure 2.6c). The large residual term suggests that suspended snow is sublimating, introducing water vapor into the ABL ($\overline{S} > 0$), and the water vapor budget (Equation 2.3) simplifies to $\overline{S} = \frac{\partial \overline{w'\rho_v'}}{\partial z}$, although this interpretation is limited by the unconstrained horizontal advection term. Our hypothesis is supported by the fact that as blowing snow intensity increases, $\frac{\partial \overline{w'\rho_v'}}{\partial z}$ increases (i.e. the slope of $\overline{w'\rho_v'}(z)$ in Figure 2.5b increases), as we expect blowing snow sublimation rates ($\overline{S}$) to increase with blowing snow intensity. Future work could estimate $\overline{S}$ directly from measured $\frac{\partial \overline{w'\rho_v'}}{\partial z}$ and evaluate snow models that parameterize the surface and blowing snow sublimation processes separately [e.g. *Strasser et al.*, 2008; *Sexstone et al.*, 2018].

Previous studies found that EC flux measurements underestimate total sublimation (surface plus blowing snow) during blowing snow [*Sigmund et al.*, 2022; *Sexstone et al.*, 2018]. However, our results suggest that higher EC instruments (e.g., at 10 meters) can accurately measure total sublimation, as water vapor fluxes during blowing snow events peaked at 10 meters (Figure 2.5b) and blowing snow concentration decreases exponentially with height [Figure 2.6a, also in the literature, e.g. *Gordon and Taylor*, 2009]. It is possible, however, that total sublimation is even higher than measured at 10 meters, particularly if vertical or horizontal advection terms are large. Future research should examine the possibility of horizontal advection during blowing snow events, which we hypothesize could arise because of the horizontal homogeneity in blowing snow concentration over complex terrain. If "clouds" of blowing snow are discontiguous across the landscape, horizontal humidity gradients would develop over short distances, causing horizontal advection. Such a processes would create negative VTFD at the top of the blowing snow layer, which we observed above 10 meters

during blowing snow (Figure 2.5b and 2.6b).

At Kettle Ponds, measurements of sublimation and humidity during blowing snow events (Figure 2.5) indicate that blowing snow sublimation is not a self-limiting process, as suggested by previous research in Arctic and Swiss alpine environments [*Liston and Sturm*, 2004; *Groot Zwaaftink et al.*, 2013; *Déry and Yau*, 2002]. Blowing snow conditions were responsible for the largest sublimation rates of the season (Figure 2.4). Additionally, as blowing snow fluxes increased, sublimation rates increased, and relative humidity decreased (Figure 2.5b and c). Even during the most extreme blowing snow event of the year, when blowing snow fluxes were in the $10^1 - 10^2 g/m^2/s$ range, near-surface relative humidity remained below 75% (Figure 2.5c, red line). However, Kettle Ponds has small blowing snow fluxes, relative to high elevation ridges [*Strasser et al.*, 2008] and alpine passes [*Trouvilliez et al.*, 2015]. At such sites, sublimation may become self-limiting. Future research should deploy blowing snow flux sensors and ECs to a variety of settings to clarify the importance of blowing snow sublimation in the alpine water balance and evaluate the models that have thus far been used to do just that [e.g. SnowModel, *Sexstone et al.*, 2018].

2.5.3 Negative vertical turbulent flux divergence

During daytime non-blowing snow conditions, we consistently observed negative VTFD above 5 meters (Figure 2.4c). On 5 May 2023, a day without blowing snow, we estimated all water vapor transport terms and found that vertical advection approximately balanced the negative VTFD, yielding a closed water vapor budget (near-zero residual). *Paw U et al.* [2000] predicted that vertical scalar advection can occur in complex terrain due to vertical velocities induced by horizontal divergence of the near-surface velocity field. At Kettle Ponds, one-meter-tall rollers (Figure 2.1b) may induce such flow. *Paw U et al.* also suggest mesoscale circulations — such as cross-valley circulations in steep alpine valleys [*Weigel and Rotach*, 2004] — could generate mean vertical velocities. Future work could use Doppler lidar [e.g. *Babić et al.*, 2021] or numerical simulations [e.g. *Doyle et al.*, 2009; *Farina and Zardi*, 2023; *Schmidli*, 2013] to assess whether valley-scale circulations induce large vertical

velocities and advection near the valley floor.

We examined seasonally averaged diurnal patterns in transport terms and found that the water vapor budget was approximately closed (near-zero residual) during mid-day downvalley winds (Figure 2.8h) and nighttime upvalley winds (Figure 2.8d). Budget non-closure occurred during mid-day upvalley and nighttime downvalley winds, conditions characteristic of diurnal thermal valley winds [*Whiteman and Doran*, 1993; *Zardi and Whiteman*, 2013], which have been observed in the East River Valley [*Adler et al.*, 2023]. This suggests that unmeasured horizontal advection may play an important role during synoptically weak conditions when thermal winds dominate. Constraining valley-scale horizontal advection will require humidity sensors with high relative accuracy [e.g. *Harder et al.*, 2017] distributed across large distances. Numerical simulations could also explore the causes of horizontal, as well as vertical, advection. Future studies of water vapor advection in complex terrain should also examine sensible heat advection. Quantifying both may improve energy balance closure over snow and in complex terrain [*Helgason and Pomeroy*, 2012; *Foken et al.*, 2006, 2011; *Morrison et al.*, 2023].

Although we focused on negative VTFD during non-blowing snow conditions for simplicity, negative VTFD also occurred during blowing snow, above 10 meters (Figures 2.4d and 2.5b). During the 21–22 December event, above-10-meter negative VTFD began around 0300 (when 20-meter $\overline{w'\rho_v'}$ dropped below 10-meter $\overline{w'\rho_v'}$, Figure 2.6b), coinciding with a rise in vertical advection (Figure 2.6c). Meanwhile, positive VTFD persisted below 10 meters (due to blowing snow sublimation, Section 2.5.2.5.2). This vertical structure in the fluxes, positive divergence overlain by negative divergence, may mark the top of the blowing snow layer. Strong humidity gradients across this boundary can amplify vertical advection, as downward vertical motion transports dry air into the humid blowing snow layer, promoting sublimation. This process is akin to the entrainment of dry air into fog, which enhances evaporation and fog dissipation [*Singh et al.*, 2024]. At Kettle Ponds, this dynamic resulted in peak EC water vapor fluxes at 10 meters, suggesting that this height best captures total sublimation rates. Future studies should consider how processes like vertical advection and

blowing snow suspension influence the ideal EC measurement height. While the blowing snow layer may only reach 10 meters at mid-latitude sites like Kettle Ponds [*Pomeroy and Gray*, 1995], it can exceed 50 meters in Antarctica [*Palm et al.*, 2011, 2018].

Our interpretations of the water vapor budget are constrained by potential errors in estimates of vertical turbulent flux divergence (VTFD), vertical advection, and the storage change term. Future research should aim to quantify uncertainties associated with these transport terms. One source of error in the VTFD term may stem from our tilt correction method (Section 2.3.2.3.3.2.3.3), as $\overline{w}$ was correlated with wind direction (Figure 2.8c, g), indicating incomplete rotation into streamwise coordinates. However, we tested several alternative planar fit approaches, including a non-sectorial fit and sectorial fits with 3, 6, and 12 sectors, but none eliminated the persistent nonzero $\overline{w}$ observed during downvalley winds. Notably, downvalley winds were more frequent than upvalley winds (n = 3011 vs. n = 1066 30-minute non-blowing snow periods), and it was under downvalley conditions that we observed consistent water vapor budget closure. This lends confidence to our conclusion that vertical advection is a real and non-negligible transport mechanism at Kettle Ponds.

2.5.4 How reliable is a single EC instrument for measuring sublimation?

We used the net exchange method (Equation 2.7) to improve seasonal sublimation estimates. This method yielded higher totals than the EC method (Figure 2.9) by accounting for positive vertical advection, which is common at Kettle Ponds (Figure 2.8h). Although the method should produce constant surface flux estimates independent of height, results varied with height (Figure 2.9), likely due to two factors. First, the method does not account for blowing snow sublimation, so estimates should increase with height (Section 2.5.2.5.2). Second, water vapor budget non-closure during certain periods (e.g., upvalley winds; Figure 2.8d) implies horizontal advection, which the method also does not account for. As noted by *Finnigan* [1999], omitting horizontal advection from the net exchange equation may lead to worse estimates of surface exchange than the EC method. However, in our case, the negative residual during water vapor budget non-closure implies a positive horizontal advection

term, meaning that including it [as in *Wang et al.*, 2024] would further increase sublimation estimates. Thus, the net exchange method likely improved estimates relative to EC but still underestimated true sublimation.

The variability in total seasonal sublimation introduced by measurement height (±12%, Figure 2.4a) and by use of the net exchange method (+3–7%, Figure 2.9) falls within published EC uncertainty bounds. *Andreas et al.* [2010] estimated ±20% error for EC fluxes over flat snow surfaces, and *Stiperski and Rotach* [2016] suggested up to ±50% over complex terrain. *Sexstone et al.* [2016] estimated seasonal sublimation uncertainty at ±24%. At Kettle Ponds, duplicated seasonal sublimation estimates from four ECs each at 3 and 10 meters had standard deviations of just ±2.8% and ±6.5%, respectively (Figure 2.9), suggesting that real-world uncertainty may be lower than previously estimated. At sites like Kettle Ponds, a single EC at an appropriate height appears sufficient for measuring seasonal sublimation, if it remains functioning throughout the entire season.

In summary, a single EC instrument can reliably estimate seasonal sublimation, particularly if it is deployed near the top of the blowing snow layer. At Kettle Ponds, the EC at 10 meters captured 12% more sublimation than a 3-meter EC because it incorporated more blowing snow sublimation (Section 2.5.2.5.2). For short-term deployments, one EC may be less reliable. During blowing snow conditions, positive VTFD (26% average increase from 3 to 10 meters; up to 200% during individual events) caused low-mounted ECs to underestimate sublimation. During non-blowing snow conditions, negative VTFD (10% average decrease from 3 to 10 meters; 41% from 3 to 15 meters) caused underestimation by higher instruments. While the net exchange method should theoretically adjust for VTFD induced by advection, these processes remain misunderstood, and the method should be applied with caution. To most accurately estimate sublimation in complex terrain and identify if VTFD is important, two ECs at ∼3 and ∼10 meters should be deployed.

2.6 Conclusion

Twelve EC instruments between two and 20 meters AGL on four towers in the Colorado Rocky Mountains, USA, estimated between 26–39 mm SWE sublimated during continuous snow cover, between 30 November 2022 and 8 May 2023 (0.26 mm/day). This amounts to 6–9% of the seasonal maximum snowpack (437 mm SWE). Blowing snow sublimation dominated snow-atmosphere water vapor exchange before the spring equinox, while surface sublimation dominated exchange afterwards.

During blowing snow conditions, EC water vapor fluxes increased with height between 3 and 10 meters (positive vertical turbulent flux divergence, VTFD), with the 10-meter EC measuring, on average, 26% greater sublimation than the 3-meter EC (Figure 2.4d). Estimates of terms in the water vapor conservation equation suggest the existence of a water vapor source term (blowing snow sublimation) that balances the positive VTFD (Figure 2.6). During the most intense blowing snow event of the season, 10-meter (20-meter) measurements doubled (nearly tripled) 3-meter measurements. Our findings suggest that previous EC measurements in blowing snow conditions underestimated total snowpack sublimation losses [consistent with the findings of *Sexstone et al.*, 2018]. Future field campaigns aimed at estimating total snow sublimation should consider deploying an EC instrument at ∼10 meters, below which most blowing snow is suspended [*Pomeroy and Gray*, 1995], although the ideal height to capture total snow sublimation is likely to vary by site.

During daytime, non blowing snow conditions, EC water vapor fluxes decreased with height above 5 meters (negative VTFD) with 10-, 15-, and 20-meter instruments measuring 10, 41, and 36% less sublimation, respectively, than the 3-meter instrument (Figure 2.4c). Estimates of terms in the water vapor conservation equation suggest that vertical advection, which results from negative vertical wind motions and negative near-surface humidity gradients, induces negative VTFD during mid-day, downvalley winds (Figure 2.8). During upvalley winds, the negative VTFD is not balanced by vertical advection. Down (up) valley winds occur 49% (24%) of the time at our field site, implying that our estimates of

transport processes closed the water vapor budget more often than not. Instances of water vapor budget non-closure (during daytime upvalley winds and occasionally during nighttime downvalley winds) suggest that unresolved water vapor transport processes, such as horizontal advection, are important at the field site.

We attempted to refine our estimates of total snow sublimation by using the net exchange method [e.g. *Lee*, 1998], which increased estimates of total snow sublimation 3–7% (5.5% on average) relative to the EC method. The observed water vapor budget non-closure and implied horizontal advection, as discussed above, suggest that the net exchange equation still underestimates total snow sublimation. Future studies could refine seasonal sublimation estimates further by estimating blowing snow sublimation and horizontal advection, and incorporating both terms into the net exchange method.

Total seasonal sublimation at our site was relatively small, approximately 10% of seasonal snow accumulation. However, our observations suggest that a single EC deployed for shorter than a full season cannot reliably estimate seasonal sublimation because water vapor fluxes in complex terrain vary substantially in space and time. Seasonal variation in net radiation and energy availability mean that short field campaigns are unlikely to represent seasonally averaged surface sublimation. Intermittent blowing snow also varies seasonally, and, during large blowing snow events, blowing snow sublimation leads to positive flux divergence and ECs at standard measurement heights of 3–5 m may underestimate total sublimation. Finally, complex terrain generates vertical air motion and, potentially, horizontal humidity gradients that drive water vapor advection, which leads to flux divergence near the surface. Unresolved horizontal advection processes warrant further research. For the purposes of estimating seasonal sublimation, a single EC instrument mounted near the top of the blowing snow layer is sufficient.

Acknowledgments

We would like to thank the Rocky Mountain Biological Laboratory for their facilitation of the field site, and billy barr, for his detailed logs of weather conditions in the East River valley.

We also thank the NCAR EOL team for making the field experiment possible. We also thank Michael Haugeneder, Edwin Rainville, Alex Horner-Devine, Michelle DiBenedetto, Elie Bou-Zeid, and Dale Durran for discussions that deepened our understanding and led to this publication. This work was supported by National Science Foundation Awards 2139836 and 2139809. This material is based upon work supported by the NSF National Center for Atmospheric Research, which is a major facility sponsored by the U.S. National Science Foundation under Cooperative Agreement No. 1852977. Chris Cox and Brian Butterworth received support from the NOAA Physical Sciences Laboratory, including through the NOAA cooperative agreements with CIRES NA17OAR4320101 and NA22OAR4320151, as well as from the U.S. Department of Energy Atmospheric Systems Research award DE-SC0024266.

Data availability

Data from the Sublimation of Snow Campaign are available online [*NSF NCAR/EOL ISFS Team*, 2024].

2.7 Appendix A: Conditions during which flux data were discarded

We removed 30-minute EC water vapor fluxes (henceforth, fluxes) when $> 25\%$ of 20 Hz measurements were flagged by the sonic anemometer or IRGA (Section 2.3.2.3.3). Of all fluxes discarded due to sonic flags, 84% occurred during blowing snow or snowfall, and 71% during a single event on 21–22 December 2022. 51% of IRGA-flagged fluxes occurred during blowing snow or snowfall, 65% when RH $> 89\%$, and 18% during sunny, spring days. All results refer to the 3-meter, tower C EC; similar results were found at 10 m. Of the four most intense blowing snow events (based on daily mean FlowCapt flux), only the most intense (21–22 December) event caused loss of 30-minute fluxes, due to sonic flags. During the event's peak, 50% of 20 Hz measurements were flagged over several hours. Data removal and gap-filling reduced event-total sublimation estimates from 2.1 mm (raw) to 1.9 mm (cleaned, gap-filled). Only one top-4 event (13–15 December) had many IRGA flags, with, at worst, only 2.7% of 20 Hz measurements flagged per 30-minute flux, so no data was removed. These

results suggest that blowing snow only considerably impacted EC sublimation estimates during the most intense event. We attribute minimal data loss to the site's dry air, which limited condensation on instruments, and relatively low blowing snow intensities (relative to Antarctica, alpine passes, Sigmund et al., 2022, Trouvilliez 2015). Blowing snow fluxes also decrease exponentially with height (Figure 2.6a), so particle densities at elevated ECs were likely inconsequential.

2.8 Appendix B: Implementation of the horizontal advection term

We estimated horizontal advection (Equation 2.3) using a finite difference approximation,

$$\overline{u}\frac{\partial\overline{\rho_v}}{\partial x} = \overline{u}\frac{\Delta\overline{\rho_v}}{\Delta x} \tag{2.8}$$

where $\overline{u}$ is 3-meter wind speed at Kettle Ponds, $\Delta\overline{\rho_v}$ is the difference in absolute humidity between Annex and Kettle Ponds, and $\Delta x = 400$m is the distance between the sites (Figure 1d). Positive $\overline{u}$ points downvalley, so $\Delta\overline{\rho_v} = \overline{\rho_v}_{Annex} - \overline{\rho_v}_{KettlePonds}$. We only calculate horizontal advection when winds are up or downvalley (Section 2.2.2.2.1).

2.9 Appendix C: Uncertainty estimates for vertical and horizontal advection

To evaluate uncertainty in vertical and horizontal advection ($\overline{w}\frac{\partial\overline{\rho_v}}{\partial z}$ and $\overline{u}\frac{\partial\overline{\rho_v}}{\partial x}$; Equation 2.3), we estimated uncertainty in $\Delta\overline{\rho_v}$, which appears in finite difference approximations to the terms, $\overline{w}\frac{\Delta\overline{\rho_v}}{\Delta z}$ and $\overline{u}\frac{\Delta\overline{\rho_v}}{\Delta x}$. We compared this uncertainty to measured vertical and horizontal gradients to assess whether the gradients differ significantly from zero. We calculated $\overline{\rho_v}$ from pressure (P), temperature (T), and relative humidity (RH). Using a Monte Carlo approach (n = 5000), we propagated manufacturer-reported uncertainty — 0.01% for P (relative error), 0.1°C for T and 1.5% for RH (both absolute error) — into an uncertainty for $\overline{\rho_v}$. Random samples of P, T, and RH were drawn from normal distributions with $2 * std$ equal to the manufacturer-reported uncertainties (Figure 2.10a–c). For distribution means, we used measurements from a timestamp with the seasonal-median temperature (1400 5 Jan 2023; T = −6.7°C, P = 720 mb, RH = 65%). From the three distributions, we generated

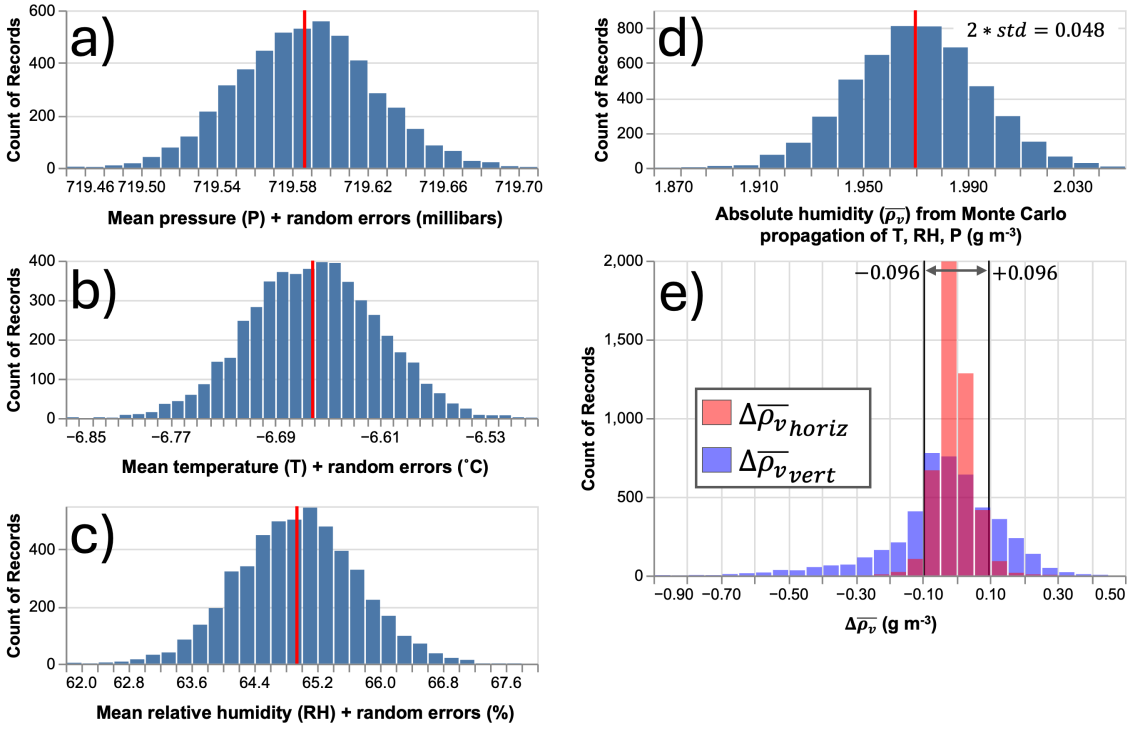

Figure 2.10: Monte Carlo error propagation for estimating error in horizontal and vertical absolute humidity gradients, $\Delta\overline{\rho_v}$. We generated fake, normally-distributed samples (n=5000) for pressure (a), temperature (b), and relative humidity (c), using the manufacturer reported error as two times the standard deviation for the sampling distribution. From those sample distributions, we generated a sample distribution of $\overline{\rho_v}$ (d). We then calculated horizontal gradients (e) in $\overline{\rho_v}$ from measurements at 3 meters at Kettle Ponds and Annex and vertical gradients (e) from 20-meter and 2-meter measurements at Kettle Ponds (Figure 2.1) from all 30-minute averaging periods during the study period. The estimated error in the gradients (0.096 g m^{-3}) is shown.

a $\overline{\rho_v}$ distribution (Figure 2.10d) and calculated uncertainty as $2 * std = 0.048$ g m^{-3}. Since advection terms involve $\Delta\overline{\rho_v}$, its uncertainty is double the estimated $\overline{\rho_v}$ uncertainty of 0.048, 0.096 g m^{-3}. We computed measured vertical ($\Delta\overline{\rho_{v_{vert}}}$, between 2 and 20 m) and horizontal ($\Delta\overline{\rho_{v_{horiz}}}$, Kettle Ponds-Annex) gradients for all 30-minute time steps (distributions shown in Figure 2.10e). 94% of $\Delta\overline{\rho_{v_{horiz}}}$ values fall within the $\Delta\overline{\rho_v}$ uncertainty of $\pm$0.096 g m^{-3}, compared to 42% for $\Delta\overline{\rho_{v_{vert}}}$, indicating that horizontal gradients are rarely distinguishable from zero, whereas vertical gradients often are.

Chapter 3

ELEVATED SHEAR LAYERS AND TOP-DOWN TURBULENCE INCREASE SURFACE-ATMOSPHERE EXCHANGE IN SNOW-COVERED COMPLEX TERRAIN

3.1 Introduction

Accurately predicting fluxes of heat, moisture, and momentum in mountains remains a challenge due to the complicated dynamics of atmospheric flow over complex terrain [*Stiperski et al.*, 2019; *Foken*, 2006; *Serafin et al.*, 2018]. While the influence of orographic drag on synoptic atmospheric flow has been modeled with gravity-wave parameterizations, the influence of orographic flows on turbulent fluxes in the boundary layer remains comparatively underexplored [*Vosper et al.*, 2018]. Of particular interest are fluxes over snow-covered complex terrain, since mountain snowpacks provide water for much of the world's populations [*Viviroli et al.*, 2007]. Accurately parameterizing fluxes in such environments is critical to predicting evaporation, sublimation, boundary layer evolution, and improving the performance of numerical weather models [*Kötsche et al.*, 2025; *Litt et al.*, 2015]. However, both the complex terrain and snow-cover pose significant challenges to estimating surface fluxes.

Surface fluxes are generally parameterized in numerical weather and land surface models with Monin-Obukhov Similarity Theory (MOST), which assumes that turbulent fluxes scale with the shear generated over a flat, homogeneous surface (surface-shear driven turbulence) [*Stull*, 1988; *Monin and Obukhov*, 1954]. However, flow over complex terrain does not satisfy the mandatory assumption of horizontal homogeneity that underpins MOST, and improving our understanding of how heterogeneities impact near-surface fluxes requires observations on the scale of both orographic flows and surface fluxes. Unfortunately, such observations are limited, although recent field campaigns have begun to observe some important orographic

flow-surface interactions. For example, *Lehner et al.* [2019] used Doppler lidar and meteorological tower measurements to characterize a turbulent wake that formed on the lee side of a crater rim and eroded the surface inversion within the crater. *Schwat et al.* [2025] used measurements from four towers to identify vertical advection of dry air towards the surface and increased surface sublimation rates associated with thermal valley winds. *Stiperski et al.* [2019] identified the effects of of turbulence anisotropy on near-surface turbulent fluxes. Other studies have also combined instruments across scales to yield new insights [*Babić et al.*, 2024, 2021; *Bell et al.*, 2020]

In the case of atmospheric flow over snow-cover, when the surface layer is mostly stable, models tend to underpredict near-surface turbulent mixing, which can result in a positive feedback of increased surface cooling, increasing stability, and decreased mixing [*Lapo et al.*, 2019; *Slater et al.*, 2001]. In the nocturnal stable boundary layer over flat terrain, measurements suggest that shear and turbulence intensification can result from breaking gravity waves, which result in a propagation of turbulent energy downwards to the surface [*Sun et al.*, 2012]. In this so-called "top-down" turbulence regime, near-surface turbulence and surface fluxes are underpredicted by MOST, and turbulence-intensifying wave events are not represented in modern weather models [*Sun et al.*, 2015]. Like breaking waves in the stable boundary layer, orographic flows, such as valley winds, mountain waves, and rotors, generate shear above the surface [*Doyle and Durran*, 2007; *Vosper et al.*, 2018; *Rotach et al.*, 2008]. In snow-covered complex terrain, where the boundary layer is often stable or neutral [*Adler et al.*, 2023], shear generated by such orographic flows could increase near-surface turbulence and exchange rates. *Vosper et al.* [2018] suggested that mountain waves and rotors could advect turbulence down towards the surface, resulting in near-surface turbulence that does not arise from wind shear against the surface, as MOST assumes. Such coherent, large-scale eddies carrying warm, dry air towards the surface have been observed [*Litt et al.*, 2015].

Based on the literature, we would expect orographic flows to produce turbulence and impact boundary layer processes in complex terrain, particularly when the boundary layer is stable. To determine if this is indeed the case, we observed interactions between oro-

graphic flows and surface turbulence using measurements from the site- to valley-scale from three synchronous field campaigns in the mountainous, high-altitude upper East River Valley, Colorado, USA, in winter and spring 2022–2023. In this study, we test the following hypotheses:

1. Turbulence measured on the valley-floor is increased by top-down effects.

2. Top-down effects vary in time. Top-down turbulence is more common when synoptic winds are oriented perpendicular to ridges (cross-valley) due to wind shear at ridge-height.

3. During top-down turbulence, surface fluxes of heat, moisture, and momentum are underpredicted by MOST.

The results in this study are organized as follows: We first describe our study area, measurements, and methods. Then, we characterize the mean wind conditions above and within the upper East River Valley, and categorize synoptic wind observations into "cross-valley" and "along-valley" categories. We then examine seasonal turbulence statistics from near-surface eddy covariance (EC) and valley-scale Doppler lidar measurements to identify when top-down turbulence dominates near-surface flow or standard, surface-shear driven turbulence dominates that flow. We then present two case study days, which exemplify the distinct surface-shear and top-down turbulence regimes and illustrate orographic flow phenomena that can lead to top-down turbulence. Finally, we compare modeled and measured surface fluxes during top-down turbulence and discuss the implications of the tests performed on our hypotheses.

3.2 Study area and instrumentation

For this study, we incorporated measurements from three field campaigns that took place in the East River Valley of the Rocky Mountains, CO, USA (Figure 3.1d). The Sublimation of Snow (SOS) campaign deployed four instrument towers at the Kettle Ponds site (KPS,

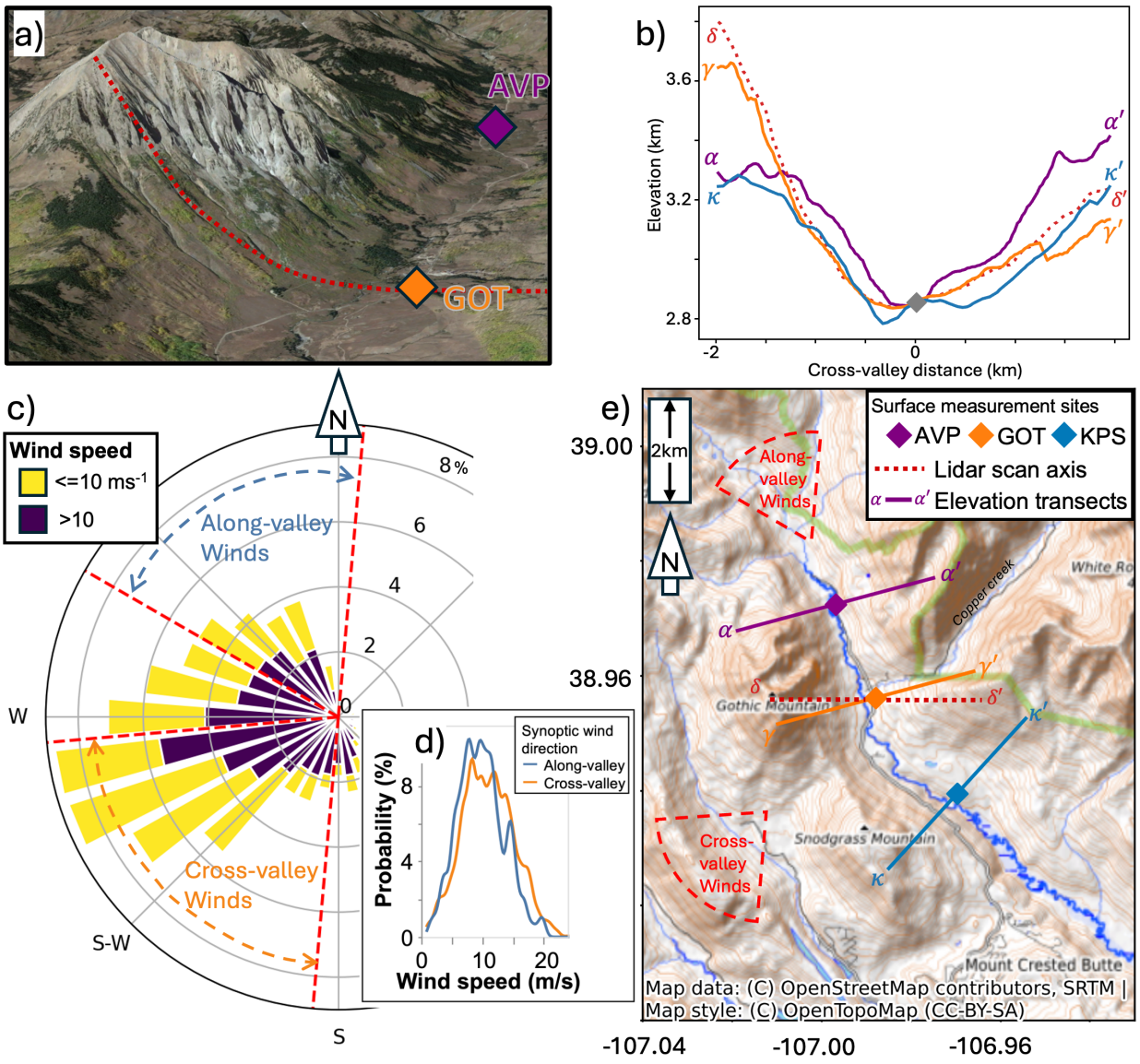

Figure 3.1: *Caption on next page.*

Figure 3.1: Measurement sites and seasonal synoptic wind conditions in the East River Valley. (a) Oblique, Google Earth view of Gothic Mountain, the tallest feature in the East River Valley, and the Doppler lidar scanning axis. (b) Elevation transects of valley cross-sections aligned with the three measurement sites in panel d. AVP and GOT elevation values were adjusted downward so elevations at measurement sites (at cross valley distance of 0) are equal. (c) Wind rose of synoptic winds measured between 30 November 2022 and 15 June 2023. Synoptic winds are measured by the Doppler lidar at the GOT site and are calculated as the mean 1–1.5 km winds. The along- and cross-valley wind direction categories used in this study are outlined with red dashed lines. (d) Distributions of wind speeds for the two wind direction categories, calculated from the kernel density estimate. (e) Topography of the study area and the three surface measurement sites. The red dashed line, extending ± 2 km to the east and west of GOT, indicates the scanning axis for the Doppler lidar relative height indicator (RHI) scans presented in this study, also shown in panel a. Solid lines show the footprints of elevation transects presented in panel b.

Figure 3.1) [*Lundquist et al.*, 2024; *Schwat et al.*, 2025]. We used measurements from eddy covariance (EC) instruments placed between 3–20 meters above ground level (AGL) on the campaign's central tower [*Lundquist et al.*, 2024]. We also incorporated measurements of humidity from a hygrothermometer placed three meters AGL.

The Study of Precipitation, the Lower Atmosphere and Surface for Hydrometeorology (SPLASH) campaign operated multiple flux and micrometeorological towers during the same period and in the vicinity of the SOS campaign [*Boer et al.*, 2023; *Cox et al.*, 2025b]. We used EC and temperature measurements from the SPLASH Avery Picnic site (AVP, Figure 3.1). Their EC instrument and temperature sensor were placed 4.6 and 2.9 meters AGL, respectively.

The Surface Atmosphere Integrated Field Laboratory (SAIL) campaign [*Feldman et al.*,

2023] also coincided with the SOS and SPLASH campaigns. We used EC measurements from their Gothic measurement site (GOT, Figure 3.1) [*Sullivan et al.*, 1997a]. The GOT EC was mounted at 3.5 meters AGL. We also incorporated measurements from SAIL's twice-daily rawinsondes (released at approximately 04:30 and 16:30 LT) and Doppler lidar scans. The Doppler lidar was deployed at the GOT measurement site (Figure 3.1c), and the rawinsondes were released from nearby the GOT site [*Feldman et al.*, 2023]. For Doppler lidar and rawinsonde measurements, we refer to heights above the Doppler lidar, which was placed on top of a shipping container on the valley floor at an elevation of 2886 masl. Gothic Mountain, the tallest feature in the vicinity, is 960 m above the Doppler lidar, and Snodgrass Mountain is approximately 510 m above (Figure 3.1a and e).

At all sites, during the 2022-2023 snow-covered season, snow depth varied between 0 and 2 meters. Thus, instrument heights above the snow surface were frequently less than the heights above the ground described above. On-site technicians removed snow from the Doppler lidar daily, ensuring the instrument was not obstructed.

3.3 Methods

For this study, we included data between 30 November 2022 and 10 May 2023, the approximate dates during which snow covered the valley floor [*Schwat et al.*, 2025]. We analyzed Doppler lidar measurements to characterize the speed, direction, and turbulent intensity of atmospheric boundary layer flow within and above the valley. We used near-surface EC measurements to characterize mean flow and turbulence on the valley floor.

3.3.1 Doppler lidar measurements

Mean horizontal winds

Vertical profiles of horizontal wind speed and direction were extracted at a 28 meter vertical resolution [*Shippert et al.*, 2022] from Doppler lidar plan position indicator scans [*Newsom and Krishnamurthy*, 2022], performed every 15 minutes throughout the study period. Hori-

zontal speed (U) and direction (Dir) were extracted from scans using the Velocity-Azimuth Display algorithm [*Newsom et al.*, 2017], between 0–2000 meters AGL. We downsampled the 15-minute measurements to 30-minute resolution via block-averaging to match the resolution of eddy covariance measurements (Section 3.3.2).

Mean wind shear

To characterize shear within the valley, we calculated the gradient in wind speed (dU/dz) and wind direction ($dDir/dz$), which describe shear due to changes in wind speed and shear due to changes in wind direction (rotational shear). Both are calculated using the finite difference approximation between the vertically-spaced measurements of horizontal wind speed and direction described above.

Vertical velocity statistics

Vertical profiles of vertical velocity variance ($\overline{w'w'}$) and skewness ($\overline{w'w'w'}$) were extracted from the Doppler lidar's vertically-staring scans [*Newsom and Krishnamurthy*, 2022], which lasted 20 minutes of every hour. $\overline{w'w'}$ contributes to TKE, and represents the intensity of vertical turbulent mixing. $\overline{w'w'w'}$ represents the vertical turbulent transport of $\overline{w'w'}$. Negative $\overline{w'w'w'}$ represents downdrafts, and positive $\overline{w'w'w'}$ represents updrafts, as in a convective boundary layer. Doppler lidar statistics were calculated using 10-minute Reynolds averaging periods and are provided at 30 meter vertical resolution [*Shippert et al.*, 2010].

Two-dimensional scans

Two-dimensional scans of radial velocity were collected by range height indicator (RHI) scans. RHI scans produce a vertically oriented plane of radial velocity values, which characterize a vertical slice of the atmospheric wind field. Throughout the SAIL campaign, RHI scans were performed on an east-west axis (approximately cross-valley, Figure 3.1c). Prior to 11 February 2023, the scans were taken once per hour. After this date, scans were taken four

times per hour, starting at 00:15, 00:18, 00:45, and 00:48, per interests expressed by the SAIL science team to better enable turbulence science. For all RHI scans, the Doppler lidar scanned in 1 degree elevation angle increments, from zero to 180 degrees (i.e. starting horizontally, pointing to the west, and ending horizontally, pointing to the east). At each elevation degree, the RHI scan collects radial (along-beam) velocity measurements with a range-gate (resolution) of 30 meters. Each RHI scan takes approximately 90 seconds to complete. The footprint of the RHI scan pattern over the topography, with a range of ± 2 km, is shown in Figure 3.1e.

Classification of synoptic winds

We categorized all data using Doppler lidar wind speed and direction measurements. "Synoptic winds" refer to the mean 1–1.5 km AGL winds, which are above ridges near the GOT site where the doppler lidar was deployed (Figures 3.1b and e). Each 30-minute period was labeled as cross-valley (185–265°) or along-valley (300—5°), and further classified as "fast" (> 10 m s^{-1}) or "slow" (≤ 10 m s^{-1}) ((Figures 3.1c). We selected the range of cross-valley synoptic flow directions such that Gothic and Snodgrass mountains were upwind of the GOT site (Figures 3.1c and e). We selected the range of along-valley synoptic flow directions to ensure that the upwind fetch for all three sites lay within the valley. We excluded data outside these categories to avoid cases where it was unclear whether synoptic winds crossed westward ridges before reaching the GOT site.

Data quality and classification of synoptic winds

Doppler lidar data quality depends on atmospheric aerosol concentration: too few aerosols reduce backscatter, while too many degrade returns. Quality is typically assessed using the signal-to-noise ratio. The mean horizontal wind, vertical velocity statistics, and RHI scans are filtered to remove data with a signal-to-noise ratio below 0.008 [*Shippert et al.*, 2010, 2022]. During our study period, data quality was generally high. Of the 7778 30-minute periods between 30 November 2022 and 10 May 2023, the Doppler lidar PPI scans

provided 1-1.5 km AGL synoptic wind speed and direction values for 5168 periods (66% of the time). To aid in categorizing our datasets into the cross-valley, along-valley, fast, and slow synoptic wind categories, we used measurements of mean 1–1.5km AGL wind speed and wind direction from rawinsondes (weather balloon), which were released near the GOT site twice daily at approximately 04:30 and 16:30 LT [*Keeler et al.*, 2022a]. Rawinsonde measurements were used to fill any missing doppler lidar measurements at 04:30 and 16:30 LT. We then filled remaining gaps in the synoptic wind speed and direction timeseries with the forward-filling method, carrying forward the last valid value, for gaps up to 3 hours long. After these gap-filling steps, we were able to categorize synoptic winds for 6576 of 7778 30-minute periods (85%). Missing data were fairly evenly distributed across the study period, with 79–84% of data available in December–March and 92% in April.

3.3.2 Near-surface eddy covariance measurements

In this analysis, we used EC measurements of mean horizontal wind speed, mean horizontal wind direction, and turbulent kinetic energy ($TKE = \frac{1}{2}\left(\overline{u'u'}^2 + \overline{v'v'}^2 + \overline{w'w'}^2\right)$) from the KPS, GOT, and AVP sites. We also calculated a turbulent velocity scale, $V_{TKE} = \sqrt{TKE}$. We used EC measurements of latent heat (water vapor) and sensible heat fluxes from the KPS site exclusively. EC measurements from the three sites were processed separately [*Cox et al.*, 2025b; *Sullivan et al.*, 1997a; *Schwat et al.*, 2025]. Means and covariances at the KPS and GOT sites were computed using a 30-minute averaging period, consistent with the recommendations of *Schwat et al.* [2025] for this time period. Means and covariances at AVP were calculated with 10-minute averaging period, and block-averaged to 30-minutes. KPS and AVP EC measurements were tilt-corrected using the planar fit method and GOT measurements were tilt-corrected with the double rotation method [*Wilczak et al.*, 2001; *Schwat et al.*, 2025; *Cox et al.*, 2025b]. The tilt correction method generally has negligible impacts on mean wind speed and wind direction, and no impact on TKE.

Spectra calculated with the Multiresolution Decomposition method

We calculated cospectra of the streamwise turbulent momentum flux, $Co(\overline{u'w'})$, from high resolution sonic anemometer data to characterize turbulence at the three EC measurement sites. GOT EC data were collected at 10-Hz resolution. KPS and AVP data were collected at 20-Hz, and we block-averaged the data to 10-Hz. We calculated cospectra using the sliding window multiresolution decomposition (MRD) method [*Howell and Mahrt*, 1997; *Vickers and Mahrt*, 2003; *Haugeneder et al.*, 2024]. For each day, we calculated a sequence of cospectra, with each cospectra calculated for a window of 2^{14} 10-Hz data points, which is equal to 27.31 minutes (the MRD method requires record lengths that are powers of two). Consecutive windows were shifted by 120 seconds. This generates a time series of cospectra (cospectrogram). For each window, EC data were rotated into the mean streamline coordinate system using the double rotation method [*Wilczak et al.*, 2001; *Kaimal and Finnigan*, 1994].

3.3.3 Two-dimensional flow simulations

To simulate realistic turbulent flow fields for comparison to the Doppler lidar observations, we used a model based on the two-dimensional Lattice Boltzmann Method [LBM; see *Chen and Doolen*, 1998] to solve the Navier-Stokes equations. The LBM represents fluid motion using a set of particle distribution functions, $f(x, y, t)$, which evolve on a discrete velocity lattice. The model used here is solved on a D2Q9 lattice (9-"particles" per grid cell in a two-dimensional plane) and is designed to simulate turbulent flow over variable topography. The velocity field is recovered from the first moments of $f(x, y, t)$ and density from the zeroth moment. The macroscopic density and velocity fields are reconstructed after each time step and used to recompute equilibrium particle distributions. The fluid's kinematic viscosity is controlled through relaxation times using the Bhatnagar Gross Krook formulation, here fixed at 1000 with a background wind speed on the upwind and top boundaries of 10 m/s [*Bhatnagar et al.*, 1954]. The bottom boundary condition uses an immersed boundary method. The LBM

bounce-back boundary conditions are applied to f at solid boundaries, creating a no-slip (zero velocity) boundary condition. This allows for irregular, spatially varying terrain. Topography is specified by a 1D slice through the topography over Gothic Mountain consistent with the Doppler lidar cross-section and aligned with the dominant wind direction (red dotted line in Figures 3.1a, b, and e). The LBM model is discretized on a 6 m (x and z) grid. The model does not include temperature stratification and is not meant to provide a representation of real world conditions. We exclusively used the model to help interpret flow structures observed in Doppler lidar RHI scans.

3.3.4 Model predictions of turbulent fluxes

In this paper, we compared measured and modeled latent heat fluxes. We modeled fluxes using the bulk aerodynamic parameterization of MOST presented in *Andreas et al.* [2010], which avoids complete suppression of turbulence in very stable conditions by setting a minimum wind speed of 0.5 m/s. A critical parameter for the parameterization is the aerodynamic roughness length (z_0) and the corresponding humidity roughness (z_q) and temperature roughness (z_T) lengths. We estimated z_0 from eddy covariance measurements [*Cox et al.*, in review, their Equation 5] and found a value of 0.0002 meters, consistent with the findings of *Cox et al.* [in review]. We estimated z_q and z_T from z_0 using the roughness-length ratio parameterization of *Andreas* [1987]. We predicted fluxes using meteorological measurements at the KPS site.

3.4 Results

3.4.1 Seasonal analysis

Mean winds

During our study period, synoptic winds were predominantly from west-southwest, with west-northwesterly winds also common (Figure 3.1c). Of the 30-minute periods during which we measured synoptic winds (Section 3.3.1), 38% and 21% were in the cross-valley and along-

valley categories, respectively. Cross-valley synoptic winds were faster than 10 m/s ("fast" synoptic winds) 56% of the time, along-valley synoptic winds 45% of the time. The cross-valley category had slightly faster winds, on average, than the along-valley category (Figure 3.1d).

Near-surface turbulence

To characterize near-surface turbulence during the distinct synoptic wind categories, we examined the relationship between V_{TKE} and wind speed (Figure 3.2). During along-valley synoptic winds, regardless of synoptic wind speed, the relationship between V_{TKE} and wind speed was approximately linear, and V_{TKE} values stayed below 2 m/s. This relationship persisted across the three sites, although V_{TKE} values were, on average, lower at AVP. During cross-valley synoptic winds, particularly fast cross-valley, V_{TKE} was elevated, and varied with wind speed non-linearly. At the GOT and KPS sites, the distributions of V_{TKE} during fast cross-valley synoptic winds were especially distinct from the distributions during along-valley synoptic winds. Cross-valley synoptic winds are also responsible for most of the high V_{TKE} outliers observed at low wind speeds at the GOT and AVP sites.

To examine the structure of near-surface turbulence during the four synoptic wind categories, we calculated the mean daily composite spectrogram for streamwise momentum fluxes from all days that fall into each of the four synoptic wind categories. We categorized each day during the study period using the mean daily synoptic wind speed and direction. During along-valley synoptic winds, both fast and slow, momentum flux cospectral power ($Co(\overline{u'w'})$) is nearly entirely negative and concentrated at small scales (Figure 3.3a and c). Negative momentum fluxes indicate that the turbulence is interacting with the surface, which acts as a momentum sink and causes wind shear. During fast cross-valley synoptic winds, $Co(\overline{u'w'})$ was mostly negative, but negatives fluxes contained little cospectral power; and this category was distinguished by frequent spikes of positive cospectral power at large scales ($\tau > 200$ seconds, Figure 3.3b). Positive momentum fluxes indicate that the measured flow is not following classical theory for the surface layer (i.e. log-profile of wind velocity). During slow

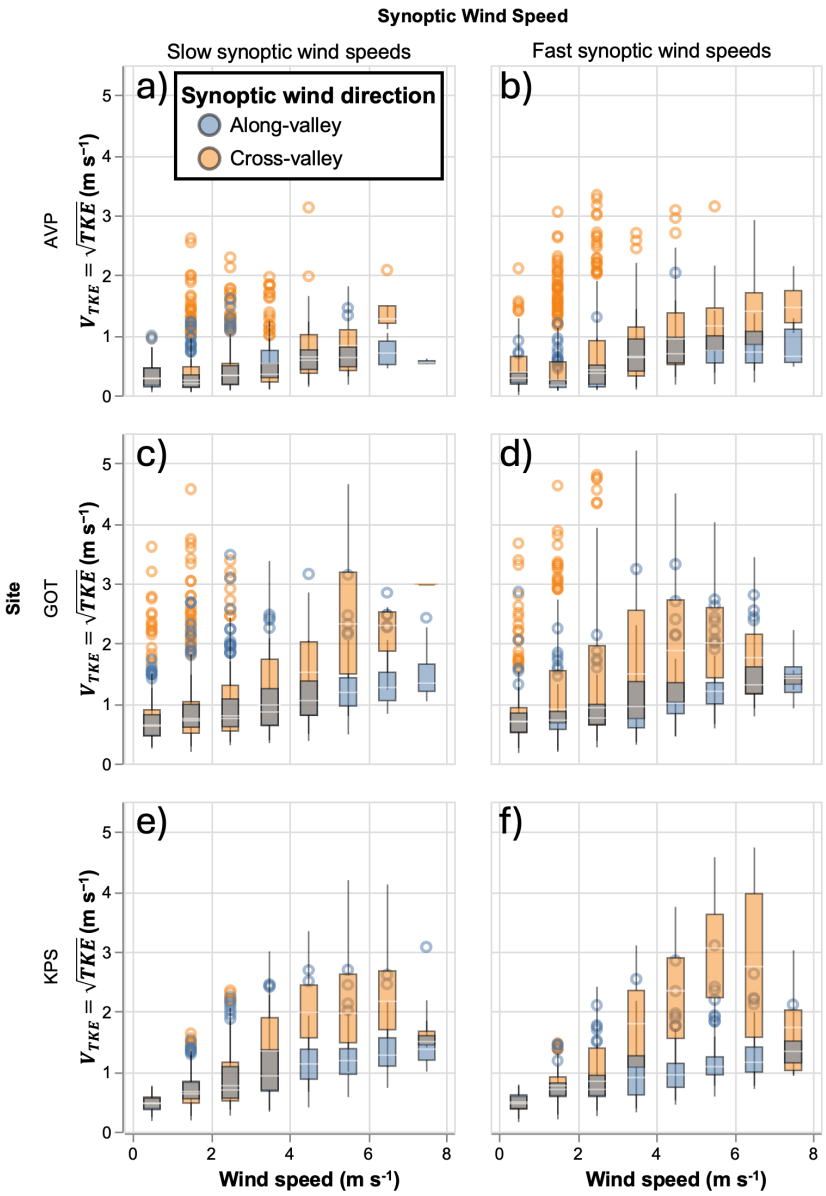

Figure 3.2: Distributions of V_{TKE} for binned wind speeds, measured at three sites, (a) and (b) AVP, (c) and (d) GOT, (e) and (f) KPS. The box plots include medians (white lines), interquartile range (box), 1.5 times the interquartile range (whiskers), and outliers (circles). Includes all data from the study period that are in the along-valley and cross-valley synoptic wind direction categories. Data is split into categories based on synoptic wind speed. (a), (c), and (e) includes data during slow synoptic wind speeds ($\leq$ 10 m/s). (b), (d), and (f) includes data during fast synoptic wind speeds ($\geq$ 10 m/s).

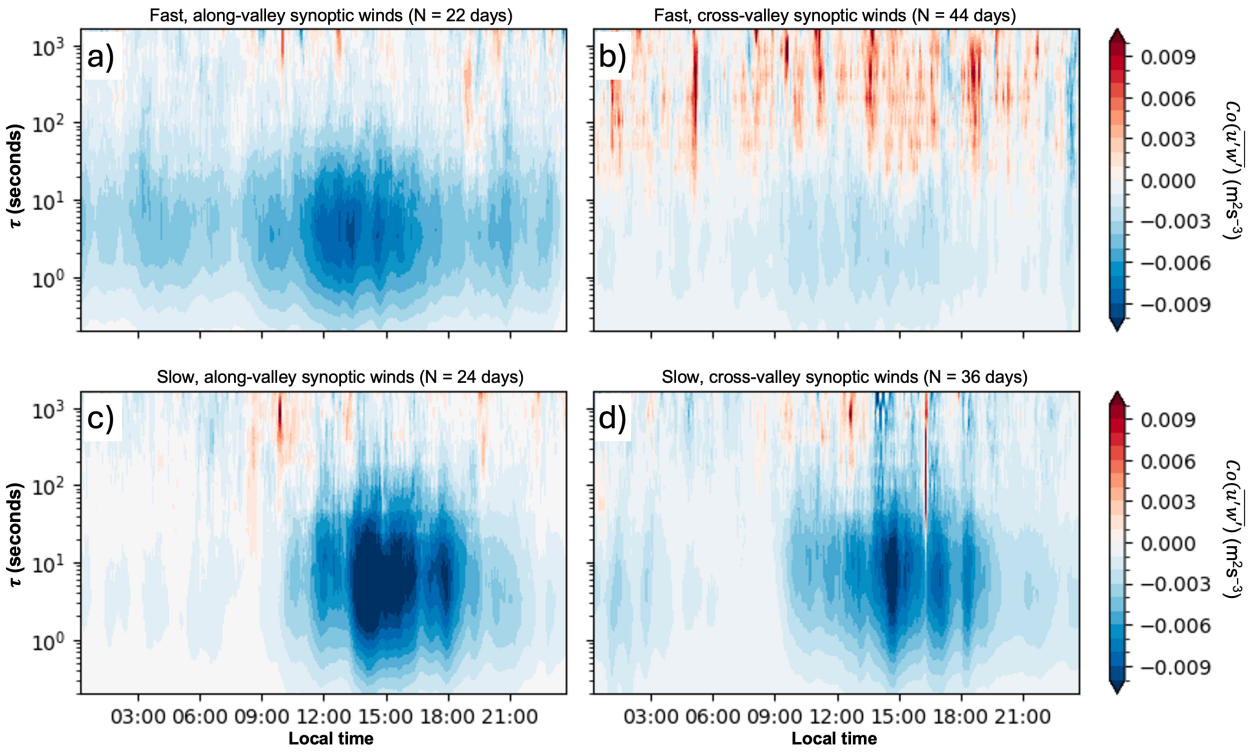

Figure 3.3: Daily composite (mean) cospectrograms of streamwise momentum flux from EC measurements at the KPS site, categorized by daily mean synoptic wind speed and direction. 126 of the 198 days in our study period had daily mean wind direction in our two categories.

cross-valley synoptic winds, the cospectra was similar as during slow, along-valley synoptic winds. For all categories, a diurnal cycle was apparent, with increased negative momentum fluxes at small scales between 09:00–19:00.

Valley-scale turbulence and shear

To examine the structure of valley-scale turbulence and shear, we plotted vertical profiles of $\overline{w'w'}$, $\overline{w'w'w'}$, dU/dz, and $dDir/dz$ (Figure 3.4). For each variable, we calculated separate distributions for the wind direction (separated by color) and wind speed (separated by panel) categories. The height of the top of Gothic and Snodgrass, the two tallest features upwind of the doppler lidar (Figure 3.1e), are indicated on the plots. During both slow and fast cross-valley synoptic winds, $\overline{w'w'}$ peaked at the height of the Gothic ridge, and $\overline{w'w'}$ was larger during fast synoptic wind speeds (Figure 3.4a and b, orange dots). This peak corresponds to a peak in wind shear at the height of Gothic during cross-valley winds (Figure 3.4c and d, orange dots). During along-valley winds, regardless of wind speed, there is no distinct peak in $\overline{w'w'}$ around ridge height (Figure 3.4a and b, blue dots), and the shear profiles during along-valley winds also lack a ridge-height peak (Figure 3.4c and d, blue dots).

During slow and fast cross-valley synoptic winds, $\overline{w'w'w'}$ is slightly negative below the Gothic and Snodgrass ridge heights, and positive above Gothic (Figure 3.4e and f, orange dots). These measurements indicate that downdrafts were common below the Gothic ridge height and updrafts were common above. During slow and fast along-valley synoptic winds, $\overline{w'w'w'}$ was slightly positive near the surface, nearly zero between Snodgrass and Gothic, and positive above Gothic (Figure 3.4e and f, blue dots). The spread in $\overline{w'w'w'}$ was large and always included zero, probably because higher moments have higher uncertainties (i.e. the uncertainty in w'^n grows with n). We discuss the 18 April profiles (black lines) later.

During cross-valley winds, rotational shear was relatively large between 0 and 750 meters AGL; during along-valley winds, rotational shear was relatively weak, but was strongest near the surface (Figure 3.4g and h, blue dots).

To examine how the valley-scale turbulence structure varied across day and night, we also

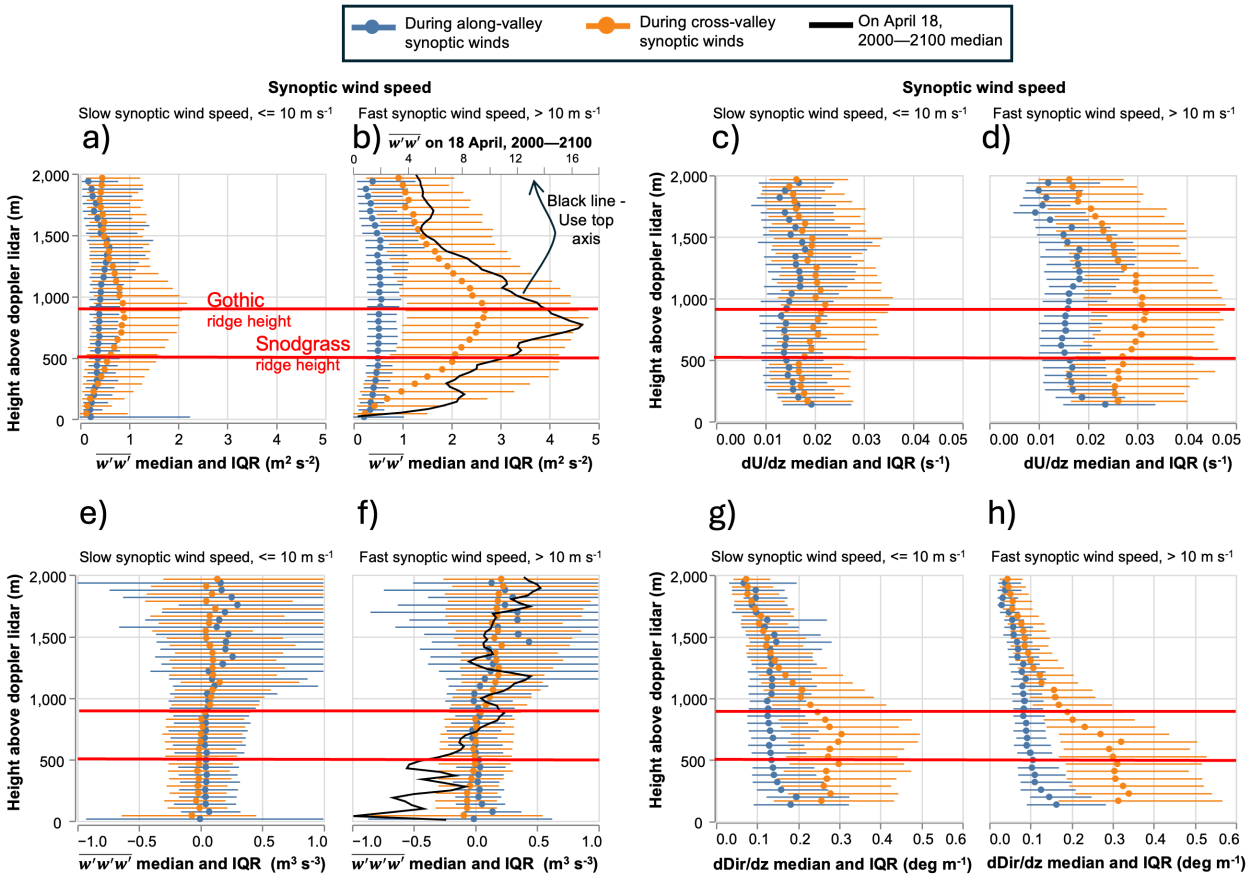

Figure 3.4: Vertical profiles of vertical wind velocity statistics and shear variables. For all plots, we show the median (circles) and interquartile range (IQR, lines). of $\overline{w'w'}$ and $\overline{w'w'w'}$ measured by the Doppler lidar vertical staring mode. Color indicates synoptic wind direction. (a) and (b) profiles of $\overline{w'w'}$. In (b), the mean profile for one hour on 18 April 2023 is shown with the black line, which corresponds to the x-axis on the top of the panel. (e) and (f) profiles of $\overline{w'w'w'}$. In (f), the mean profile for one hour on 18 April 2023 is shown with the black line. (c) and (d) profiles of dU/dz, wind shear. (g) and (h) profiles of $dDir/dz$, rotational wind shear.

plotted $\overline{w'w'}$ profiles for data collected between 04:00–05:00 and 16:00–17:00 (Figures 3.5a and b). These times represent the nighttime and daytime boundary layers, respectively, and overlap in time with the twice-daily rawinsonde (weather balloon) releases. We compared the night and day time $\overline{w'w'}$ profiles with profiles of potential temperature collected by the rawinsondes (Figures 3.5c and d). During both day and night, the $\overline{w'w'}$ profiles peaked

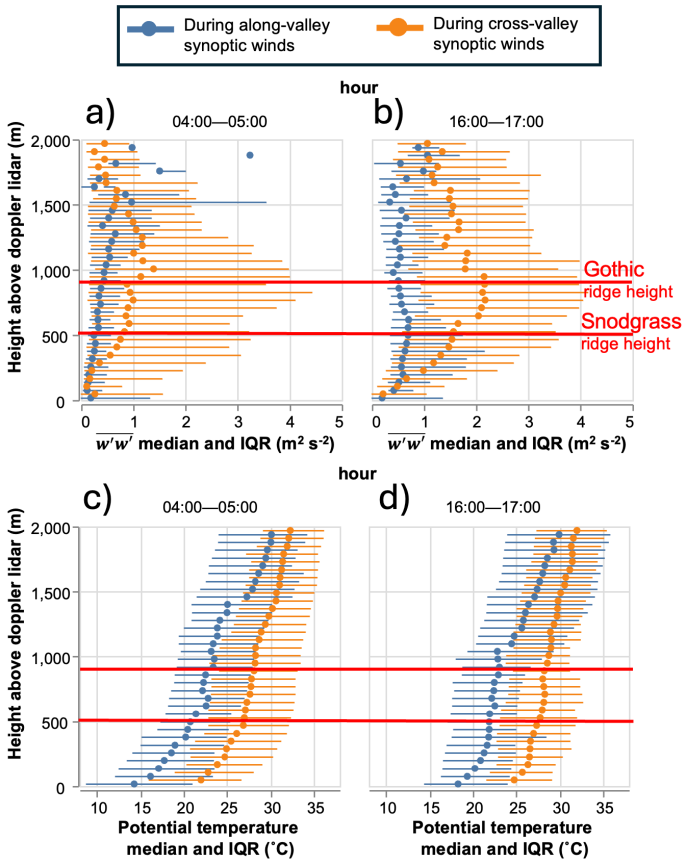

Figure 3.5: (a) Median (circles) and interquartile range (IQR, lines) of $olw'w'$ for bins of height, including data between 04:00–05:00 local time. (b) Same as (a), but including data between 16:00–17:00 local time. (c) Median and interquartile range of potential tempreature measured by rawinsonde for bins of height, including data between 04:30–05:00 local time. (d) Same as (c), but including data between 16:30–17:00 local time.

around the Gothic ridge height (Figure 3.5a and b). Median $\overline{w'w'}$ was larger during the daytime hours ((Figure 3.5b), but the spread was similar across day and night. Below approximately 300 meters, at night, $\overline{w'w'}$ was suppressed to near zero (Figure 3.5a); but it was not during the day (Figure 3.5b). The rawinsonde potential temperature profiles indicate that during the nighttime, there is stronger static stability than during the daytime. At night, there is a positive temperature gradient between 0 and 500 meters AGL (Figure 3.5c); during the day, a positive temperature gradient is mostly restricted to the lowest 200 meters, and the temperature gradient is shallower during cross-valley winds than during along-valley winds (Figure 3.5d).

3.4.2 Case studies

To elaborate on the near-surface and valley-scale turbulence observations, we now present two case studies which exemplify the different turbulence regimes observed during along- and cross-valley winds. We chose one day with cross-valley winds, 18 April 2023, and another with along-valley winds, 9 April 2023. We selected 18 April 2023 because it accounts for the plurality of V_{TKE} outliers at the GOT and AVP sites (Figure 3.2a–d). *Schwat et al.* [2025] found that 18 April had the largest daily sublimation rate of the 2022–23 snow-covered season, and we observed unique turbulent structures in the Doppler lidar scans (presented later). We selected 9 April for comparison with 18 April because the two days had similar temperature regimes, with above-freezing daytime air temperatures and a snowpack with a 0 °C surface (not shown). Additionally, 9 and 18 April had similar, moderate near surface wind speeds (2–6 m/s, Figure 3.6b and d).

Mean winds

On 9 April, slow (2–8 m/s) synoptic (1–1.5 km AGL) winds blew in the along-valley direction, beginning as northwesterly winds and shifting to northerly winds in the evening (Figure 3.6a). Synoptic and within-valley wind directions were the same, except from 14:00–18:00 LT when 0–300 m winds turned westerly. During the night (before 09:00 LT, after 18:00 LT), the

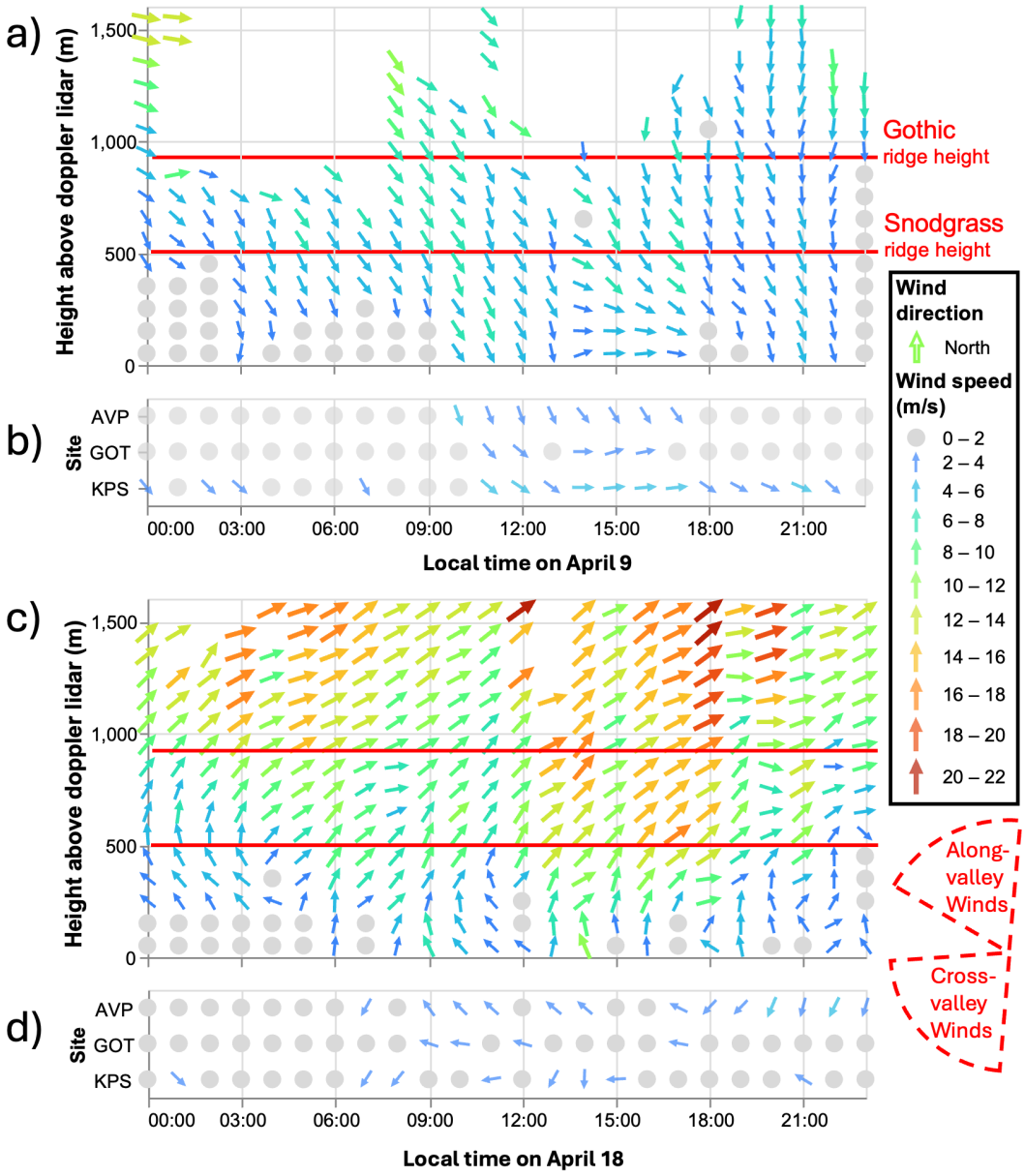

Figure 3.6: Hourly mean valley-scale and near-surface winds on 9 and 18 April 2023. (a) Vertical profiles of wind speed and direction measured by the Doppler lidar above the GOT site on 9 April. Missing data is due to poor lidar returns. (b) Wind speed and direction measured at the three surface measurement sites on 9 April. (c) Same as panel a, on 18 April. (d) Same as panel b, on 18 April. Wind directions during speeds less 2 m/s are not shown.

limited winds above 2 m/s blew down the East River Valley (Figure 3.6b), consistent with the nighttime thermal, downvalley winds common in mountains and observed in the East River Valley [*Adler et al.*, 2025; *Whiteman*, 2000]. During the day (09:00–18:00 LT), AVP experienced consistent downvalley winds, coherent with the synoptic winds; upvalley winds were not observed (Figure 3.6b). This is consistent with the forced channeling, whereby synoptic winds propagate momentum deep into the valley and surface winds mimic synoptic winds [*Adler et al.*, 2025].

On 18 April, fast (10–20 m/s) synoptic winds blew cross-valley, from the southwest (Figure 3.6c). Throughout the day, there was little coherence between synoptic (above Snodgrass) and within-valley (below Snodgrass) winds; winds below 300 meters blew in the upvalley direction. This type of wind behavior could explain the large rotational shear observed during cross-valley winds (Figure 3.4g and h). Surface winds on 18 April were noisy and inconsistent, although upvalley winds were common during the daytime at the AVP site (Figure 3.6c). The GOT site experienced easterly winds.

Near-surface turbulence

We plotted measurements of wind speed and V_{TKE} from the two case study days (Figure 3.7) and found them to match the general turbulence statistics observed for the cross-valley and along-valley categories (Figure 3.2). V_{TKE} was larger on 18 April at all three sites, even though the spread of wind speeds at each site was similar during the two dates. At the AVP and GOT sites, the V_{TKE}-wind speed relationship was non-linear on the 18th, with a scatter of high V_{TKE} values at low wind speeds (Figure 3.7a and b). The V_{TKE}-wind speed relationship at KPS was linear on both days, with a steeper linear relationship on 18 April than 9 April (Figure 3.7c). At the AVP site on both days, anomalously low V_{TKE} values were found at wind speeds less than 2 m/s (Figure 3.7a). At the three sites, turbulence on 9 April is within the local instability (I) or surface shear (II) regimes defined by *Sun et al.* [2012] (Figure 3.7, all panels). On 18 April, turbulence is within the top-down turbulence regime (III).

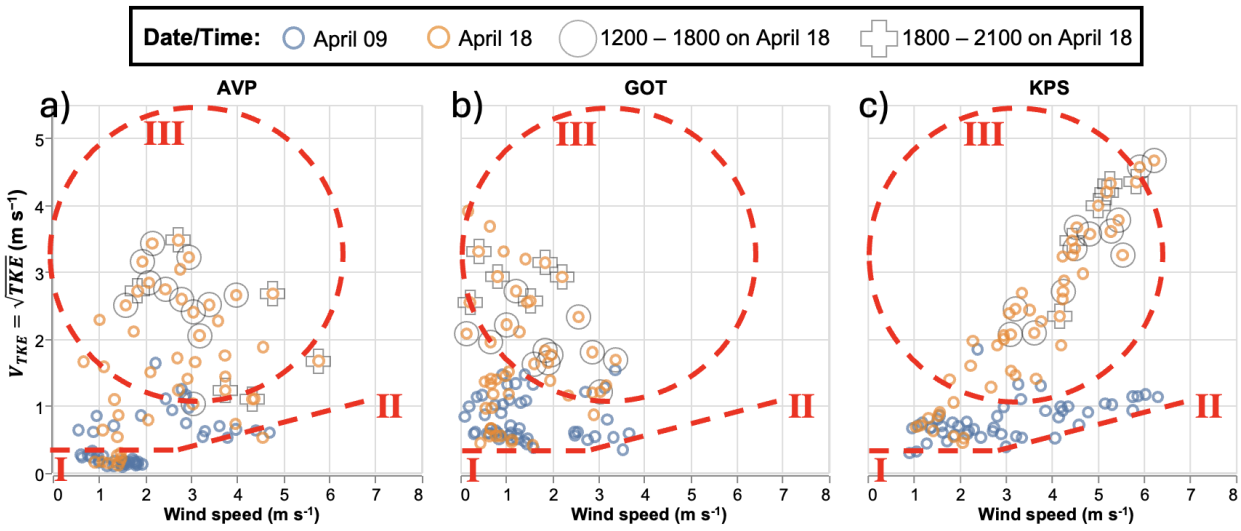

Figure 3.7: V_{TKE} versus wind speed for the three near-surface measurement sites on 9 and 18 April 2023, AVP (a), GOT (b), and KPS (c). Color indicates the case study date. Points underlain by gray circles are from 12:00–18:00 LT on 18 April, underlain by gray crosses from 18:00–21:00 LT on 18 April. The red lines and circle indicate three turbulence regimes, following *Sun et al.* [2012]: Turbulence generated by local instability (I), by shear at the surface (II), and by top-down turbulent events (III).

To further examine near-surface turbulence characteristics on the two case study days, we analyzed individual spectrograms of streamwise momentum flux at the three surface measurement sites. On April 9, at the GOT and KPS sites, negative cospectral power was concentrated at small timescales ($\tau < 100$ seconds, Figure 3.8c, e), and increased in magnitude when near-surface wind speeds increased around 11:00 and again at 14:00 LT (Figure 3.6b). At the AVP site, negative cospectral power was concentrated at larger timescales, and little power was observed at the smallest timescales (Figure 3.8a). At all sites, intermittent bursts of positive cospectral power were observed at the largest timescales ($\tau > 200$ seconds). On 18 April, cospectral power was approximately one order of magnitude larger than on 9 April. At the GOT and KPS sites, cospectral power was predominantly positive and concentrated at larger timescales ($\tau \geq 100$ seconds, Figure 3.8d and f). At AVP, cospectral power was also concentrated at larger timescales, but was not as positive nor consistent as at the other sites Figure 3.8b.

Valley-scale turbulence and shear

On 18 April, we found elevated near-surface turbulent energy (Figure 3.7) and positive momentum fluxes at large scales (Figure 3.8d, f), which suggest that sub-mesoscale to mesoscale structures may be contributing to the increased surface turbulence. To characterize the structure of valley-scale turbulence on April 18, we examined rawinsonde measurements of humidity and potential temperature and time series of vertical profiles of $\overline{w'w'}$, dU/dz, and $dDir/dz$ above the GOT site (Figure 3.9). We also replicate the GOT cospectra (Figure 3.8d) for comparison (Figure 3.9d). At 04:30, a stable inversion existed in the lowest 150 meters of the atmosphere, with potential temperatures increasing approximately 10 K (Figure 3.9a). By 16:30, the atmosphere was almost completely isothermal and neutral, with potential temperature increasing by only 1 degree between the lowest rawinsonde measurement height (approximately 10 m AGL) and 2000 m. Throughout the day, humidity decreased with height, with especially strong gradients near the surface (Figure 3.9a).

Vertical profiles of $\overline{w'w'}$ from the Doppler lidar illustrate times and locations in the

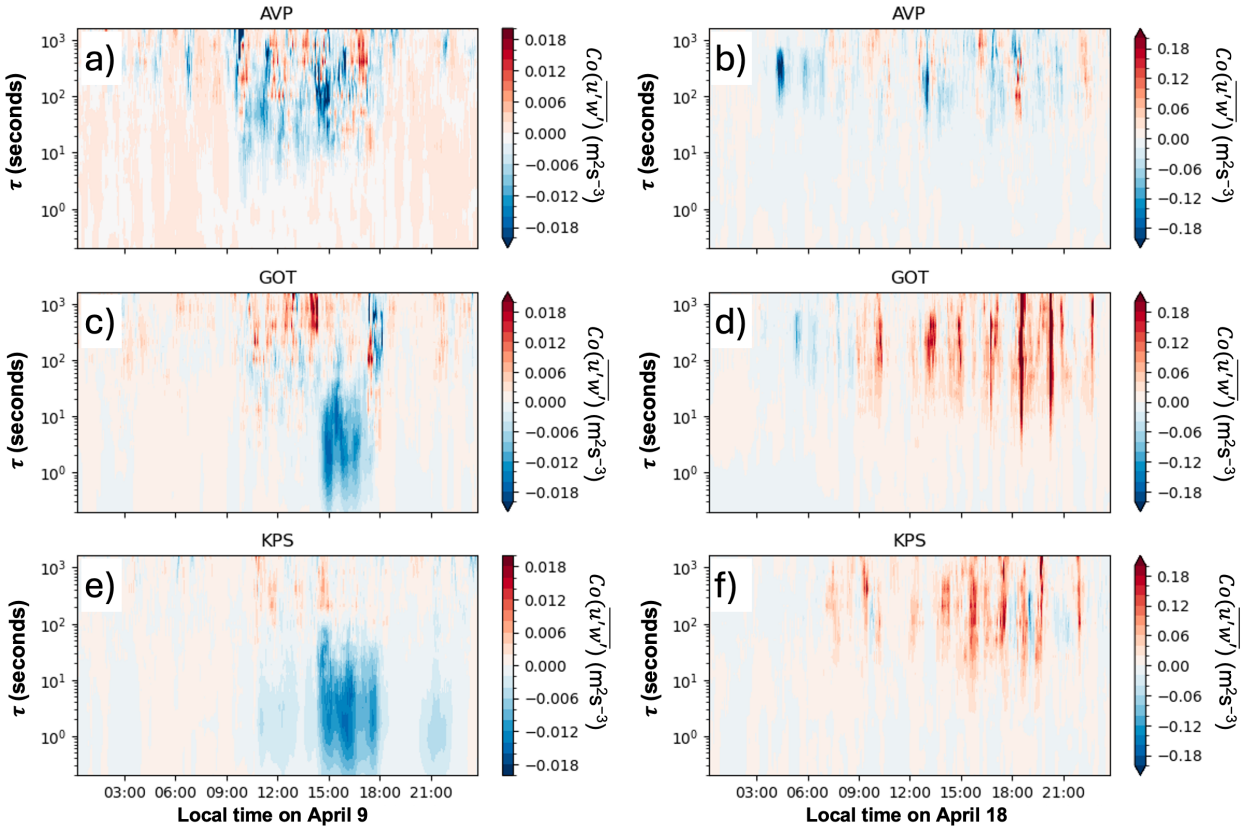

Figure 3.8: Cospectrograms of streamwise momentum flux calculated from three EC measurements at three valley-floor sites. Cospectrograms are shown for April 9 at the (a) AVP, (c) GOT, and (e) KPS sites, and for April 18 at the (b) AVP, (d) GOT, and (f) KPS sites. Cospectrograms are calculated using a sliding window multiresolution decomposition (see Section 3.3.2). For each separate cospectra calculation, data are double-rotated into the streamwise coordinate system. Note that the color bars are different on 9 and 18 April.

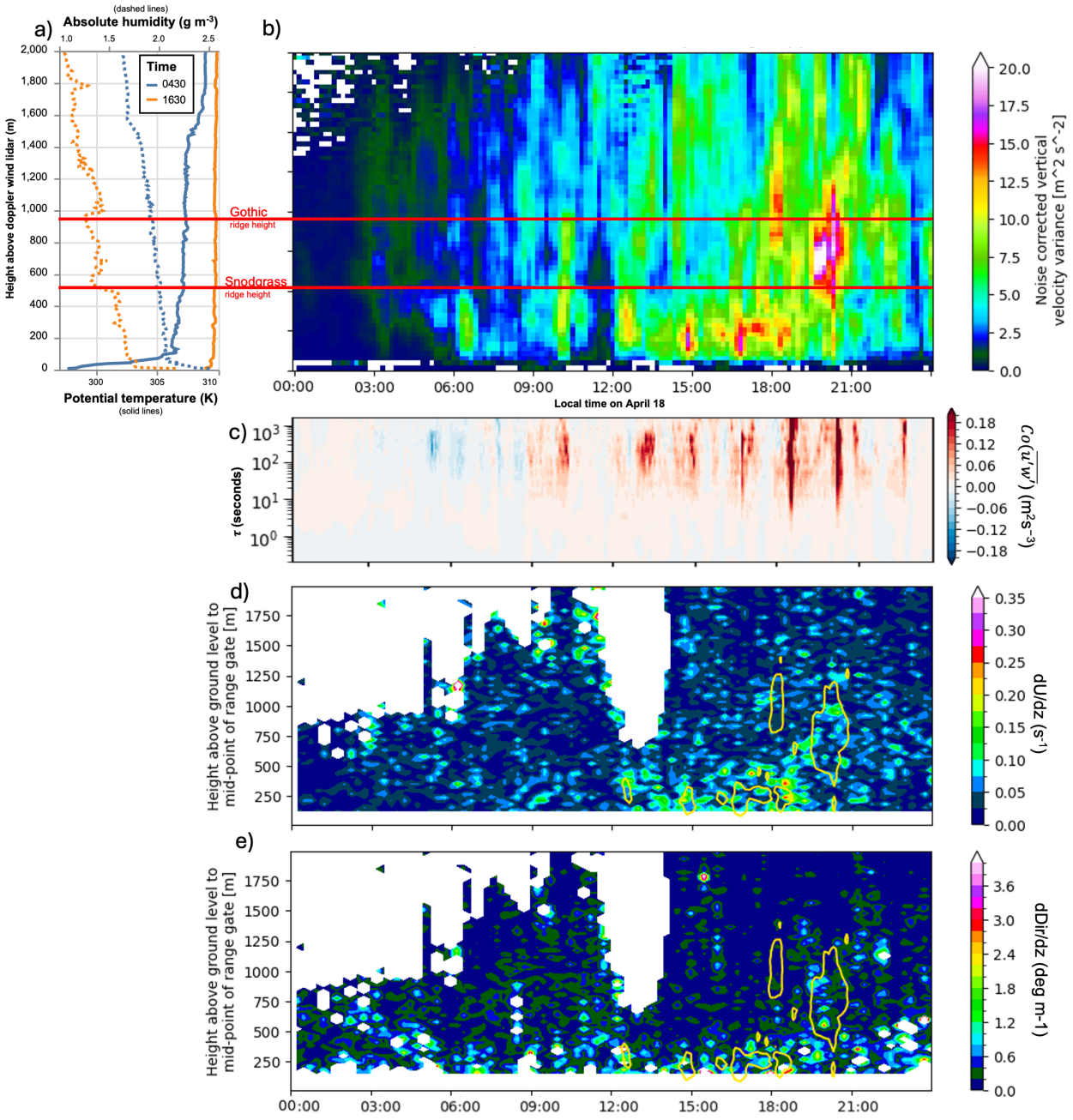

Figure 3.9: *Caption on next page.*

Figure 3.9: (a) Measurements of potential temperature (solid lines) and absolute humidity (dashed lines) from twice-daily rawinsondes on April 18, 2023. (b) Vertical profiles of $\overline{w'w'}$ throughout April 18 from vertically-staring Doppler lidar scans. Measurements are calculated for 10-minute averaging periods. For both panels, red lines indicate the heights of the two tallest features to the windward side of all instrumentation (see Figure 3.1). (c) Cospectrogram of streamwise momentum flux at the GOT site. Recreated from Figure 3.8d for comparison with panel b. (d) Vertical profiles of dU/dz on April 18, measured by doppler lidar PPI scans. Yellow contour lines indicate the time-height locations of $olw'w'$ spikes observed in panel b. (d) Vertical profiles of $dDir/dz$ on April 18, also measured by doppler lidar PPI scans.

valley atmosphere with increased turbulence. $\overline{w'w'}$ began increasing around 12:00 LT, and intermittently spiked between 100–400m throughout the afternoon and early evening (Figure 3.9b). The increase around 12:00 corresponds to an increase in synoptic wind speed (Figure 3.6c) Maximum observed $\overline{w'w'}$ occurred at heights of 500–1000m between 20:00–21:00 LT (Figure 3.9b); this spike was preceded by a spike in synoptic wind speeds around 18:00, which lasted through 20:00 (Figure 3.6c). Spikes in $\overline{w'w'}$ corresponded in time to spikes in positive momentum fluxes observed at the GOT site (Figure 3.9c), and corresponded in time and space to increased shear and rotational shear (Figure 3.9d and e).

We extracted the vertical profiles of $\overline{w'w'}$ and $\overline{w'w'w'}$ between 20:00–21:00 LT 18 April, during which we observed peak $\overline{w'w'}$, and compared them with the seasonal statistics (Figure 3.4b and f). During the 20:00–21:00 LT event, the $\overline{w'w'}$ profile peaked between the Snodgrass and Gothic ridge heights, which matched the average $\overline{w'w'}$ profile during fast, cross-valley synoptic winds; although, the magnitude was about six times larger (Figure 3.4b, black line). Also, a second, smaller peak in $\overline{w'w'}$ appears closer to the surface. During the same hour, $\overline{w'w'w'}$ was positive at and above the Gothic ridge height, and negative below (Figure 3.4f,

black line). This negative $\overline{w'w'w'}$ implies the occurence of downdrafts, and a downward transport of $\overline{w'w'}$ from the ridge-height towards the surface. This profile was somewhat representative of the average $\overline{w'w'w'}$ profile during fast, cross-valley synoptic winds, although the 20:00–21:00 LT April 18 magnitude of negative skewness was much larger than the seasonal average (Figure 3.4f, compare orange dots and black line).

To further characterize the 20:00–21:00 LT turbulent event observed in $\overline{w'w'}$ measurements (Figure 3.9b), we examined four cross-valley RHI scans of the valley wind field between 20:00–21:00 LT (Figure 3.10c–f). To aid in the interpretation of these scans, we also simulated flow over Gothic Mountain (Section 3.3.3), and extracted the 2D velocity field (Figure 3.10a). We simulated a Doppler lidar scan in the modeled 2D velocity field, creating a simulated radial velocity field (Figure 3.10b). The simulated 2D velocity field, simulated Doppler lidar scan, and real scans (Figure 3.10, all panels) illustrate westerly flow above 1250 meters AGL, with negative radial velocities to the left (west) and positive to the right (east) of the Doppler lidar. The simulated 2D velocity field includes a series of vortices forming in the lee of Gothic, as well as return, up-slope flow on the lee-slope of the mountain (Figure 3.10a). Vortices observed in the 2D velocity field (Figure 3.10a) appear as dipoles of positive and negative radial velocities in the simulated Doppler lidar scan (Figure 3.10b). The dipoles rotate as they get closer to directly above the lidar. Two real Doppler lidar scans at 20:15 and 20:18 LT show a series of velocity dipoles in the lee of the peak of Gothic Mountain, as well as return flow, flowing up the lee-side of Gothic (Figure 3.10c and d). Based on our simulated 2D velocity field and radial velocity fields, we interpret the observed dipoles as vortices. In the 20:15 (20:18) scan, we identified 5 (3) distinct vortices forming on Gothic's lee side. The vortices had radii varying between approximately 125–250m. In the 20:45 and 20:48 scans, one large rotor in the lee of Gothic is visible, and this lee-rotor contributes to up-slope flow on the lee side of Gothic, and forms a large shear layer at ridge-height (approximately 1000 meters), where flow reverses direction (Figure 3.10e and f).

During the rotor event observed between 20:00–21:00 LT on 18 April, we examined high resolution (20-Hz) measurements of vertical velocity and humidity at heights between 3 and

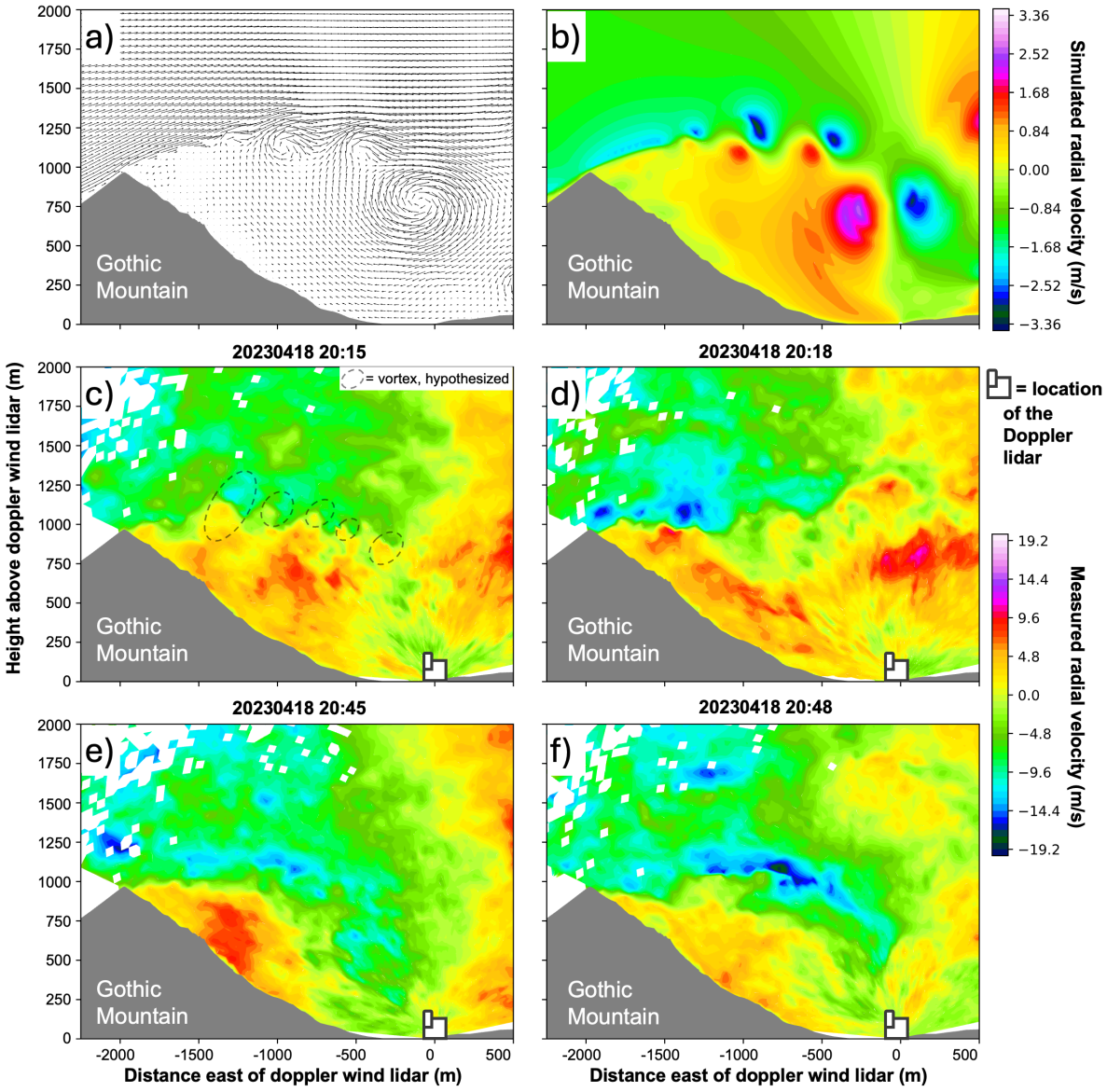

Figure 3.10: (a) Quiver plot illustrating the velocity vector field of simulated flow over Gothic Mountain. 2D flow was simulated over the topographic transect that underlies the actual Doppler lidar RHI scanning axis. (b) Simulated Doppler lidar scan of the 2D velocity field shown in panel a. Radial velocities are extracted from panel a, for comparison with real Doppler lidar scans (panels c–f). Radial velocities measured by real RHI scans at (c) 20:15, (d) 20:18, (e) 20:45, and (f) 20:48 LT on 18 April 2023. Additional scans from April 18 are shown in Figure 3.13. The terrain cross-section corresponds to the lidar scan axis shown in Figures 3.1a, b, and e.

20 meters at the KPS site. We focused on a 6-minute period (20:34–20:40) that illustrates three distinct downdrafts, negative spikes in vertical velocity (outlined with dashed lines, Figure 3.11a). Downdrafts were characterized by large negative spikes in w which were largest at 20 m and decreased in magnitude towards the surface, with the 3 m measurements showing no negative spike. When negative vertical velocity spikes were observed at higher measurements, variance in 3 m w (represented as noise or spread) increased, indicating that downdrafts lead to near-surface spikes in $\overline{w'w'}$. Downdrafts were also associated with a renewal of dry air towards the surface. In between downdrafts, near-surface humidity grew, with humidity closer to the surface increasing more rapidly (Figure 3.11b). Upon the start of a downdraft, humidity values decreased to $\sim$ 1.1 g m^{-3} at all heights, and remained constant until the downdraft ended. This drier humidity corresponds to the humidity of the air far above the valley-floor ($\sim$ 1400 m AGL, Figure 3.9a), although the rawinsonde data was collected four hours earlier.

3.4.3 Model predictions of fluxes

Finally, we examined the predictive power of a bulk aerodynamic parameterization for turbulent fluxes. On 9 April, we found that latent and sensible heat fluxes were modeled well (Mean Error = 0.70 W m^{-2} for latent heat fluxes and 4.4 W m^{-2} for sensible heat fluxes) (Figure 3.12a). But, on April 18, both heat fluxes were underestimated (Mean Error = -21 W m^{-2} for latent heat fluxes and 31 W m^{-2} for sensible heat fluxes) (Figure 3.12b). This was also investigated by *Cox et al.* [in review]. We modeled latent heat fluxes over our full study period (30 November 2022 to 15 June 2023), and compared the model performance during different synoptic winds. On average, during fast, along-valley synoptic winds, model predictions of latent heat fluxes matched measurements (Figure 3.12c). On average, during fast, cross-valley synoptic winds, the model consistently underestimated measured latent heat fluxes $>$ 15 W m^{-2}.

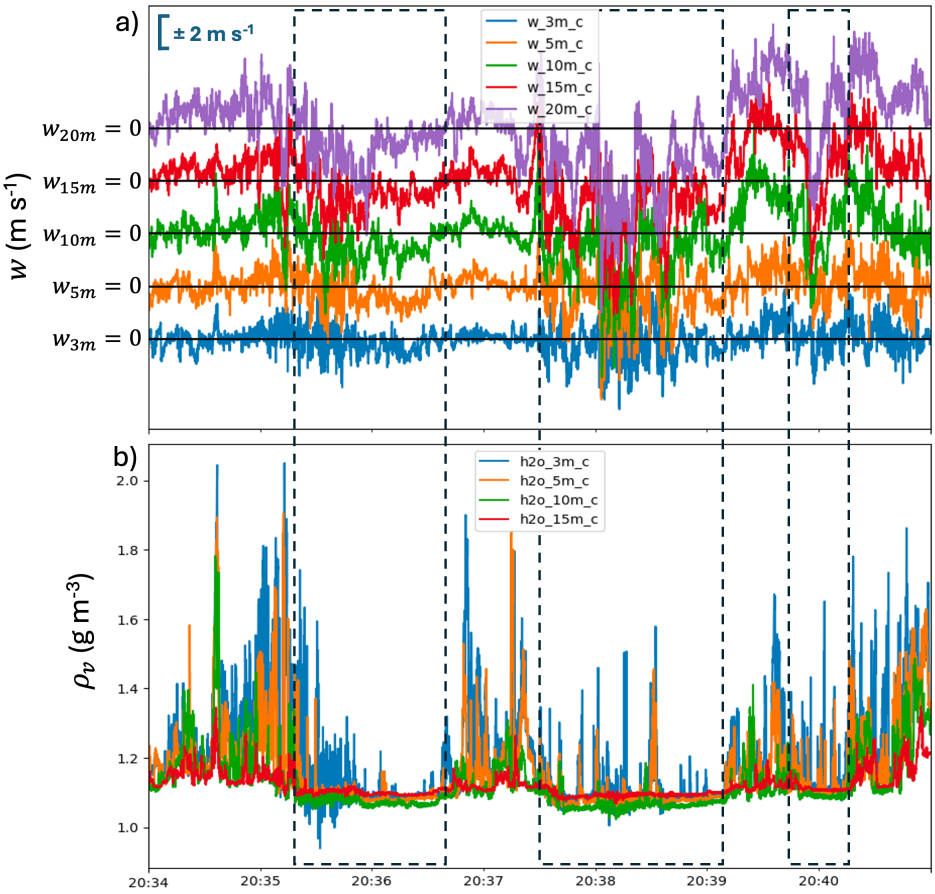

Figure 3.11: (a) 20 Hz measurements of w from five sonic anemometers at various heights. Color and location on the y-axis indicates the measurement height. (b) 20 Hz measurements of ρ_v from five gas analyzers co-located with the sonic anemometers. Color indicates the measurement height. Dashed boxes outline three distinct downdraft events. Gas analyzer measurements were calibrated by removing mean-bias between gas-analyzer and hygrothermometer measurements, taking hygrothermometer measurements as truth. Separate hygrothermometer measurements were available at each height.

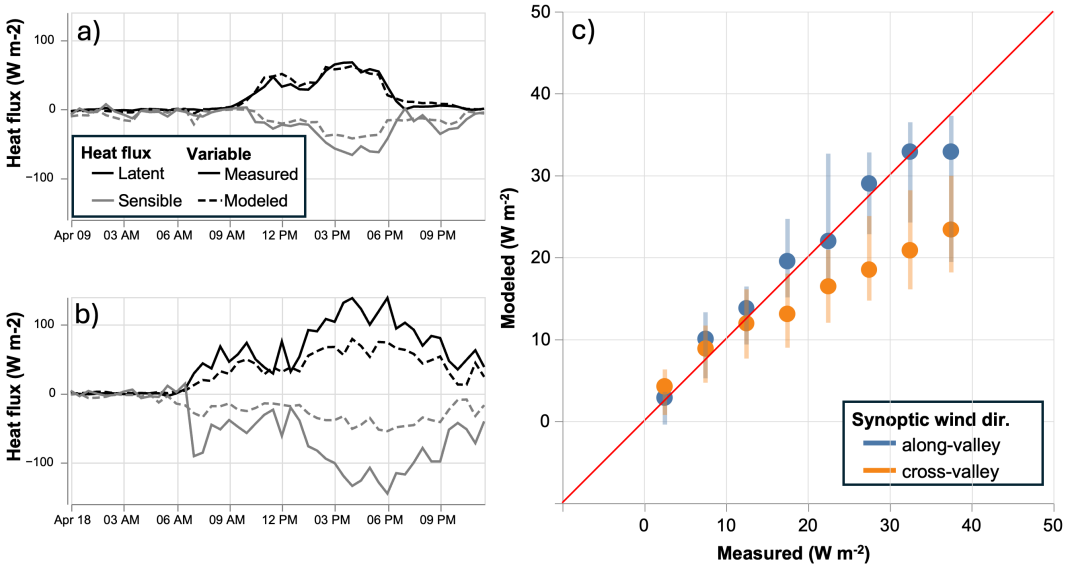

Figure 3.12: Measured and modeled turbulent heat fluxes. (a) Heat fluxes on April 9 2023. Measurements are from the 3-meter EC at the SOS site. Modeled values are following the bulk aerodynamic method described by *Andreas et al.* [2010]. (b) As in a, but on April 18 2023. (c) Mean (circles) and interquartile range (lines) of modeled latent heat fluxes for bins of measured fluxes, including all 30-minute data from our study period, 30 November 2022 to 15 June 2023. Data are categorized by synoptic wind direction. Data is only included during fast ($> 10 m/s$) synoptic winds.

3.5 Discussion

3.5.1 Observations of top-down turbulence near the surface

We examined when and where near-surface turbulence in the upper East River Valley was influenced by top-down processes (Hypothesis I). Near-surface measurements of V_{TKE}, momentum flux cospectra, and 20 Hz wind and humidity data suggest that cross-valley synoptic winds promote top-down turbulence.

During along-valley synoptic flow, near-surface EC measurements of V_{TKE} increased linearly with wind speed and remained below 2 m s^{-1}, on average (Figure 3.2 and Figure 3.7, regime II). This behavior aligns with classical turbulence surface-scaling, in which local shear production dominates the TKE budget (e.g., the law of the wall). In contrast, cross-valley synoptic winds produced elevated V_{TKE} at low wind speeds (Figure 3.2 and Figure 3.7, regime III), consistent with the signature of top-down turbulence described by *Sun et al.* [2012], in which near-surface turbulence intensity decouples from near-surface mean wind speed.

We further distinguished the turbulence regimes using momentum flux cospectra. During along-valley synoptic flow, momentum fluxes were uniformly negative across scales, and of a larger magnitude during the daytime (Figures 3.3a, 3.3c, 3.8c, 3.8e), consistent with the typical surface-scaling approach for predicting turbulence, in which the ground acts as a momentum sink. Turbulence may be suppressed at night due to increased stability at night (Figure 3.5a). During cross-valley synoptic flow, this pattern changed. While small turbulent scales remained dominated by negative fluxes, large scales ($> 10^2$ s) exhibited intermittent positive fluxes (Figure 3.3b). On 18 April, intermittent positive fluxes coincided in time with spikes in turbulence measured far above the surface (Figure 3.9b and c), and we interpreted the large-scale positive fluxes to indicate top-down turbulence. Similar low-frequency peaks in momentum flux cospectra have been reported in other complex terrains, such as the Bolivian Andes, where *Litt et al.* [2015] attributed low-frequency peaks to interactions between coherent terrain-induced structures and surface-layer flow.

We also analyzed 20 Hz near-surface EC vertical velocity and humidity data during a top-down turbulence event (20:30–20:40 LT, 18 April). Short-lived downdrafts (30–60 seconds long; Figure 3.11a) coincided with increased velocity variance and weak humidity variance and a clearly defined lower humidity limit of about 1.1 g m^{-3} (Figure 3.11b). The increased velocity variance suggests that downdrafts carry turbulent energy; the decreased humidity variance suggests that during downdrafts, humidity gradients near the surface go towards zero. Additionally, the mean near-surface humidity during downdrafts was equal to the mean humidity observed several hundred meters above (Figure 3.9a). These observations suggest episodic downward transport of dry air from above the valley floor; although, the rawinsonde observations of humidity aloft were taken four hours prior to the observed downdrafts, so this interpretation remains tentative. Between downdrafts, near-surface humidity increased in ramp-like patterns due to local exchange with the surface [*Cox et al.*, in review]. Our observations of humidity ramps and renewal of dry air to the surface resemble the results of *Litt et al.* [2015], who attributed similar fluctuations in potential temperature to coherent structures interacting with the surface flow.

3.5.2 Top-down turbulence associated with shear-production of turbulence aloft

We also hypothesized that top-down turbulence originates from wind shear near ridge height (Hypothesis II). Doppler lidar measurements of $\overline{w'w'}$, dU/dz, and $dDir/dz$, together with near-surface observations support this interpretation, and also suggest that rotational shear within the valley, below ridge-height, generates turbulence. Observations of $\overline{w'w'w'}$ further indicate that turbulence produced by shear is transported down to the valley floor.

Between 12:00 and 21:00 LT on 18 April, synoptic winds blew in the cross-valley direction and within-valley winds blew upvalley (Figure 3.6c). We observed both wind shear and rotational shear throughout the 18th (Figure 3.9d and e), which coincided in time and space with spikes in $\overline{w'w'}$ (Figure 3.9b). On average during fast cross-valley winds, shear and $\overline{w'w'}$ peaked at the height of the Gothic Ridge (orange dots in Figure 3.4b and d); and rotational shear peaked within the valley, below the height of Snodgrass (orange dots in

Figure 3.4h). These suggest that shear at height of Gothic Ridge and within the valley are producing turbulence. Shear at the Gothic ridge height may be due to flow-blocking. RHI scans revealed that near the height of the Gothic Ridge, flow rapidly reverses direction (e.g. Figure 3.10e). Rotational shear within the valley may due to wind turning. On 18 April, wind direction changed most rapidly with height, turning from up-valley to cross-valley, between 100–400 m AGL (e.g., at 14:00 LT, Figure 3.6c). Averaged over the study period, rotational shear peaked below 400 m during cross-valley winds (Figure 3.4g–h), suggesting that this wind-turning feature persists throughout the season. Previous authors have also suggested that wind-turning increases near surface turbulent exchange [*Rotach et al.*, 2008].

Between 18:00 and 21:00 LT on 18 April, $\overline{w'w'w'}$ was negative below 900 m (black line, Figure 3.4d). Because $\overline{w'w'w'}$ represents the vertical turbulent transport of $\overline{w'w'}$, negative values indicate downward diffusion of turbulent kinetic energy (TKE) [*Stull*, 1988, p. 152]. Following downdraft events observed near the surface, variance in 3 m w increased, supporting the interpretation that downdrafts transported TKE towards the surface (Figure 3.11a). Together, these multi-scale observations suggest that TKE within the valley is transported downward, from shear layers to the surface, consistent with a "top-down" boundary layer structure. Our interpretations of TKE transport are supported by *Turnipseed et al.* [2004], who also linked negative $\overline{w'w'w'}$ to intermittent downdrafts in complex terrain; and by *Litt et al.* [2017], who found that vertical TKE transport in complex terrain is non-negligible and can influence near-surface turbulence.

3.5.3 Stability effects on the valley turbulence structure

Our interpretation that peak $\overline{w'w'}$ high above the valley floor is the result of shear-generated turbulence is supported by the observed spikes in $\overline{w'w'}$, dU/dz, and $dDir/dz$ that coincided in time and space (Figures 3.4 and 3.9b–e). This interpretation also relies on the assumption that no other processes could have generated turbulence, although we have thus far ignored the possibility of buoyancy-generated turbulence. In this section, we examine how buoyancy could have contributed to the turbulence signals observed aloft.

Our study period (30 November 2022–10 May 2023) spanned the period with extensive snow cover in the East River Valley [*Schwat et al.*, 2025; *Lundquist et al.*, 2024; *Lapo et al.*, 2019], and unstable conditions were exceedingly rare. We estimated near-surface static stability using the 3 m and 20 m potential temperatures measured at KPS ($\Delta\theta/\Delta z$). Over the study period, 37% of 30-minute periods were classified as stable ($\Delta\theta/\Delta z \geq 0.05$ K m^{-1}), 61% as neutral ($\Delta\theta/\Delta z < 0.05$), and 2% as unstable ($\Delta\theta/\Delta z \leq -0.05$). Additionally, seasonally-averaged potential temperature profiles show stable conditions during both day and night in the boundary layer above the GOT site (Figure 3.5c and d). The absence of unstable conditions indicates that buoyancy was not a source of TKE production in the East River valley during our study period, and further supports our hypothesis that shear-production of turbulence can dominate the valley atmosphere during the snow season.

In our comparison of the nighttime and daytime boundary layers, we found that $\overline{w'w'}$ always peaked near ridge-height; however, in the lowest 300 meters, $\overline{w'w'}$ was suppressed at night relative to day (Figure 3.5a and b). This could be due to the stable stratification of the atmosphere — at night, the stable boundary layer was deeper and more strongly stratified (Figure 3.5c and d). This suggests that while shear production of turbulence can still occur during nighttime, downward transport of TKE may have a more limited effect on the surface flow, as buoyant destruction of turbulence near the surface is more efficient at night. However, during extreme cases such as 18 April, TKE produced by shear layers may still reach the surface, as exhibited by the high TKE (Figure 3.7) and spikes in momentum fluxes at large scales (Figure 3.8) observed on the 18th during day and night.

Our study period excluded times without snow cover, when daytime heating of the surface can initiate convection. The summertime structure of boundary layer turbulence in complex terrain may be more complicated than the boundary layer studied here, as both buoyant-production and shear-production could contribute to the TKE budget. We hypothesize that convection could potentially diminish the influence of top-down effects on the surface. Future studies should quantify the importance of top-down turbulence in complex terrain during unstable daytime conditions.

3.5.4 Spatial variation in top-down turbulence

We found that the strength of top-down turbulence varied across valley-floor sites, which likely reflects differences in local terrain geometry and stability. At the AVP site, momentum flux cospectra showed limited small-scale energy on 9 April and weak large-scale positive fluxes on 18 April (Figures 3.8a, b). Small scale turbulence may have been suppressed by the frequent formation of a cold pool (i.e. highly stable conditions) at AVP [*Adler et al.*, 2025, and John Cramblitt, personal communication, 3 September 2025]. Cold pools formed at AVP more than at the other sites because AVP is close to the East River at the valley bottom, while the other sites are perched above the valley bottom (Figure 3.1b). The AVP site's relatively narrow valley setting (Figure 3.1b) may also obstruct large eddies transported downward from aloft. The observed spatial variability in top-down turbulence implies that the importance of top-down effects depends not only on shear strength aloft, but also on near-surface stability and local terrain. However, our measurements of winds and turbulence in the valley were restricted to the airspace above GOT, where the single Doppler lidar was deployed, and it is likely that shear-generation aloft varies horizontally. Future studies should consider deploying multiple lidars at multiple surface sites to understand how valley-scale turbulence varies along with near-surface turbulence.

3.5.5 Formation of rotors and top-down turbulence

Our results supported Hypothesis II, that shear at ridge height drives top-down turbulence, and built on the hypothesis, by implicating shear and rotational shear within the valley as a driver of top-down turbulence. Our observations further illustrate an association between top-down turbulence and the formation of rotors, which we observed with repeated Doppler lidar RHI scans. Here, we discuss the mechanisms responsible for lee-rotor formation, and highlight parallels between top-down turbulence in complex terrain and in the nocturnal stable boundary layer over flat terrain.

Between 20:00–21:00 LT on 18 April, during a period of ridge-height shear and enhanced

top-down turbulence (Section 3.5.2), RHI scans captured two distinct flow patterns in the lee of Gothic Mountain: a series of smaller sub-rotor vortices (20:15–20:18 LT; Figure 3.10c,d) and a single, larger lee rotor (20:45–20:48 LT; Figure 3.10e,f). Our interpretation of the flow including sub-rotor vortices is supported by our 2D flow simulations, which illustrate the radial velocities a Doppler lidar would observe over a series of vortices (Figure 3.10b). During the rotor event, $\overline{w'w'}$ peaked at 16 m^2/s^2 (Figure 3.4b), consistent with previous observations in rotors in southeast Wyoming, USA [*Strauss et al.*, 2015, also measured $\overline{w'w'} = 16$ m^2/s^2].

While the two scans showing the single lee rotor (20:45 and 20:48) illustrate stationary flow with little variability between time steps, the two scans showing sub-rotor vortices propagating downwind (20:15 and 20:18 LT) illustrate a non-stationary flow that has large variability between time steps. These flow structures may correspond, respectively, to type I rotors, stationary rotors that form beneath the crests of non-breaking lee waves, and type II rotors, non-stationary rotors that form within flows resembling hydraulic jumps [*Hertenstein and Kuettner*, 2005]. While previous work has linked type II rotors to top-down turbulence [*Vosper et al.*, 2018], we found evidence of top-down turbulence throughout 18 April and did not identify its association with one type of flow structure over the other. We examined all RHI scans between 12:00–21:00 LT on 18 April (Figure 3.13) and found that single lee-rotor structures (e.g. Figure 3.13, 15:15, 17:48, and others) recurred throughout the day. Sub-rotor vortices appeared less frequently (e.g Figure 3.13, 17:48), although we found that identifying sub-rotor vortices visually is difficult, and they appeared most prominently in the selected scans (Figure 3.10c and d).

RHI scans (Figures 3.10 and 3.13) showed intermittent transitions between single lee-rotor and sub-rotor states, which likely results from instabilities in the ridge-height shear layer. When a stationary, type I lee-rotor forms, an unstable vorticity sheet forms along the horizontal plane where velocity reverses direction (e.g. at ridge-height, ∼900m, Figure 3.10e). Due to Kelvin-Helmholtz instabilities along the vorticity sheet, the lee-rotor may break into smaller sub-rotor vortices [*Doyle and Durran*, 2007; *Doyle et al.*, 2009]. We may observe this process between 20:00–21:00 on 18 April (Figure 3.10c–f), although this

interpretation remains tentative. Overall, our observations suggest that ridge-height shear, itself a source of turbulence, can produce Kelvin-Helmholtz instabilities, which may also generate turbulence and result in top-down effects. These processes highlight similarities between top-down turbulence in complex terrain and in the nocturnal stable boundary layer over flat terrain. In the latter environment, [*Sun et al.*, 2012] attributed top-down turbulence to Kelvin-Helmholtz instabilities in gravity waves.

3.5.6 Predicting surface fluxes in complex terrain

We hypothesized that surface fluxes would be underestimated by MOST during periods of top-down turbulence (Hypothesis III). To test this, we compared estimates of surface fluxes from EC measurements and a bulk aerodynamic approach (Section 3.3.4). Below, we discuss model performance during top-down turbulence and how downdrafts may influence near-surface fluxes.

During strong cross-valley synoptic winds, when top-down turbulence was most evident (Section 3.5.1), the bulk approach underestimated EC measurements. *Cox et al.* [in review] proposed that bulk aerodynamic methods failed on 18 April because the shallow ($\sim$ 20 cm) stable layer above the snow surface intermittently decoupled from the atmosphere above, violating MOST's assumption of steady, continuous turbulence. Our observations in this study suggest that other assumptions underpinning MOST are additionally violated. Namely, MOST assumes that the near-surface turbulent kinetic energy (TKE) budget is dominated by local shear and stability, whereas during top-down turbulence, near-surface TKE also dependes on TKE transported downward from elevated shear layers [*Litt et al.*, 2017, also see our Section 3.5.2]. On 18 April, we observed downdrafts that coincided with increased near-surface velocity variance (Figure 3.11a) and reduced near-surface humidity (Figure 3.11b), implying that advection or turbulent diffusion of TKE and dry air from aloft may be responsible for increased surface latent heat fluxes relative to MOST predictions. In a similar vein, *Schwat et al.* [2025] detected downward advection of dry air at the KPS site, although their estimates of vertical advection represented transport across near-surface ($<$ 20 m) humidity

gradients. Our observations indicate that downdrafts originate from > 100 m above the surface. Therefore, accurate flux estimates under top-down turbulence may need to account for non-local transport processes — whereby persistent eddies carry air parcels with distinct temperature and humidity across large distances, such as from ridge-height to the valley floor. *Soares et al.* [2004] parameterized non-local transport for a different scenario, when convective plumes originate at and rise above a warm earth surface. Their work may offer a blueprint for parameterizations surface exchange during top-down turbulence.

3.6 Conclusions

Turbulence in complex terrain remains difficult to represent, and research has shown that conventional modeling approaches often struggle to reproduce fluxes in the mountain boundary layer. Part of this challenge stems from the presence of well-known terrain-driven flows, such as thermal winds, lee-rotors, and mountain waves, that fall outside the assumptions of Monin–Obukhov Similarity Theory (MOST) and therefore evade standard parameterizations. In 2021–2023, in the East River Valley, an extensive suite of coordinated measurements were collected, creating a natural laboratory for identifying key exchange processes and evaluating turbulence representations in models.

We observed top-down turbulence on the valley floor, and interactions between synoptic winds and topography that generated shear and turbulence in the valley atmosphere. During cross-valley synoptic winds, near-surface flow was characterized by high turbulent energy and low wind speeds, turbulent cospectral spikes in the meso-scales, and repeated downdrafts that increased near-surface velocity variance and decreased near-surface humidity variance. With cross-valley flow, we observed increased shear at ridge-height and in the lowest 400 meters of the boundary layer, associated with wind blocking in the lee of a prominent ridge and wind-turning from valley-bottom along-valley flow to above-valley cross-valley flow. Increased shear was associated with increased $\overline{w'w'}$, which we interpreted as representing increased turbulent kinetic energy (TKE). When $\overline{w'w'}$ spiked in the valley atmosphere at the height of observed shear layers, $\overline{w'w'w'}$ was negative between the shear layers and the surface,

indicating that $\overline{w'w'}$ (and, possibly, TKE) was transported down from the shear layer towards the surface.

We restricted our study period to the snow-covered season, when the boundary layer was mostly stable or neutral (98% of the time); and we found increased $\overline{w'w'}$ at ridge height during both day and night, indicating that buoyancy did not contribute to the high $\overline{w'w'}$. Over six months of observations during snow-cover, we found that top-down turbulence is most common during fast (> 10 m/s), cross-valley synoptic winds, but also occurs during slower cross-valley synoptic flow, and limited top-down effects may occur with along-valley flow. The along-valley/cross-valley distinction was useful for distinguishing turbulence regimes at our site, but the topography around a specific site likely determines how top-down effects vary in time and space. On most days, near-surface turbulence was influenced by both shear at the surface and top-down turbulence. However, during extreme events such as 18 April 2023, near-surface turbulence cospectral power was concentrated in the meso-scales, indicating that the near-surface flow was more influenced by top-down effects than near-surface shear. On 18 April, we observed the intermittent formation of a large lee-rotor and multiple sub-rotor vortices within the mountain boundary layer. These ridge-height, highly turbulent flows appear to influence the entire mountain boundary layer, although they do not appear to be a prerequisite for top-down turbulence.

Our findings suggest that near-surface turbulence is influenced by turbulence generated well above the surface layer and transported downward [*LeMone et al.*, 2019]. This challenges the assumption underlying MOST that the surface-layer TKE budget is governed solely by local shear and buoyancy. In snow-covered complex terrain, where strong shear layers form aloft, downward transport may contribute substantially to near-surface TKE, although future studies should attempt to quantify the TKE budget to confirm this hypothesis. On 18 April, as well as on average during fast cross-valley synoptic winds, surface turbulent heat fluxes were under predicted by the commonly used bulk aerodynamic model. Our results indicate that surface-scaling methods are necessarily low-biased in their predictions of surface-atmosphere exchange during top-down turbulence, and sublimation rates can be

underestimated as a result.

Future studies should examine the potential importance of top-down effects on near-surface turbulence during unstable conditions. Additionally, the frequency and spatial distribution of shear layers produced within complex terrain may need to be understood to implement improved surface flux parameterizations. Future attempts to parameterize surface fluxes in complex terrain should consider the model of non-local transport. The Eddy-Diffusivity/Mass-Flux model formulated to predict fluxes during the formation of convective plumes [*Soares et al.*, 2004] could potentially be "turned upside down" and used to predict surface fluxes in the presence of top-down turbulence. A "brute force" statistical parameterization may also be possible, wherein observed turbulence statistics for a given location, such as those presented here, could be used to bias-correct existing surface flux parameterizations. The skill of such an approach would need to be tested with out-of-sample data, such as from another field campaign. Regardless, the need for a revised parameterization for surface-atmosphere exchange is clear.

Representations of surface-atmosphere exchange in complex terrain play a central role in predicting sublimation as well as surface heat fluxes, which influence snow melt. Therefore, improving surface flux parameterizations means improving our predictions of the timing and amount of streamflow. The atmospheric phenomena examined in this study, including cross- and along-valley flows, flow separation, rotor formation, and shear-layer development, are pervasive in mountainous regions, even if their precise manifestations differ among watersheds. Consequently, the top-down turbulence documented here should be expected in complex terrain more generally. The comprehensive observational record from the East River Valley demonstrates that incorporating such effects is tractable using information on topography and synoptic flow, providing a foundation for the development of turbulence schemes applicable across a wide range of complex terrain settings.

Acknowledgments

We would like to thank Elie Bou-Zeid, Michelle DiBenedetto, Alex Horner-Devine, Dale Durran, Daniel Kirshbaum, and Edwin Rainville for discussions that deepened our understanding and led to this publication. We also thank the Rocky Mountain Biological Laboratory, for their facilitation of the field site, and billy barr, for his detailed logs of weather conditions in the East River valley. This work was supported by National Science Foundation Awards 2139836 and 2139809 and U.S. Department of Energy Atmospheric Systems Research awards DE-SC0024082 and DE-SC0024266. This material is based upon work supported by the NSF National Center for Atmospheric Research, which is a major facility sponsored by the U.S. National Science Foundation under Cooperative Agreement No. 1852977.

Data availability

All data used in this study is available for download. Eddy covariance and surface meteorological measurements at the KPS site were collected as part of the Sublimation of Snow (SOS) campaign [*Lundquist et al.*, 2024] and can be downloaded at the DOI link in this citation: *NSF NCAR/EOL ISFS Team* [2024]. Eddy covariance and surface meteorological measurements at the AVP site were collected as part of the Study of Precipitation, the Lower Atmosphere and Surface for Hydrometeorology (SPLASH) [*Boer et al.*, 2023] and can be downloaded at the DOI link in this citation: *Cox et al.* [2025a]. Eddy covariance measurements collected at the GOT site, rawinsonde measurements, Doppler lidar mean wind measurements, Doppler lidar vertical velocity statistics, and Doppler lidar RHI scans were collected as part of the Surface Atmosphere Integrated Field Laboratory (SAIL) Campaign [*Feldman et al.*, 2023] and can be downloaded at the DOI links in these citations: *Sullivan et al.* [1997b]; *Shippert et al.* [2010, 2022]; *Newsom et al.* [2011]; *Keeler et al.* [2022b].

3.7 Appendix A: Doppler lidar RHI scans on 18 April 2023

In addition to the RHI scans presented in the main body of this study (Figure 3.10), we also included additional RHI scans collected on 18 April 2023 (Figure 3.13). As discussed above, these scans also demonstrate the formation of lee rotors and sub-rotors in the lee of Gothic Mountain.

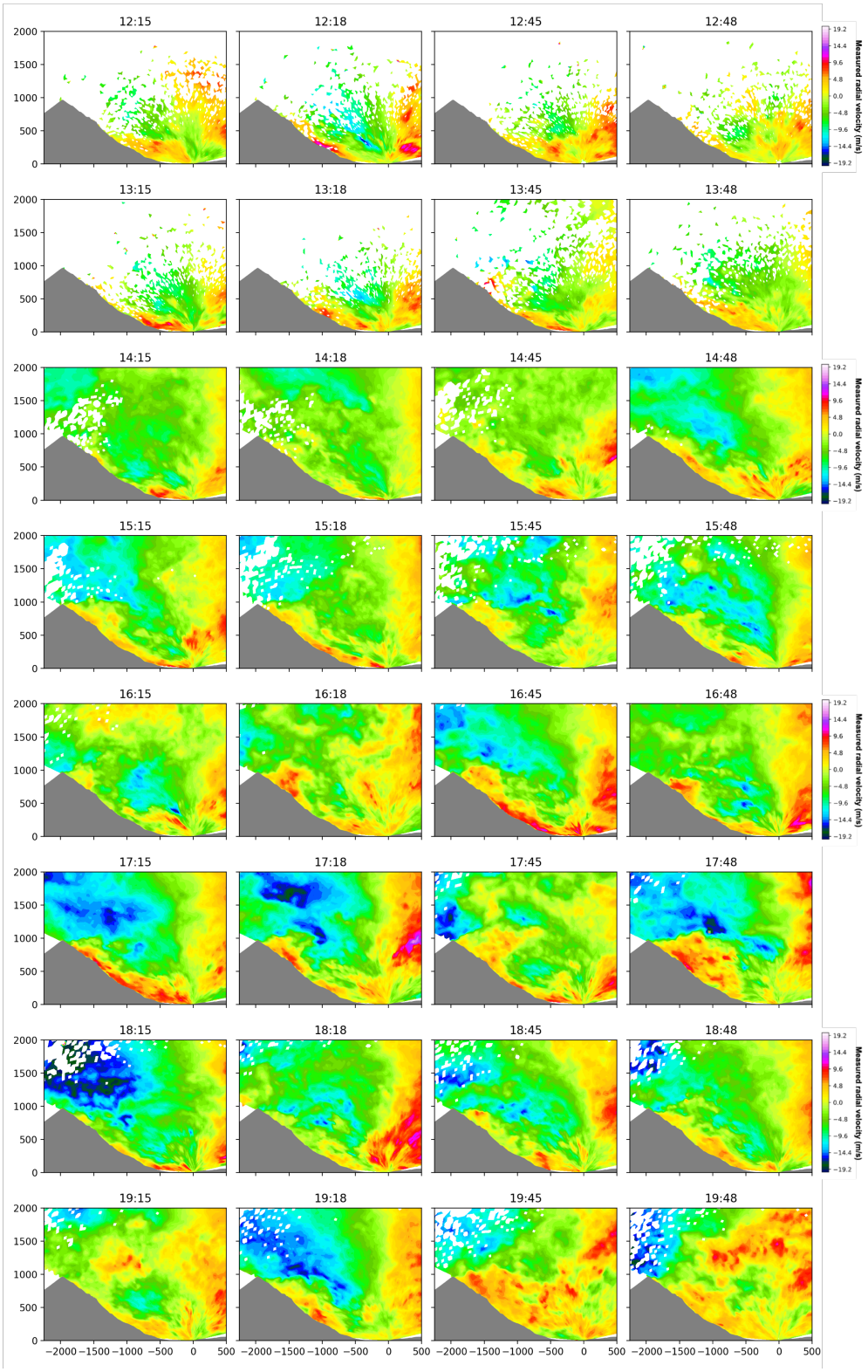

Figure 3.13: *Caption on next page.*

Figure 3.13: Radial velocities measured by all cross-valley RHI scans performed on 18 April 2023, between 12:00 and 20:00 LT. Data points with signal-to-noise less than 0.008 are removed, following *Newsom and Krishnamurthy* [2022].

Chapter 4

MEASURING SENSIBLE HEAT ADVECTION OVER PATCHY, MELTING SNOW: BEYOND POINT MEASUREMENTS

4.1 Introduction

In the atmospheric boundary layer over a horizontally heterogeneous surface, horizontal sensible and latent heat advection can impact surface and near-surface conditions, despite the common assumption that vertical transport processes dominate. Horizontal heat advection has been identified on the coast [*Mahrt et al.*, 2021], at forest boundaries [*Kochendorfer and Paw U*, 2011], within forest canopies [*Thomas*, 2011], and over patchy snow cover with and without vegetation [*Harder et al.*, 2017; *Granger et al.*, 2006; *Mott et al.*, 2018; *Mahrt and Vickers*, 2005]. Heat advection over patchy snow is of particular interest, as the process can control snow melt rates and timing, which can influence the timing of spring streamflow in snow-dominated watersheds. Sensible heat advection over patchy snow has been estimated using numerical atmospheric boundary layer simulations [*Weisman*, 1977; *Liston*, 1995; *Claussen*, 1991] and using measurements from horizontally distributed instrument towers [*Harder et al.*, 2017; *Granger et al.*, 2006; *Essery et al.*, 2006; *Mott et al.*, 2013, 2017]. Based on measurements, bulk theories have been developed to predict the sensible heat advection over snow patches [*Granger et al.*, 2002, 2006; *Essery et al.*, 2006]. These theories have been evaluated with a variety of measurements, including distributed instrument towers and multiple measurements of snow melt distributed across individual snow patches [*Van Der Valk et al.*, 2022; *Mott et al.*, 2011]. Recently, bulk theories have been coupled with one-dimensional snowpack energy balance models [*Harder et al.*, 2019].

Although many studies of patchy snow have highlighted how sensible heat advection en-

hances surface-atmosphere sensible heat exchange, the influence of advection on the surface energy balance and actual snow melt rates remains uncertain. *Mott et al.* [2015] found that sensible heat advection may be important during low fractional snow-covered area (fSCA), because upward heat fluxes over bare ground warm the atmosphere, which enhances advective melting of snow. During higher fSCA, they found that large snow patches on slopes can develop very stable internal boundary layers and thermal drainage flows, which cool surrounding bare ground. In another study, *Mott et al.* [2013] found that stable internal boundary layers above snow patches may decouple from the overlying atmosphere entirely, limiting the effects of advection. This decoupling effect may be especially strong over topographic concavities, where snow patches frequently persist due to preferential deposition during blowing snow transport [*Mott et al.*, 2016; *Fujita et al.*, 2010]. *Harder et al.* [2019] found that including sensible heat advection in a snowmelt simulation resulted in only small differences in the snowpack disappearance date.

A major challenge to measuring sensible heat advection and constraining its influence on the snowpack energy balance is the fact that a large number of scalar and flux fields are relevant to the process. Horizontally and vertically varying temperature fields across snow patch boundaries should be measured to identify the magnitude of horizontal sensible heat advection in the atmospheric surface layer. Eddy covariance measurements of heat and momentum fluxes and wind speeds are required to parameterize bulk models of advection. Radiation measurements and spatially distributed snow melt estimates are required to characterize the snow patch energy balance. To the author's present knowledge, only one study has included all the measurements described above [*Mott et al.*, 2017].

During the 2022-2023 winter in the upper East River Valley of Colorado, Rocky Mountains, USA, we deployed a suite of instruments as part of the Sublimation of Snow campaign [*Lundquist et al.*, 2024]. During a period of patchy snow in the spring melt season, we utilized high resolution satellite imagery to characterize fSCA, an infrared video camera and polyester sheet to estimate sensible heat advection, a scanning lidar and fluidless snow pillows to estimate snow melt rates, and eddy covariance (EC) instruments and radiometers to

characterize the snowpack surface energy balance. We used these measurements to answer the following research questions:

1. What is the magnitude of sensible heat advection?

2. What is the contribution of sensible heat advection to snow melt during patchy snow?

In the following, we first present our study site and our instrumentation. Then, we describe our methods, including how we estimated sensible heat advection over an isolated snow patch with an infrared video camera, how we estimated snow melt rates and the surface energy balance over patchy snow, and how we estimated sensible heat advection over a 300x300 m^2 area around our site. We attempted to estimate sensible heat advection over a larger area because it is the distributed behavior that influences the atmosphere and water resources. After the methods, we present our results and discuss how our observations compare with those from previous studies.

4.2 Study site and instrumentation

We deployed flux towers, scanning lidars, an infrared (IR) video camera, and a polyester sheet to the Kettle Ponds site in the upper East River Valley, Rocky Mountains, USA [*Lundquist et al.*, 2024, the Sublimation of Snow campaign] between October 2022 and June 2023 (Figure 4.1). Four instrument towers at the site had multiple eddy covariance (EC) systems and thermohygrometers mounted between 1 and 20 meters, a four-stream radiometer mounted at 9 meters, four infrared radiometers for measuring surface temperature mounted at 3 meters, and 6 scanning lidars mounted at 9.5 meters, angled towards the ground. In this study, we used measurements from a single EC mounted on tower C at 3 meters above ground level (AGL), and only two of the lidars. The scanning footprints of the two lidars used in this study are shown in Figure 4.1c. A full description of the instruments deployed and the EC data processing are provided by *Lundquist et al.* [2024] and *Schwat et al.* [2025], respectively.

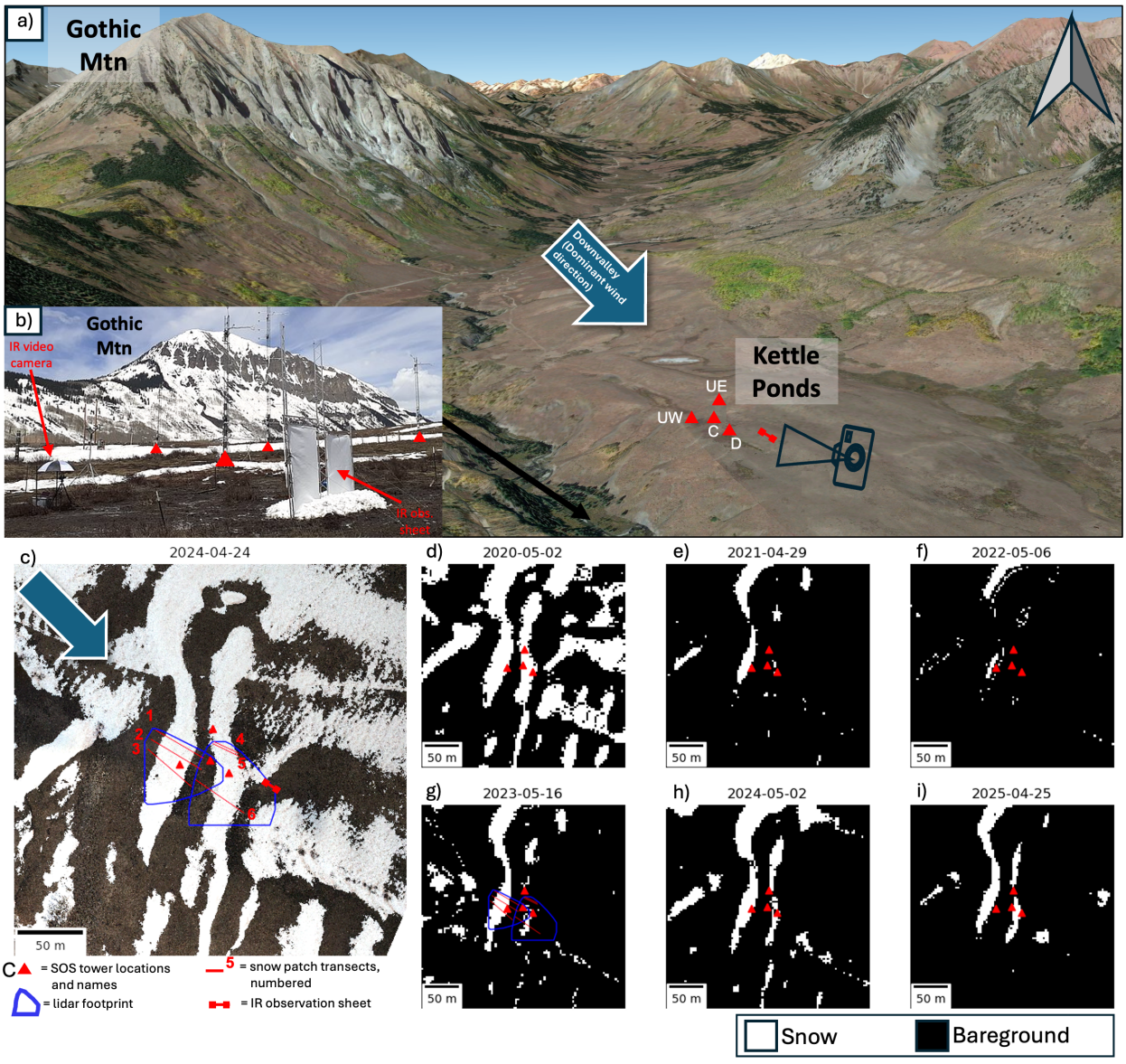

Figure 4.1: *Caption on next page.*

Figure 4.1: a) Google Earth oblique rendering of the upper East River Valley, looking upvalley, and location of the Kettle Ponds site and the four towers deployed there. The camera symbol and cone indicate the viewing angle of the photograph in panel b. b) Camera image of the infrared (IR) video camera and polyester IR observation sheet. c) Orthoimage, collected by unmanned aerial vehicle on 24 April 2024. Red triangles indicate the tower locations. Blue lines indicate the footprints of scanning lidars mounted on tower UE and C (Figure 4.1a). Red lines indicate six transects over which we extracted lidar data. The red line with square-ends indicates the location of the IR observation sheet. d–i) Fractional snow covered area (fSCA) maps derived from 3-meter resolution Planet imagery [*PBC*, 2020/2025; *Yang et al.*, 2023; *Chiu et al.*, 2025]. fSCA maps are shown on six separate years; days were selected to illustrate the consistency of snow patches at the site. Includes copyrighted material of Planet Labs PBC. All rights reserved.

The Kettle Ponds site is on the relatively flat valley bottom of the upper East River Valley, and micro-topography at the site is characterized by 2.5 meter tall ridges and swales (Figure 4.1a). Each year during the snow melt season, snow becomes patchy. During the spring snow melt of 2023, scanning lidars observed the melt out of two distinct snow patches that formed underneath the instrument towers (Figure 4.1g). The distribution of snow during melt season at Kettle Ponds is consistent across years (Figure 4.1d–i), a well-known phenomenon [*Pflug and Lundquist*, 2020; *Schirmer et al.*, 2011]. Hourly camera images, taken facing upvalley from tower D, indicate that in 2023, the first bare ground emerged on 7 May, and snow was completely gone from the site by 26 May. In this study, we focus on the patchy snow period between 10 and 17 May (Figure 4.2). As in other years, two snow patches underneath towers D and UW persisted throughout this period (Figure 4.1). These patches form on the downvalley side of topographic depressions. During our study period, winds blew downvalley 73% of the time.

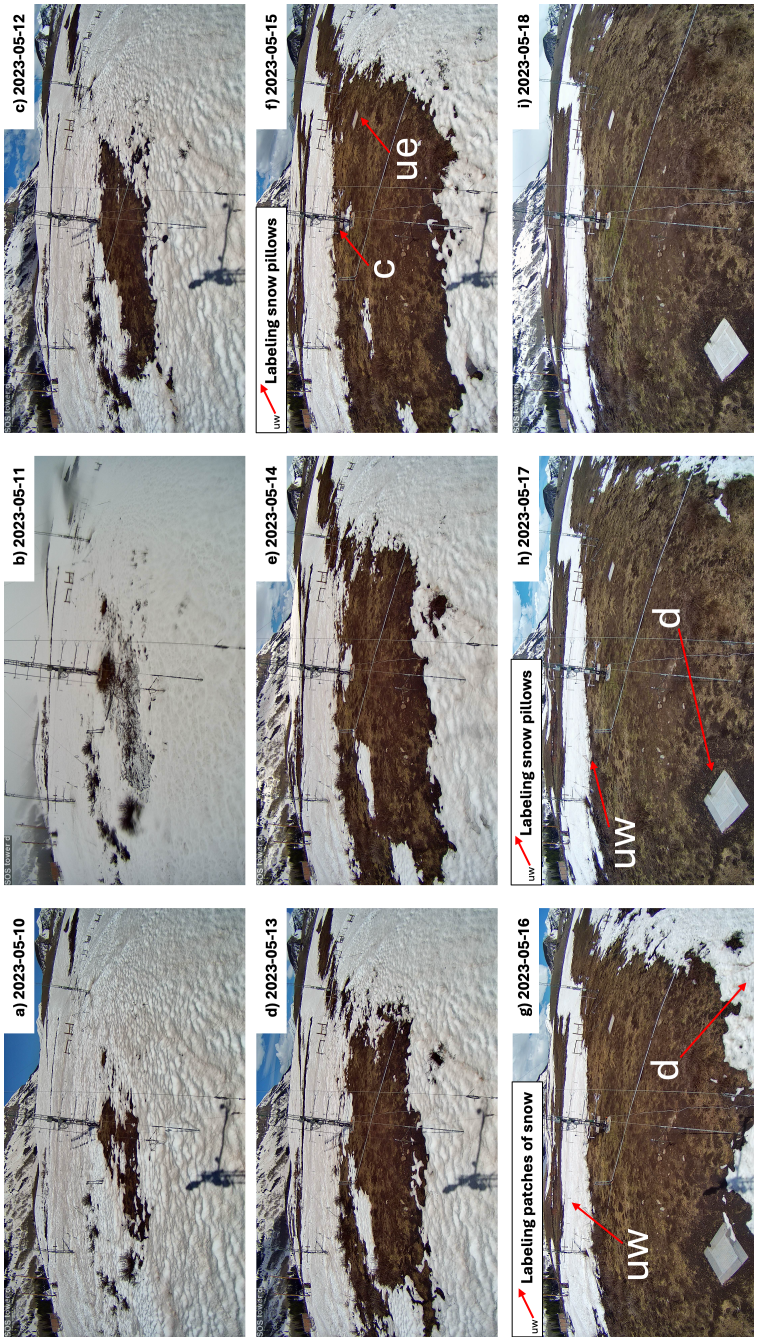

Figure 4.2: Images taken from a web camera pointed upvalley, mounted on tower D (Figure 4.1a). All images taken at 17:00 LT.

4.3 Methods

4.3.1 Theory for sensible heat advection over an isolated snow patch

In seasonally snow covered mid-latitude regions, such as the Rocky Mountains, during a spring day with patchy snow cover, bare ground temperatures can exceed 0 °C, while the surface of melting snow patches remains at 0 °C. Horizontal winds blow warmer air over snow patches, and, as the air passes over the snow surface, it is cooled. Close to the snow patch surface, where the air is cooled, an internal boundary layer (IBL) forms (Figure 4.3a). The depth of the internal boundary layer is defined by where the temperature above the snow surface equals the temperature over bareground. For this study, we assumed that turbulence over the bare ground upwind of a snow patch is well-developed, and thus the temperature profile, $T_u(z)$, upward sensible heat flux, H_u, and wind speed profile, $U(z)$, over bare ground, are horizontally homogeneous (Figure 4.3a).

The cooling of air that occurs within the IBL over a snow patch is the energy extracted from the air by the snow. If the snow surface is below 0 °C, the snow will warm as a result. If the snow surface is at 0 °C, it will melt. *Granger et al.* [2002] proposed a boundary layer integration approach to estimating the flux of energy into a snow patch. This approach is derived by integrating the conservation of energy equation in two dimensions, over the Energy Control Volume illustrated in Figure 4.3a. We begin with a two-dimensional statement of conservation of energy,

$$U(z)\frac{\partial T}{\partial x} = \frac{1}{\rho c_p}\frac{\partial H}{\partial z}, \tag{4.1}$$

where ρ and c_p are the density and heat capacity of air, H is the downwards vertical heat flux, U is the wind speed, which varies only in the vertical direction, and T is the temperature field, which varies horizontally and vertically [*Essery et al.*, 2006]. Integrating this equation across the Energy Control Volume (Figure 4.3a), horizontally from the upwind edge ($x = 0$) of a snow patch to the downwind edge ($x = X$), and vertically, from the patch surface ($z = 0$)

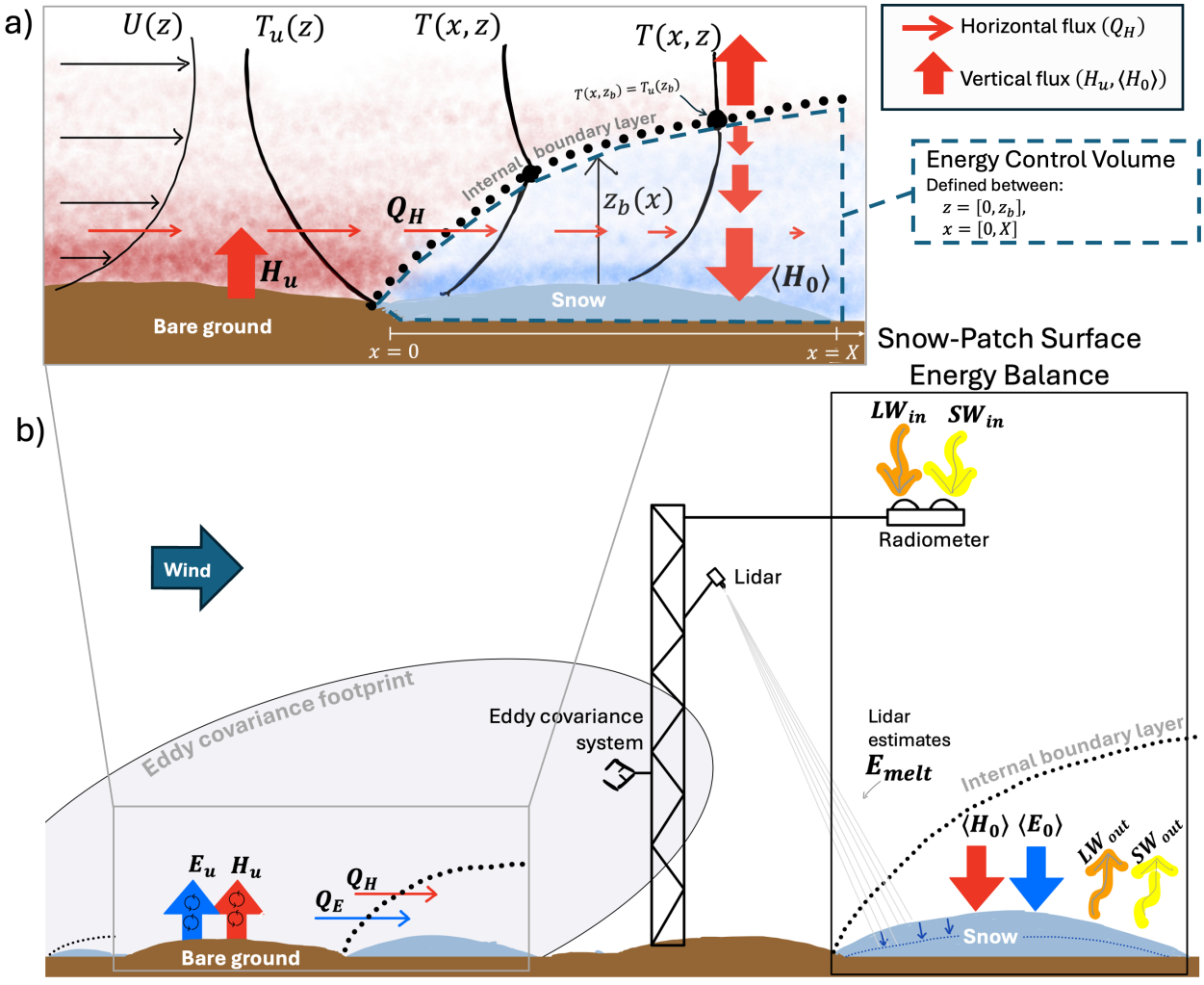

Figure 4.3: *Caption on next page.*

Figure 4.3: (a) Conceptual figure illustrating the development of an internal boundary layer (IBL) over a snow patch. $U(z)$ is the horizontal wind speed profile, which is assumed to be constant across bare ground and snow. $T_u(z)$ is the temperature profile over bare ground and $T(x, z)$ is the temperature profile over the snow, which varies with distance into the snow patch. $z_b(x)$ is the depth of the IBL formed over the snow patch, defined as the height where the temperature above snow equals the temperature above bare ground, i.e. $T(x, z_b) = T_u(z_b)$. H_u is the upward sensible heat flux over the bare ground, Q_H is the advected sensible heat, and $\langle H_0 \rangle$ is the horizontally-averaged sensible heat flux into the snow patch. Advected sensible heat (Q_H) decreases with distance into the snow patch and this horizontal flux divergence is associated with a deposition of heat into the snow patch. The conservation of heat equation (Equation 4.1) is integrated over the Energy Control Volume in the atmosphere over the snow patch, which is defined between $z = 0$ and $z = z_b$ and between $x = 0$ and $x = X$. (b) Conceptual diagram illustrating our approach to measuring the energy balance over a snow patch. The equivalent transport terms for latent heat fluxes are included ($E_u, Q_E, \langle E_0 \rangle$). The Snow-Patch Surface Energy Balance box includes all the terms in the energy balance equation (Equations 4.7 and 4.8). $\langle H_0 \rangle$ and $\langle E_0 \rangle$ are functions of terms outside the box, $\langle H_0 \rangle = H_u + Q_H$ and $\langle E_0 \rangle = E_u + Q_E$.

to the IBL height ($z = z_b$,), gives

$$\langle H_0 \rangle = H_u + Q_H \qquad | \qquad Q_H = \frac{\rho c_p}{X} \int_0^{z_b} U(z) \Big[T_u(z) - T(X, z) \Big] dz, \tag{4.2}$$

where H_u is the sensible heat flux above the bare ground upwind of the snow patch, Q_H is the advected sensible heat, and $\langle H_0 \rangle$ is the horizontally averaged sensible heat flux into the snow patch between $x = 0$ and $x = X$. With this equation, we can estimate $\langle H_0 \rangle$ using measurements or estimates of the heat flux over the upwind bare ground (H_u), the wind profile, and the vertical temperature profiles at the up and downwind edges of the snow patch [e.g. *Harder et al.*, 2017]. Note that the horizontal fluxes (advected heat, horizontal

red arrows in Figure 4.3a) decrease with distance into the snow patch; this horizontal flux divergence results in deposition of heat into the snow patch below. Additionally, a vertical flux divergence exists above the snow patch (vertical red arrows in Figure 4.3a), as the heat flux is downward within the IBL and upward above the IBL.

Note that a similar equation could be defined for humidity (latent heat) using the conservation of water vapor equation. If the air is more humid over bare ground than over snow, transport of moister air over snow will result in deposition of water onto the snow, which represents a heat flux into the snow. While we will not directly estimate latent heat advection in this study, we will consider its impacts on the snow energy balance. Similarly to the above,

$$\langle E_0 \rangle = E_u + Q_E, \tag{4.3}$$

where E_0 is the horizontally averaged latent heat flux into a snow patch, E_u is the latent heat flux above exposed bare ground upwind of a snow patch, and Q_E is the advected latent heat.

According to Equation 4.2, to estimate sensible heat advection, one must also define z_b, the height of the IBL over the snow patch. The height of IBLs is generally approximated with a power law,

$$z_b(x) = cx^b, \tag{4.4}$$

where c and b are fitted parameters [*Brutsaert*, 1982; *Granger et al.*, 2002]. The depth of the IBL is defined as the height above now where the temperature equals the temperature above the upwind bare ground (i.e. $T(x, z_b) = T_u(z_b)$, Figure 4.3a). Therefore, one could evaluate the integral in Equation 4.2 to any arbitrary height above the maximum z_b and find the same estimated advection. We used this simplification in our study.

4.3.2 Estimating sensible heat advection with an infrared video camera

On 17 May, a thin polyester sheet with an acrylate coating was rigged to a metal frame with elastic rope, oriented in the vertical plane (the "IR observation sheet", Figure 4.4).

This innovation was first presented by *Haugeneder et al.* [2023]. The sheet material instantaneously adapts to the ambient air temperature, meaning the temperature of the sheet is the local air temperature. At the sheet, we pointed a Jenoptik thermal-infrared (IR) video camera, which recorded images of the emitted spectral power of the sheet surface in the wave range 7.5–14 μm at 30 Hz. We converted spectral emittance to estimates of sheet-surface temperature using the Stefan-Boltzmann law and the emissivity of the sheet material, 0.94 [*Haugeneder et al.*, 2023]. Temperatures of the sheet, snow below, and the landscape behind the sheet are shown in Figure 4.4b. Figure 4.4c shows sheet temperatures only. Reflection and transmission by the surrounding environment and mean bias in the IR video camera's microbolometer are known to impact measured temperatures [*Pestana et al.*, 2019]. In this study, we only analyze relative differences in the measured temperatures (i.e. Equation 4.2), which are insensitive to these errors [*Haugeneder et al.*, 2023]. To minimize heating and cooling of the video camera, an umbrella was placed to protect the instrument (Figure 4.4c).

The towers holding the sheet were stationary for the entire 2022–2023 winter. Upon arrival to the site on 17 May, no snow surrounded the towers. Snow was collected and piled around the towers to form a snow patch, which spanned the width of the observation sheets (Figure 4.4a, c). No snow was taken from near the instrumented towers, nor within the footprints of the scanning lidars.

Thirty minutes of video were collected between 1200–1230 on 17 May 2023, during which winds blew downvalley. We processed the video according to the following steps. First, we took the pixel-wise temporal mean across all 30 minutes (Figure 4.4b). Second, we trimmed the edges of the frames to exclude data outside the edges of the rigged sheet, and used the height and length of the metal supports to convert image pixels into real spatial dimensions, in meters. After trimming the frames, the left edge of the sheet begins at x = 0.08 m (Figure 4.4d). After translating the image coordinate system from pixels to real space, the resolution of each video frame is 5.4x5.4 mm. Then, we removed pixels representing the snow surface, by searching, in each column from the top down, for the first temperature measurement at or below 0 °C. That pixel, and pixels below it, are removed from the dataset. The result of

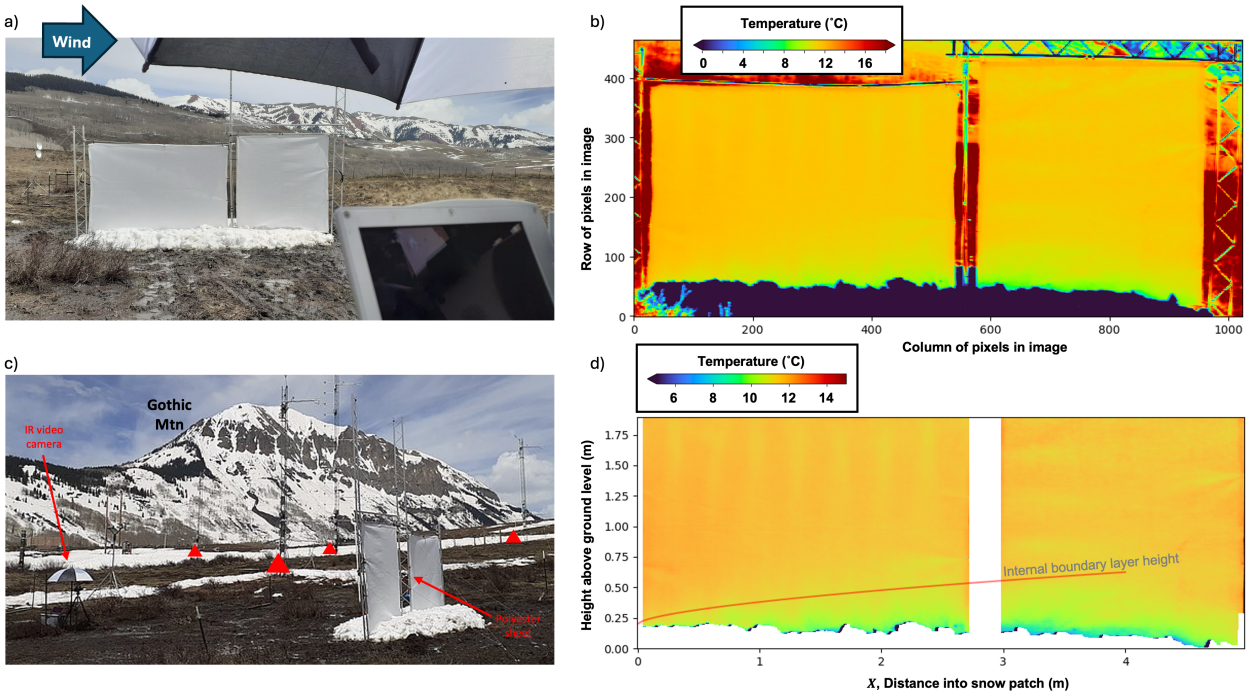

Figure 4.4: Illustration of the infrared video camera data collection method. a) Picture looking toward the northeast, illustrating the relative position of the infrared video camera and the observation sheet. b) A single frame from the infrared video camera data collection, including the landscape behind the observation sheet. c) Picture looking upvalley (northwest) showing the observation sheet, the IR video camera, and the four instrumented towers. d) 30-minute averaged temperature field collected between 12:00–12:30 LT on 17 May 2023. We removed image pixels showing the landscape behind the observation sheet (as shown in panel b) and the snow patch beneath. The red line approximates the top of the internal boundary layer using the equation of *Granger et al.* [2006], $z_b = 0.18X^{0.62}$.

these steps, a two-dimensional air temperature field, is shown in Figure 4.4d.

We used the processed data to estimate sensible heat flux into the snow patch. We extracted vertical temperature profiles at the upwind edge of the snow patch ($T_u(z) = T(x = 0.08, z)$) and at various distances into the snow patch ($T(x, z)$), which we input into Equation 4.2. We extracted $T(x, z)$ at 25 cm intervals, between $x = 0.25$ and 4.5m. We used measurements from the instrument towers to estimate the remaining inputs into Equation 4.2. For H_u, we used the sensible heat flux measured by the EC at 3-meters AGL on tower C, between 1200–1230. Theoretically, H_u should be constant upwind of the snow patch (Section 4.3.1). At 12:00-12:30 17 May, H_u measurements made by four ECs at 3 meters AGL on four towers ranged from 130–170 W/m^{-2}. These estimates are within 20% of each other, a common estimate of random error for EC flux measurements [*Stiperski and Rotach*, 2016]. To estimate $U(z)$, we used the 3-meter EC measurement of U and shear velocity, $u_* = (\overline{u'w'}^2 + \overline{v'w'}^2)^{1/4}$, to calculate z_0 and fit the vertical velocity profile,

$$U(z) = \frac{u_*}{k}\ln\Big(\frac{z + z_0}{z_0}\Big). \tag{4.5}$$

This equation ignores the effects of atmospheric stability on the velocity profile, which is small in a shallow IBL [*Essery et al.*, 2006]. We calculated z_0 using measurements from an EC on tower C, which is approximately 50 meters upwind of the snow patch (Figure 4.1). The upwind fetch for tower C and the observation sheet are similar, so the calculated z_0 value is likely representative of the flow that interacts with the measured snow patch. Finally, we evaluated Equation 4.2 via numerical integration at each horizontal interval where we extracted $T(x, z)$ values. We integrated Equation 4.2 from 0 to $z_b = 0.6$ meters, which we visually determined is the maximum height of IBL (Figure 4.4d). The IBL height shown in Figure 4.4d is the function presented in *Granger et al.* [2006], $z_b = 0.18X^{0.62}$. The numerical integrations result in estimates of $\langle H_0 \rangle$ and $Q_H(x)$ for values of x across the IR observation sheet. Because the sheet extended over the entirety of one snow patch, we can estimate the average heat flux into the entire patch. However, we will also estimate sensible heat fluxes into snow patches of arbitrary width (Section 4.3.5). To do so, we used measurements of

$Q_H(x)$ over the snow patch to fit the function

$$Q_H = \alpha x^{\beta} \tag{4.6}$$

where α and β are fitted parameters. This function describes the decay in sensible heat advection with distance into the snow patch, which arises from the decay in the growth of the IBL with distance into the snow patch (e.g. Equation 4.4). The power law Equation 4.6 has been utilized in previous studies. *Granger et al.* [2002] found b=-0.47 for strong turbulence. *Harder et al.* [2019] used the same power law to implement a bulk advection scheme in a one-dimensonal energy balance snowmelt model, and provided functions for α and β, which depend on wind velocity, snow and bare ground surface temperatures, and surface roughness. In our results, we present the parameters in Equation 4.6 fitted to our measurements, and compare them with parameters presented in previous studies.

4.3.3 Measuring the snow pack energy balance

To estimate the relative contribution of sensible heat advection to the surface energy balance over a patch of snow (Research Question 2), we estimated the energy fluxes in a snow-patch surface energy balance,

$$E_{melt} = R_{net} + \langle H_0 \rangle + \langle E_0 \rangle = R_{net} + H_u + Q_H + E_u + Q_E, \tag{4.7}$$

where E_{melt} is the energy that goes towards melt of the snow patch and R_{net} is the horizontally averaged net radiative flux into the patch. R_{net} is the sum of the incoming longwave and shortwave radiation and outgoing longwave and shortwave radiation, $R_{net} = LW_{in} + SW_{in} - LW_{out} - SW_{out}$. Figure 4.3b diagrams the relevant energy fluxes and the instruments we used to measure them. Relative to other snow surface energy balance equations presented in the literature [e.g. *Lundquist et al.*, 2024], ours is simple. We excluded the ground heat flux term, which characterizes heat from the earth warming the snow, and the heat storage term, which represents changes in the temperature of the snowpack. Ground heat fluxes are generally small, on the order of 1 Wm^{-2}. During the melt season, snowpack temperatures

do not fluctuate much. At Kettle Ponds and at another nearby site, the snowpack was isothermal and reached 0 °C by mid April 2023 [*Lundquist et al.*, 2024; *Cox et al.*, 2025b]. Similar simplifications to the energy balance were also made by *Van Der Valk et al.* [2022] in their patchy snow melt study.

We only measured Q_H on one day, 17 May, with the IR observation sheet, and we did not measure Q_E. We measured the remaining terms in the energy balance continuously throughout our study period. When we present energy balance results, we use the following form of the energy balance,

$$E_{melt} = R_{net} + H_u + E_u + Res, \tag{4.8}$$

where Res is calculated from the other measured terms. Non-zero Res could be explained by non-zero Q_H or Q_E, by other energy fluxes we do not account for, such as heat storage in the air or snow, or by error in our measurements. We estimated each term in Equation 4.8 at hourly resolution for the duration of our study period. Below, we describe how we estimated each term.

Estimating snow melt energy with snow pillows and scanning lidar

We estimated E_{melt} using four, fluidless snow pillows and two scanning lidars deployed at Kettle Ponds. Snow pillows are scales that are buried into the dirt such that a 0.9x0.9 m^2 (3x3 ft^2) scale platform is flush with the ground surface. One snow pillow was deployed near the base of each tower at the site (e.g. Figure 4.2h). The pillows recorded the snow water equivalent (in units of meters) on the scale throughout the winter season at a 5 minute resolution, which we upsampled to hourly means. The snow pillow measurements contain a diurnal systematic error associated with temperature fluctuations. We applied a cumulative minimum to the hourly time series to remove erroneous increases in snow mass recorded in May. We then calculated the rate of snow mass change, $\frac{\mathrm{d}SWE}{\mathrm{d}t}$ (m/hr), by differentiating the time series using the second order central difference. Finally, we calculated the hourly melt energy (in W/m^{-2}) assuming the specific heat of fusion is $L_f = 334$ kilojoules/kilogram and

the density of water is $\rho_w = 1000$ kg/m^3,

$$E_{melt} = L_v \rho_w \frac{\mathrm{d}SWE}{\mathrm{d}t}. \tag{4.9}$$

Equation 4.8 describes the surface energy balance averaged over a snow patch. However, snow pillow estimates of E_{melt} are representative of a very limited area. Estimates of E_{melt} over the full extent of a snow patch are more appropriate for our snow-patch surface energy balance approach (Figure 4.3b). During our study period, two scanning lidars continually observed the melt of the two distinct snow patches that formed underneath towers UW and D (Figure 4.1g). We estimated E_{melt} with the scanning lidar measurements, and used the snow pillow-based estimates to evaluate the lidar-based estimates.

To estimate melt energy over the two persistent snow patches at the site (Figure 4.1c, g), we used lidar scans to measure the change in snow depth, which we converted to snow melt rates by assuming a snow density. The lidars scanned every 5 minutes; we only used scans collected at the beginning of each hour. From the lidar point clouds, we generated a time series of surface-elevation grids at 5 cm horizontal resolution. For each grid cell, we assigned the minimum elevation of all points falling within that cell, producing a sequence of gridded digital surface models (DSMs). Due to reflection of light across variable snow surfaces and the emergence of vegetation during our study period, the hourly snow depth changes we calculated by spatially averaging across the DSMs were noisy. To reduce noise, we manually selected six horizontal transects with minimal noise and calculated snow depth change only along the transects (Figure 4.1c). For each pixel in the hourly transects, we applied a cumulative minimum function, same as for the snow pillows. We then calculated the pixel-wise rate of snow depth change (m/hr) by differentiating each pixel's time series of surface elevation using the second order central difference. Finally, we calculated the hourly melt energy for each transect by averaging snow depth change across all pixels. The six estimates of transect-averaged snow depth change rates are then converted to melt energy by assuming a snow density of $\rho_{snow} = 400$ kg/m^3 and using the specific heat of fusion (L_f),

$$E_{melt} = L_f \rho_{snow} \frac{\mathrm{d}h_{snow}}{\mathrm{d}t}. \tag{4.10}$$

The estimate for ρ_{snow} comes from field measurements of melting snow [*López-Moreno et al.*, 2013]. In our results, we evaluate this assumed snow density by comparing lidar-based and snow pillow-based melt estimates.

Estimating radiative fluxes

To estimate R_{net}, we used measurements of LW_{in} and SW_{in} collected by a Hukseflux NR01 4-stream radiometer, mounted on tower UW. We did not use the radiometer's measurements of outgoing radiation, as we are considering an energy balance at the surface of a snow patch, and the radiometers downward facing sensors have a field of view that included both bare ground and snow during our study period (Figure 4.3b). We calculated LW_{out} for a snow patch using the Stefan-Boltzmann equation,

$$LW_{out} = \sigma \epsilon T_s^4 \tag{4.11}$$

where σ is the Stefan-Boltzmann constant, $5.67e^{-}8$ W m^{-2} K^{-4}, ϵ is the emmisivity of snow, which we set to 0.98 [*Raleigh et al.*, 2013], and T_s is the snow surface temperature. We used the infrared radiometer deployed on tower UW to measure T_s. Although we deployed infrared radiometers on all four towers, only the UW instrument had snow within its viewing angle for the entirety of the study period. We calculated SW_{out} for a snow patch by assuming a snow albedo of 0.6, which was the albedo measured over the snow at Kettle Ponds in early May, before snow became patchy [*Lundquist et al.*, 2024].

Estimating turbulent heat fluxes

To estimate H_u and E_u, we used 30-minute EC measurements from the Kettle Ponds site, upsampled to hourly averages. Ogive analysis (not shown) indicates that 30-minutes is an appropriate Reynolds averaging timescale for both fluxes [*Foken et al.*, 2006]. Note that for our snow-patch surface energy balance approach, H_u and E_u should be the heat fluxes over bare ground upwind of a snow patch (Figure 4.3a). However, EC instruments measure aggregated fluxes over a large footprint (Figure 4.3b), and upwind of the instrument towers,

during our study period, there is both snow and bare ground (Figure 4.1g). This means that the measured E_u and H_u may be lower than true fluxes over just bare ground. We discuss this issue further after presenting our results.

4.3.4 Measuring snow covered area with high resolution satellite imagery

To characterize fractional snow covered area (fSCA, e.g. Figures 4.1d–i) over the Kettle Ponds site and the surrounding area, we used Planet imagery, which provides near-daily coverage at 3-meter resolution [*PBC*, 2020/2025]. To identify fSCA, we used a pre-trained Random Forest model that classifies each pixel in an RGB image as snow or not snow [*Yang et al.*, 2023; *Chiu et al.*, 2025]. We selected 11 total Planet images for use in this study. We selected one image during the melt season for each year between 2020–2025 (six total images), to illustrate the persistence of snow patches on the landscape at Kettle Ponds (Figure 4.1d – i). We also selected all images with minimal cloud cover during our 10–17 May 2023 study period, as well as images on 9 and 23 May 2023 (Figure 4.10di–dvi). We then cropped these images to a ±150 meter square around tower C at Kettle Ponds, and calculated fSCA maps with the model described above. The resulting fSCA maps cover a 300x300 m^2 area.

4.3.5 Estimating sensible heat fluxes across the landscape

Our formulation of the snow patch surface energy balance (Equation 4.8) includes a residual term, *Res*. According to Equations 4.7 and 4.8, this residual represents the combined contribution of sensible and latent heat advection. To address our second research question, we compare *Res* to our independent estimates of sensible heat advection. This comparison allows us to assess how strongly advection contributes to snowmelt: if both the residual and our advection estimates are large, this would support the conclusion that advection plays a significant role in melting the snow.

While we measured sensible heat advection over a single snow patch for 30-minutes on 17 May using an IR video camera (Section 4.3.2), we want to estimate sensible heat advection throughout our study period, so we can compare all terms in our energy balance. Equation 4.6

allows us to model sensible heat advection for snow patches of arbitrary width. We estimated the distribution of snow patch widths surrounding Kettle Ponds using fSCA maps from 4 separate days and then estimated sensible heat advection for the distribution of snow patches with Equation 4.6. We did this with the following steps. First, we created an ensemble of 105 lines oriented along the 315° bearing, the dominant wind direction, separated in the north-south direction by 5 meters, which results in an even distribution of lines across our domain (Figure 4.5a). Second, for each 2023 fSCA image (Figures 4.10di–dvi), we extracted

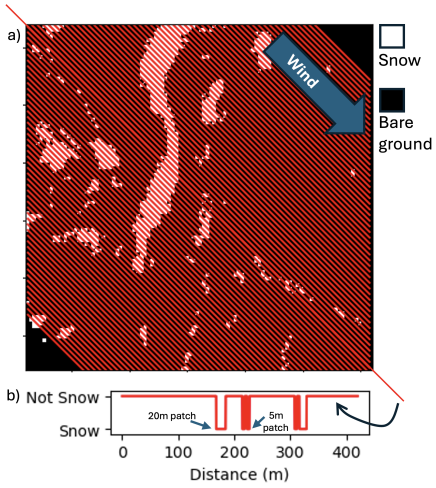

Figure 4.5: a) fSCA map from 2023-05-16 (recreated from Figure 4.1g), overlayed with lines aligned with the wind direction. b) Example of values extracted from the fSCA map along one line. Continuous segments of snow define the width of snow patches encountered in the along-wind direction.

pixel values along each line. For each line, we calculated the length of all segments with continuous snow cover (Figure 4.5b). The distribution of segment lengths is the distribution of snow patch widths. We then plug in the patch width distribution for x in Equation 4.6, which results in a distribution of Q_H. This distribution represents the range of sensible heat advection magnitudes expected to influence snow patches over the 300x300 m^2 study domain. We only present patch length and Q_H distributions for days when fSCA is smaller

than 62%, as fSCA maps show that when fSCA is larger, the landscape is characterized by bare ground patches embedded in snow, a situation for which Equation 4.6 is not suited (see Section 4.3.1).

4.4 Results and Discussion

4.4.1 Estimating advective sensible heat fluxes with an infrared camera

We measured sensible heat flux into a snow patch, $\langle H_0 \rangle$, using the infrared camera data and Equation 4.2 (Research Question 1). First, we had to calculate z_0, and found $z_0 = 0.0079$

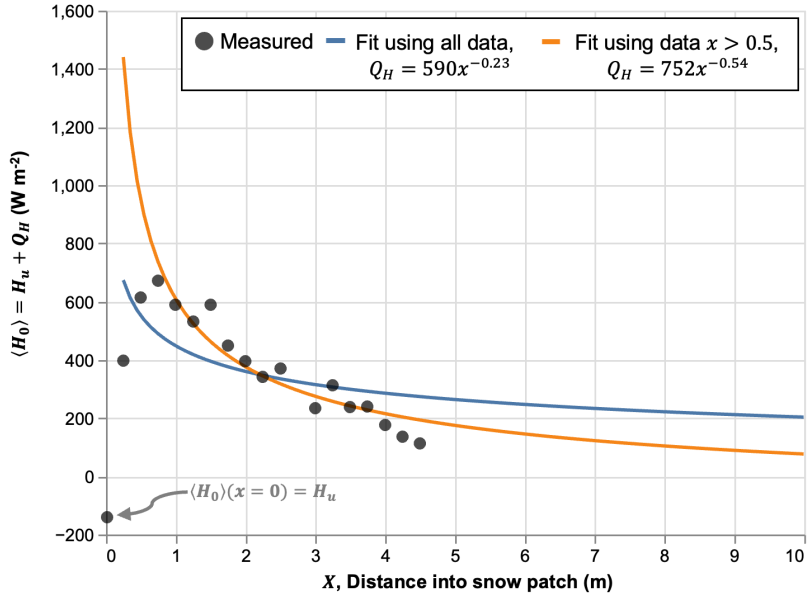

Figure 4.6: Measured and predicted heat flux into a snow patch. Measured data (grey points) are calculated using Equation 4.2 and the mean temperature field collected over 30-minutes by the infrared video camera (Figure 4.4d). The blue and orange lines show Equation 4.6 fitted to the measured data using the least squares method. The blue line was fit including all measured points, the orange line was fit to all measured points except those measured at $x < 0.75$m.

m. This roughness is consistent with a surface composed of a mix of mud flats ($z_0 = 0.005$)

and flat terrain with isolated obstacles (z_0 = 0.03) [z_0 values from *Wieringa*, 1980]. Our $\langle H_0 \rangle$ estimates from the infrared video camera are shown as dots in Figure 4.6. Within the first 75 cm of the patch, $\langle H_0 \rangle$ increases, reaching 700 W m^{-2} at x = 0.75, and then decreasing to around 100 W m^{-2} by x = 4.5 meters. The observed exponential decay in $\langle H_0 \rangle$ with distance into the patch is predicted by theory. With distance into the snow patch, the IBL depth grows, the vertical temperature gradient decreases, the horizontal temperature gradient decreases, and Q_H decays (visible in Figure 4.4d, illustrated in Figure 4.3a). *Granger et al.* [2002] predicted that the decay would follow a power law, Equation 4.6, with b = -0.47 for strong turbulence. When we excluded the two measured data points between $x = 0 - 0.75$ meters, we found b=-0.54 (0.5368 ± 0.0015 using a 10% confidence interval), and the curve fits most of the data points closely (Figure 4.6, orange line). *Van Der Valk et al.* [2022] used direct numerical simulation to estimate sensible heat advection over snow patches and estimated b=-0.35. Overall, our data conforms to established theory quite well, apart from the initial increase in $\langle H_0 \rangle$ in the first 75 centimeters of the snow patch. When we fit the power function to all the measured data, we found b=-0.23 (Figure 4.6, blue line), which is outside the range of possible parameter values predicted by *Granger et al.* [2002]. The initial increase in $\langle H_0 \rangle$ could be due to the fact that our snow patch was piled approximately 20 centimeters above the ground (Figure 4.4a). The height of the snow pile forces flow approaching along the ground to rise, which could lead to flow separation and decreased turbulent exchange at the windward edge. This highlights one problem with our experimental set up. Additionally, our measurements beyond x = 75 cm appear more linear than exponential, potentially suggesting that existing models predicting exponential decay are incorrect. Future measurements with an IR camera or closely spaced towers should attempt to measure over wider snow patches than we measured, to further explore whether $\langle H_0 \rangle$ and Q_H decay linearly or exponentially with distance into a snow patch. In any case, the decent match between $\langle H_0 \rangle$ measurements and predictions led us to use the fitted function (Figure 4.6, orange line) to estimate advection over other patches near the site.

4.4.2 Monitoring snow patch evolution with scanning lidar

We calculated hourly snowmelt rates for 10–17 May from 1 dimensional transects of surface elevation over melting snow patches. Before examining the snow melt rates, we examined the evolution of the snow surface elevation, shown in Figure 4.7. The transect numbers in Figure 4.7 correspond to the transects in Figure 4.1c. Figures 4.7a, b, and c show the melt

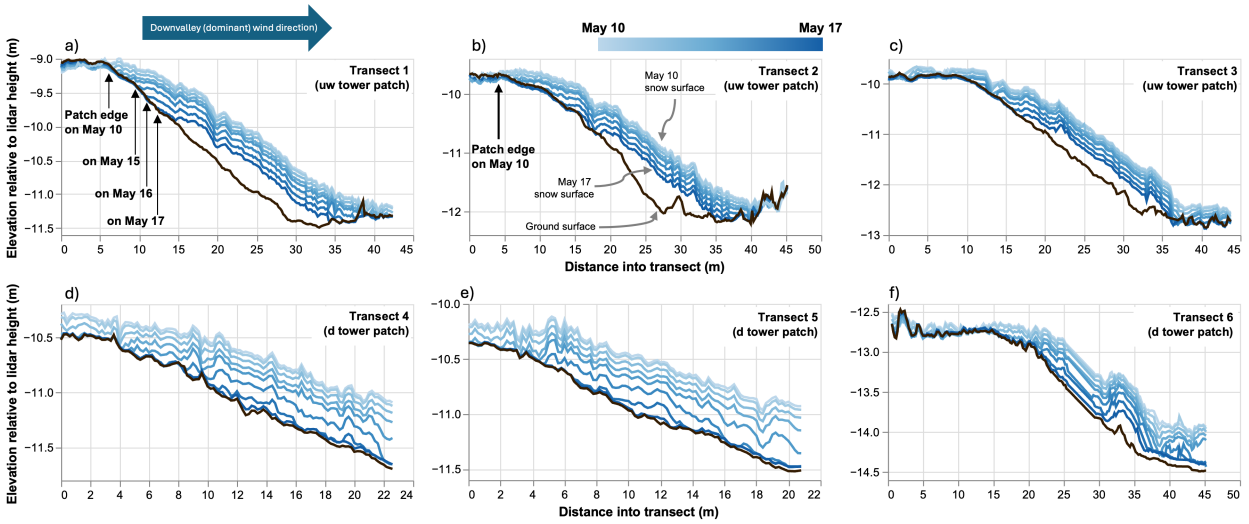

Figure 4.7: Surface elevations extracted over the six transects (Figure 4.1c) from lidar scans. One surface elevation transect is shown for each day between 10–17 May, from the scan collected at 00:00 LT. Blue lines show the changing snow surface. The black line shows the underlying topography. In panels a and b, black arrows point to the upvalley edge of the snow patch.

out of the snow patch beneath tower UW and illustrate that snow patches persist in concave topography. By 17 May, the uphill side of all the patches receded below the top of the local topographic highs (e.g. Figure 4.7a, see "Patch edge"). Figures 4.7d, e, and f show the melt out of the snow patch beneath tower D. Transects over this patch clearly show that melt rates accelerated between 10–17 May. They also show that the tower D snow patch had mostly disappeared by 16 May. Therefore, our estimates of snow melt, presented later, only

include measurements from transects 1–3 starting on 16 May.

Our measurements of transects 1 and 2 capture the uphill (windward) edge of the snow patch from the beginning of the measurement period on 10 May (Figures 4.7a and b, see "Patch edge"). Using these two transects, we examined how melt rates varied with distance from the upwind patch edge. Because heat advection decays with distance into a snow patch (Figure 4.6), we expect that melt rates decay as well. We calculated mean melt rates for bins of distance from the patch edge. We adjusted the location of the patch edge at the beginning of each day to follow the movement of the patch edge as it receded downslope (e.g. Figure 4.7a). We then normalized the bin-averaged melt rates by the time-and-space-averaged melt rate (Figure 4.8). We assumed that errors from lidar measurements are normally

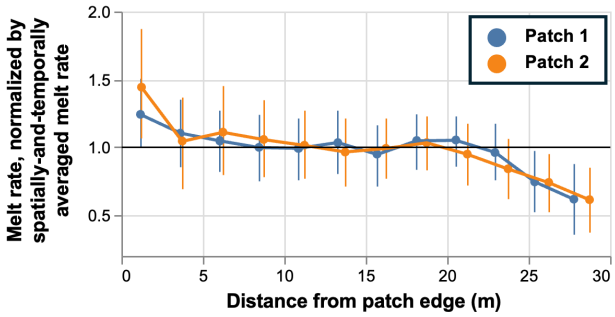

Figure 4.8: Normalized snow surface melt rates as a function of distance from the upwind snow patch edge. Change rates are calculated from surface elevations using second order central differencing. Rates are then normalized by the temporally and spatially averaged rate. Dots show the mean for bins of distance from the patch edge. Bars show the 95% confidence interval around the mean; we assumed errors are normally distributed.

distributed, and show both the mean melt rate for bins of distance-from-patch-edge and the 95% confidence interval around that mean. For both transects, melt rates within 5–10 meters of the patch were between 1–1.5 times larger than average melt rates, and melt rates greater than 20 meters from the patch edge were 0.6–1.0 times the average rate. These results are similar to previous findings, with some slight differences. *Van Der Valk et al.* [2022] measured

melt rates at the front and back edges of a snow patch using Structure from Motion, and found that melt rates at the front edge were 1.8 times higher than average. *Mott et al.* [2011] measured melt rates with lidar and found that melt rates decreased exponentially with distance into the snow patch, with melt rates at the front edge 1.1–1.6 times higher than average, and melt rates beyond 5 meters into the patch lower than average. Our measurements diverge from the findings of *Mott et al.* [2011] in that below-average melt rates were only found near the downwind snow patch edge, beyond 20 meters into the patch. The reason for this pattern is unclear, but it may have to do with the complex topography that contains transects 1 and 2 (Figures 4.7a and b, black lines). Note that while Figure 4.8 includes data from our entire study period, we repeated the analysis separately for melt rates during downvalley winds (73% of our study period) and melt rates during non-downvalley winds (27%). We found that the pattern observed in Figure 4.8 remained for downvalley winds, while during the other winds, there was no significant variation in melt rate with distance (not shown). This adds confidence to our lidar-based melt measurements, as we would expect increased melt rates on the upwind side of the patch.

Snow patches commonly form in topographic depressions, due to preferential deposition during blowing snow transport. Previous authors have hypothesized that snow patches in topographic depressions may experience reduced heat fluxes due to lower wind speeds in the depressions and atmospheric decoupling [*Mott et al.*, 2015], which further preserves the snow patch in a self-regulating manner [*Fujita et al.*, 2010]. We found that melt rates were increased at the upwind edge of a snow patch in a topographic depression, which suggests that horizontal advection is contributing to the snow melt. Additionally, we observed that melt rates actually increased over our study period (e.g. Figures 4.7a and e), even as the snow patches receded below the upwind topographic highs and were theoretically more protected from winds. We conclude that decoupling was uncommon at our site. This is further supported by comparing the melt rates of transects 1–3, which formed in more concave topography than transects 4–6 (Figure 4.7, compare black lines). In one study in the Swiss Alps, *Mott et al.* [2013] found that snow ablation rates measured over a snow patch within

a depression were smaller than ablation rates of patches on slopes. We observed no major differences in the melt rates of the two patches (not shown).

4.4.3 Estimating snow melt energy with scanning lidar and snow pillows

From the lidar measurements of six transects, we calculated the transect-averaged vertical snow surface decay rates and converted to snow melt rates ("lidar-based melt rates"), assuming a snow density of 400 kg m^{-3}. We compared lidar-based melt rates with the rates measured by four snow pillows. The four separate snow pillow measurements and the mean, minimum and maximum of the six lidar transect measurements are shown in Figure 4.9. Snow melt rates generally increased over the study period, and 15–17 May had the highest

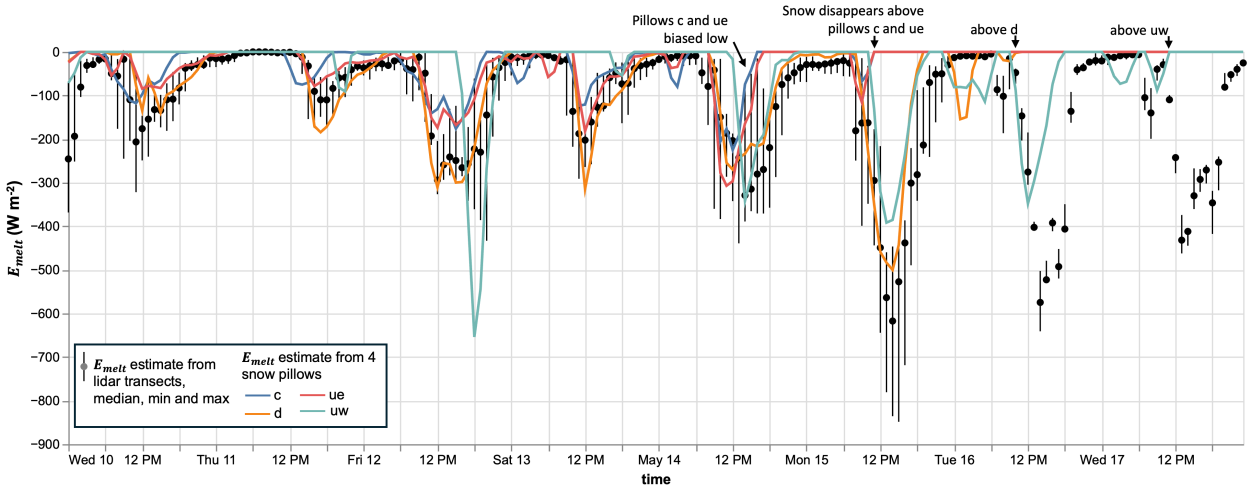

Figure 4.9: Snow melt energy estimated from snow pillows and lidar. Snow pillow and lidar change rates are calculated using second order differencing. Lidar surface elevation change rates are converted to mass change rates assuming a snow density of 400 kg/m^3. Grey dots and bare show the median and IQR of E_{melt} estimates from six snow patches. The colored lines show the E_{melt} estimates from the four different snow pillows. Snow melted out above the snowpillows throughout the study period; these times are indicated by arrows and the snow pillows become visible in Figure 4.2.

daily melt rates. On 15 May, snow melted out above the snow pillows at tower C and UE (Figures 4.9 and 4.2f), and by 17 May, snow had melted out above the tower UW and D snow pillows (Figure 4.2h). Our lidar measurements appear to be more reliable for estimating E_{melt}. Snow pillows exhibit a low bias in the 24–48 hours before snow entirely disappears above them, and the UW snow pillow shows little to no melt in the first 4 days of our study period, perhaps due to the pooling of water in the snowpack [*Lundquist et al.*, 2024], which would compensate for any mass lost, or due to snow-bridging, when a hard layer in the snowpack forms and reduces pressure on the pillow scale [*Sorteberg et al.*, 2001]. Comparing the mean of all the lidar estimates and the mean of the snow pillow estimates, excluding the UW snow pillow, the melt rates matched with an r^2 of 0.57 and a mean bias of 37%, with lidar melt rates generally larger than pillow rates.

4.4.4 Snow melt and the surface energy balance

To estimate the contribution of sensible heat advection to the energy balance over patchy snow (Research Question 2), we estimated all terms in the energy balance (Equation 4.8) and plotted them together for comparison (Figure 4.10c). The spread in *Res* is calculated from the spread in E_{melt}, which represents the spread in the lidar measurements across the six transects. There are other sources of error that could contribute to the residual term; we will discuss these later. We also present daily mean and daily maximum energy fluxes for four days during the study period in Table 4.1. To illustrate the onset of snow patchiness at the site scale, we plotted surface temperatures measured by four radiometers on each tower (Figure 4.10a); surface temperatures of 0 °C indicate the presence of snow cover. Snow patchiness at the EC footprint scale is illustrated with fSCA maps for each day during our study period with satellite imagery, plus one day on either end (Figure 4.10di–div).

Before 15 May, sensible heat fluxes measured by the EC method (H_u) were positive (Figure 4.10c). Positive (downward) H_u is common over snow cover, when the atmosphere above the snow surface is warmer. This indicates that prior to 15 May, snow dominated the landscape within the EC footprint, and heat advection over snow was likely minimal.

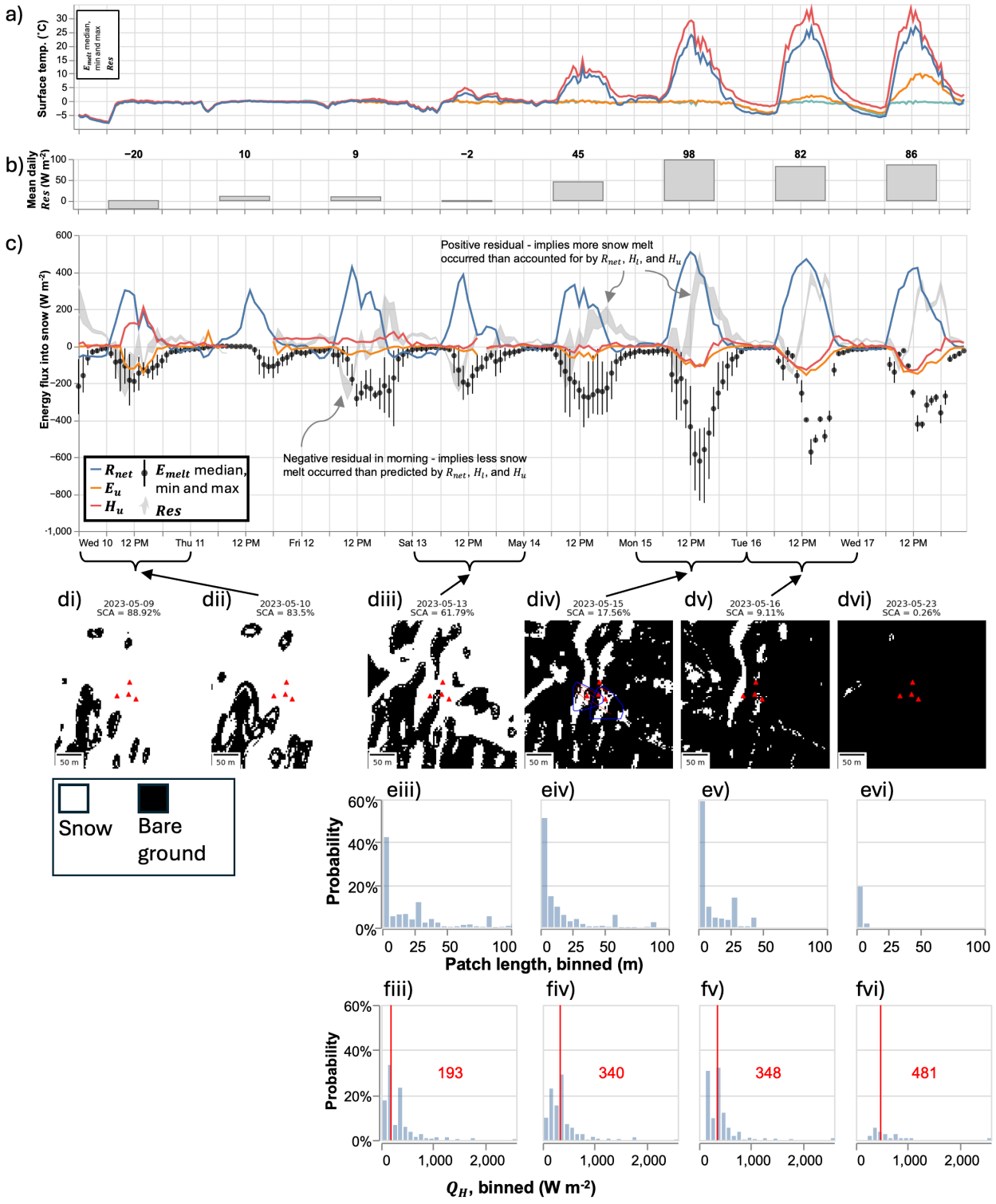

Figure 4.10: *Caption on next page.*

Figure 4.10: a) Time series of surface temperatures measured by four radiometers, one mounted on each tower at the Kettle Ponds site. b) Mean daily *Res*, calculated from hourly *Res* fin panel c. c) Energy balance terms from Equation 4.8. Net radiation, R_{net} is calculated from measurements of incoming shortwave and longwave, calculated outgoing shortwave assuming snow albedo of 0.6, and calculated longwave using the measured snow surface temperature from tower UW, shown in Panel a. Vertical turbulent sensible and latent heat fluxes (H_u and E_u, respectively) are measured by an eddy covariance system 3 meters above the ground on the tower C at Kettle Ponds. E_{melt} shows the median, minimum, and maximum of snow melt rate estimates from the six snow patches measured by lidar (also shown in Figure 4.9). *Res* is calculated from the other terms, e.g. Equation 4.8. The spread in *Res* is calculated from the spread in E_{melt}. d) Snow covered area (SCA) maps from six days in May overlapping with the study period. Includes copyrighted material of Planet Labs PBC. All rights reserved. e) Distribution of patch lengths calculated from the fSCA maps shown in the panels diii–dvi. f) Distribution of Q_H calculated using Equation 4.6, plugging in for X the distribution of patch lengths shown in panels eiii–evi. We do not show patch lengths for advection estimates prior to 13 May because, prior to that date, snow cover was too large to estimate sensible heat advection

Starting on 14 May, H_u was consistently negative, suggesting that bare ground dominated the EC footprint. We can see that bare ground dominates the landscape by May 15, when fSCA was 18% (Figure 4.10div); no satellite imagery was available for 14 May. Latent heat fluxes measured by the EC method (E_u) were negative or near-zero throughout the study period. Negative (upward) E_u represents evaporation or sublimation, positive E_u would represent condensation on the surface. Interestingly, both H_u and E_u remained near zero on 13 May, which suggests that, averaged over the EC footprint, both vertical turbulent sensible and latent heat fluxes averaged out to zero, and horizontal advection of both sensible and

	Daily mean			Daily max		
date	E_{melt}	Res	R_{net}	E_{melt}	Res	R_{net}
2023-05-14	-116	45	98	-329	181	331
2023-05-15	-192	98	154	-617	434	508
2023-05-16	-158	82	156	-575	375	470
2023-05-17	-136	86	132	-432	350	423

Table 4.1: Daily mean and maximum energy fluxes for the three largest energy flux terms in the energy balance, as shown in Figure 4.10c. We only include calculated values for days when fSCA was likely or confirmed less than 50%.

latent heat had begun. Truly zero H_u and E_u would suggest that, within the EC footprint, all the heating of the atmosphere by bare ground was balanced by cooling of the atmosphere by the snowpack, and all evaporation over bare ground was balanced by condensation over the snowpack. By 14 May, both fluxes dipped below zero, suggesting that bare ground dominated the EC footprint; although we can only confirm fSCA < 0.5 on 15 May (Figure 4.10div).

Net radiation followed a typical diurnal solar cycle (Figure 4.10c). Some days during our study period had intermittent cloud cover, which explains mid-day downward spikes in net radiation, e.g. at 12pm on 12 May. At night, negative net radiative fluxes indicate longwave cooling of the surface, which we observe in the measurements of surface temperatures over both snow and bare ground, with both slowly decreasing at night (Figure 4.10a).

Our estimates of snow melt energy (E_{melt}) generally follow the diurnal cycle of net radiation, and E_{melt} is generally larger in magnitude than R_{net}(Figure 4.10c). For most of the study period, the residual term was non-zero, indicating that the energy flux terms we measured did not balance all of the observed snowmelt (Equation 4.8). During many days, the morning transition (0900–1100) was characterized by a negative residual, meaning more

energy was available for melt than ocurred. This is likely due to the energy taken to warm up the sub-zero snow surface, which froze and dipped below 0 °C overnight (Figure 4.10a). In the morning, the snow must warm up to zero before melting. This is especially apparent on May 16 and 17, when snow surface temperatures reached -5 °C over night, and, in the morning, there was a negative residual and a 1–2 hour delay between the increase in net radiation around 0900 and the onset of snow melt around 1000–1100.

Between 14–17 May, the residual became positive by around 12pm, and decreased at the end of the day alongside E_{melt}. According to our energy balance (Equations 4.7 and 4.8), the positive residual indicates that sensible and latent heat advection were contributing to snow melt. We estimated sensible heat advection over the distribution of patches near our measurement site. To do this, we first estimated the distribution of snow patch widths at our site from the available fSCA maps (Figure 4.10eiii–evi) and then estimated horizontal advection over all the patch lengths (Figure 4.10fiii–fvi). Between 15–17 May, we measured mid-day peak energy balance residuals of 350–434 W m^{-2} (Figure 4.10c and Table 4.1) and average estimated sensible heat advection of 340–481 W m^{-2} (Figure 4.10fiii–fvi). Between 13–15 May, the peak residual increased from 82 to 434 W m^{-2}, and the average sensible heat advection increased from 193 to 340 W m^{-2}. We only present Q_H results for 13 May onwards, because, during large fSCA, our model for advection does not apply (see Section 4.3.1). As fSCA decreases (Figure 4.10di–dvi), average snow patch length decreases (Figure 4.10eiii–evi), average Q_H increases (Figure 4.10fiii–fvi), and daily average Res increases (Figure 4.10b). On 15 and 16 May, the two days during our study period with measured fSCA $< 50\%$, our estimates of average Q_H, 340 and 348 W m^{-2}, respectively (Figure 4.10fiv and fv), account for most of the observed peak energy balance residual of 434 and 375 W m^{-2} (Figure 4.10c). We found that before 14 May, when fSCA was above 50%, the mean daily energy balance residual was less than or equal to 10 W m^{-2}; after, the residual ranged from 45–98 W m^{-2} (Figure 4.10b).

4.4.5 The changing influence of sensible advection in the snow patch energy balance

Our energy balance observations appear to measure the onset of sensible heat advection during the patchy snow period of the 2023 melt season. When fSCA was high and snow mostly covered the landscape on 10 May, net radiation balanced snow melt, *Res* was near-zero or negative, and advective effects were likely negligible at Kettle Ponds. This is consistent with previous studies that found snow melt is dominated by radiation early in the season [*Mott et al.*, 2011]. Between 14–17 May, when fSCA fell below 50%, the energy balance residual became positive, ranging from 181 to 434 W m^{-2}. Over the same time period, estimates of sensible heat advection across the landscape ranged between 340–481 W m^{-2}, accounting most or all of the energy balance residual. Similarly, *Mott et al.* [2011] found that heat fluxes became increasingly important as the snow becomes patchy. Considering daily mean behavior, we found that the daily mean energy balance residual was less than 10 W m^{-2} before 14 May, and increased starting on 14 May (Figure 4.10b), coincident with the decrease in fSCA below 50% Overall, our measurements strongly suggest that sensible heat advection contributed to snow melt. While *Mott et al.* [2013] found that advection only contributed to snow melt when wind velocity exceeds 5 m/s, during our study period, wind velocities rarely exceeded 5 m/s (not shown). This disagreement suggests that advection processes are highly sensitive to local conditions, and vary across regions.

4.4.6 Evidence of latent heat advection

Thought we did not estimate latent heat advection, it is likely that over patchy snow near Kettle Ponds, latent heat advection contributed to snow melt. This hypothesis is supported by the fact that our estimates of sensible heat advection (Figure 4.10fiii–fvi) are often slightly less than the observed energy balance residual (Figure 4.10c, also Table 4.1). On May 16 and 17, estimated sensible heat advection (340 and 348 W m^{-2}) accounted for 91 and 99% of the mid-day peak energy balance residual (375 and 350 W m^{-2}). This suggests that latent heat advection is much smaller than sensible heat heat advection at our site. Previous studies

found that latent heat advection can be on the same order of magnitude as sensible heat advection [*Harder et al.*, 2017; *Van Der Valk et al.*, 2022]. Perhaps latent heat advection is smaller in the relatively dry environment of the Colorado Rocky Mountains than in the Canadian prairies (*Harder et al.*) or in the mountains of Norway (*Van Der Valk et al.*), further suggesting that advection processes vary across regions with seasonal snow cover.

4.4.7 Limitations for estimating Q_H

To estimate sensible heat advection, Q_H, over the distribution of snow patches near the measurement site, we used an equation fitted to measurements from just 30 minutes on 17 May. We then used this fitted equation to predict a distribution of sensible heat advection values on four separate days. We are cautious to not over-interpret the exact magnitudes of sensible heat advection calculated for the distributions of snow patch lengths (Figure 4.8 eiii–evi), and simply compare the distributions with the advection rates implied by non-zero, positive *Res*.

4.4.8 Energy balance uncertainties

Our energy balance equations (Equations 4.7 and 4.8) and our estimates of *Res* and Q_H, which loosely match on 16 and 17 May, suggest that the observed energy residual is due to horizontal heat advection. However, our methods have some limitations, primarily uncertainty in our estimates of the energy flux terms in Equation 4.8. Here, we discuss potential sources of uncertainty in our estimates of H_u, E_u, E_{melt}, and R_{net}.

First, we believe it is possible that we may be underestimating H_u and E_u. As discussed in Section 4.3.3, the two terms should represent heat fluxes over bare ground. However, we used ECs to estimate the two terms and, during the patchy snow period, the EC instrument integrates fluxes over both snow and bare ground (as illustrated in Figure 4.3b). H_u and E_u should be larger over bare ground than snow, because the bare ground surface is warmer than the snow surface (Figure 4.10a) and, considering that both the snow and bare ground surface are near saturation during our study period (Figure 4.4a, note the saturated muddy

surface), the air adjacent to the bare ground surface has a higher humidity than over snow. This means that our EC measurements of H_u and E_u may be underestimates. To examine this possibility, we used a bulk aerodynamic method to estimate H_u [*Cox et al.*, in review] using measured bare ground surface temperatures (Figure 4.10a). We also attempted to use the bulk aerodynamic method to estimate E_u, but found the method produced erroneously large E_u estimates, and we did not attempt to further constrain the uncertainty of E_u. Our model estimates of H_u were, at most, 50 W m^{-2} greater than measured H_u (not shown) This would lead to an overestimate of *Res* by, at most, 50 W m^{-2}.

Second, we considered uncertainty in our estimates of E_{melt}, Our primary source of uncertainty for E_{melt} is our assumed constant snow density of 400 kg m^{-3} (Section 4.3.3). We took this snow density from the literature, however, measurements at Kettle Ponds suggest that snow density during the melt season may approach 500 kg m^{-3} [*Lundquist et al.*, 2024]. Using the 500 kg m^{-3} snow density would increase our E_{melt} estimates by 25%, which would increase *Res* between 82–154 W m^{-2} on 14–17 May (Table 4.1). However, our comparisons of lidar-based and snow-pillow-based melt rates show that the lidar-based melt rates are relatively high — which, if anything, suggests that our density estimates are too high. Therefore, we consider the increases in *Res* described above as an upper limit on the uncertainty due to snow density, and we may be underestimating the magnitude of *Res* and heat advection.

Third, we considered potential uncertainties in our estimates of R_{net}, which probably stem from the two terms we estimated, LW_{out} and SW_{out}. To estimate LW_{out}, we assumed an emissivity of 0.98. *Raleigh et al.* [2013] suggested that snow emissivity rarely deviates from the range 0.97–1.0; thus, emissivity is only likely to affect our estimate of LW_{out} by 1–2 % (Equation 4.11). To estimate SW_{out}, we assumed a snow albedo of 0.6, which was the albedo over snow calculated by *Lundquist et al.* [2024] at our study site in early May. We recalculated our energy balance results using an albedo of 0.5, which reduced the daily mean *Res* on 15, 16, and 17 May from 98, 82, and 86 W m^{-2} (Figure 4.10b) to 64, 46, and 56 W m^{-2}, respectively, reductions of 35–44%. However, this decreased albedo also lead to larger, negative residuals before 14 May, when we expect heat advection and the energy balance

residual to be small. Therefore, an albedo of 0.5 is probably too small, although considering 0.5 as a lower limit, uncertainty in albedo could decrease estimates of *Res* by up to about 40%.

Overall, our observations support the hypothesis that sensible heat advection plays a role in contributing to snow melt, especially when considering that the three sources of uncertainty described above separately imply both over and underestimation of *Res*. If we assume no uncertainty in our measurements and that our energy balance contains all relevant energy fluxes, our estimate of the energy-balance residual is entirely attributable to sensible and latent advection (Equations 4.7 and 4.8). On three days with confirmed fSCA below 50%, 15–17 May, the peak mid-day *Res* ranged from 350–434 and the peak mid-day R_{net} ranged from 422–507 W m^{-2} (Figure 4.10c). This suggests that during patchy snow, horizontal heat advection contributes a similar amount of energy to snow melt as radiation.

4.5 Conclusions

We investigated sensible heat advection and snow melt over patchy snow using a combination of high resolution measurements, including an infrared video camera, two scanning lidars, 3-meter resolution satellite imagery, and a suite of tower-based meteorological instruments. Measured sensible heat advection near the upwind edge of a snow patch deviated from, and was lower than, flux rates predicted by theory, perhaps due to the shape of the snow patch, which rose about 20 cm above the ground surface. Additionally, our measurements of sensible heat advection decays linearly with distance into the snow patch, while theory predicts an exponential decay. Future studies should replicate our methods over a wider snow patch to examine how advection decays.

We estimated snow melt across six transects on two separate, ∼30-meter wide snow patches using scanning lidar. We found that snow melt rates were higher at the windward snow patch edge, and lower at the leeward edge, suggesting that horizontal heat advection increased snow melt rates. These findings are consistent with previous observations of snow patch melt; however, in contrast to other studies, melt rates over our patches decayed slowly

with distance from the windward edge, and below-average melt rates were isolated to the very leeward edge of the patch. We compared spatially-averaged lidar snow melt estimates with measurements from four fluidless snow pillows, and found that all instruments were in reasonable agreement. Leveraging the lidars allowed us to measure snow melt rates over disconnected snow patches in topographic concavities, while snow above the snow pillows melted out earlier, in part because the snow pillows must be installed on level ground where snow melts earlier.

We generated snow covered area (fSCA) maps from 3-meter satellite imagery, which illustrated the increasing patchiness of snow at the site during the melt season. We used the lidar-based snow melt rates, estimates of net radiation, and eddy covariance measurements of turbulent heat fluxes to characterize the energy balance over a snow patch. We found that as fSCA decreased and patchiness increased, the energy balance residual became increasingly large. When fSCA dropped below 50%, the peak, mid-day energy balance residual ranged between 350–434 W m^{-2}, and the daily averaged residual ranged from 82–98 W m^{-2}. When fSCA was greater than 50%, the daily averaged residual ranged from -20–10 W m^{-2}.

Using measurements of sensible heat advection from 12:00–12:30 LT on a single day, we extrapolated to other mid-day periods and predicted the sensible heat advection over a distribution of snow patches observed in a 300x300 m^2 domain surrounding our measurement site, on four separate days. The estimates of sensible heat advection ranged from 193–481 W m^{-2}. On the same four days, the peak mid-day net radiation ranged from 330–507 W m^{-2} and the peak mid-day energy balance residual ranged from 181–434 W m^{-2}. Comparing the estimated sensible heat advection rates and the measured energy balance residual terms on four days, we found that sensible heat advection accounted for between 79 and 100% of the residual. These estimates suggest that sensible heat advection provided a snowmelt energy contribution on par with that of net radiation. When sensible heat advection did not account for the entire residual, we hypothesized that latent heat advection could be responsible for the remaining residual, and on such days, our measurements indicated that latent heat advection may reach up to about 93 W m^{-2}. On one patchy snow day, 13

May, we found that sensible and latent heat fluxes measured by the eddy covariance method were approximately zero, supporting the hypothesis that horizontal sensible and latent heat advection is important near our site, because zero EC fluxes would require that upward heat fluxes over bare ground are balanced by downward fluxes, at least within the footprint of the eddy covariance instrument.

Overall, our measurements strongly support the hypothesis that sensible heat advection is an important component of the surface energy balance for patchy, melting snow. At our site, significant horizontal heat advection occurred for 4—5 days, when fSCA fell below 50% and the final snow patches melted away. These findings underscore the need to account for heat advection in models used to predict timing and rates of snow melt. Additionally, our measurements highlight the need for additional field measurements of heat advection, particularly in complex terrain and in concave micro-topography where snow patches persist (e.g. Figure 4.7a). Our IR video camera field measurements of sensible heat advection deviated from an idealized advection model, with windward-edge advection rates lower than theory predicts, potentially due to the shape of the snow patch. Additionally, our lidar-based estimates of snow melt across snow patches revealed that melt rates vary across the snow patch, in ways that differ from previous studies. To reveal future insights about heat advection on the snow-patch scale, the IR video camera method used here and originally presented in *Haugeneder et al.* [2023] could be deployed over snow patches in variable topography, where advective fluxes are likely to deviate further from idealized models.

Acknowledgments

We would like to thank Elie Bou-Zeid, Michelle DiBenedetto, Alex Horner-Devine, and Dale Durran for discussions that deepened our understanding and led to this publication. We also thank the Rocky Mountain Biological Laboratory for their facilitation of the field site. This work was supported by National Science Foundation Awards 2139836 and 2139809 and U.S. Department of Energy Environmental Systems Science award DE-SC0024075. Planet imagery was retrieved through NASA awards 80NSSC21K1151 and 80NSSC24K0050. This

material is based upon work supported by the NSF National Center for Atmospheric Research, which is a major facility sponsored by the U.S. National Science Foundation under Cooperative Agreement No. 1852977.

Data availability

Eddy covariance, surface meteorological measurements, and web-camera images from the Kettle Ponds site were collected as part of the Sublimation of Snow (SOS) campaign [*Lundquist et al.*, 2024] and can be downloaded at the DOI link in this citation: *NSF NCAR/EOL ISFS Team* [2024]. Infrared video camera and lidar data are available upon request but are not publicly hosted due to their large volume. Planet imagery and the derived snow cover area maps are not available for distribution.

Chapter 5

CONCLUSIONS

5.1 Summary

In this dissertation, we examined turbulent and advective transport phenomena that influence the exchange of water vapor, heat, momentum, and energy near the earth's surface in complex terrain. We used measurements across a range of scales, from eddy covariance point measurements of turbulent fluxes, to infrared video camera measurements of temperature across a 2x4 meter slice of the surface layer, to doppler lidar measurements of wind fields across a 2x2 kilometer cross section of the East River valley. This unique combination of observations collected by the concurrent SOS, SAIL, and SPLASH campaigns elucidated hydrometeorological processes in great detail.

In Chapter 2 we measured sublimation rates throughout the 2022-2023 winter season in the East River Valley and found that winter sublimation accounted for approximately 10% of the seasonal maximum snowpack. We observed positive water vapor flux divergence in the surface layer during blowing snow conditions, because blowing snow suspended in the air sublimates, adding water vapor to the atmosphere. During one blowing snow event, 10-meter ECs measured more than 4x as much sublimation as the 2-meter EC. Over the entire season, the 10-meter EC measured 12% more sublimation. During non-blowing snow conditions, we observed negative water vapor flux divergence, with ECs above 10 meters measuring 36–41% less sublimation than ECs at standard measurement heights of 2–3 meters. During downvalley winds, we observed mean downward air motion at the site, which induces vertical advection of water vapor and explains the negative water vapor flux divergence. We did not explain the negative divergence during other wind conditions.

In Chapter 3 we measured near surface turbulence at three sites and valley-scale turbu-

lence using a doppler lidar. We found that shear-layers produced at and below ridge-height due to wind blocking by terrain and wind turning, respectively, produced increased turbulent energy, which transports down to the valley floor, resulting in increased near surface mixing rates. Simultaneously, we observed downdrafts that carried dry air from high above the surface down to the valley-floor, which increased near-surface sublimation rates. We also observed specific sub-mesoscale flow phenomena, lee-rotors and sub-rotor vortices, that formed in the lee of an upwind ridge and were associated with especially large spikes in near-surface mixing. During cross-valley synoptic winds, when elevated shear layers formed, models underpredicted fluxes because their underlying theories do not account for the effects of sub-mesoscale motions.

In Chapter 4, we used an infrared measurement technique to calibrate an equation for estimating sensible heat flux into an isolated snow patch. We also used three-meter satellite imagery, scanning lidar, radiometers, and eddy covariance systems to track snow melt and the surface energy balance over a snow patch. We found that when snow covered area fell below approximately 50%, lateral sensible heat advection was responsible for approximately 50% of the energy going towards snow melt, for at least three days during the melt season in the East River Valley.

In summary, we used a suite of instrumentation across a range of scales to constrain total seasonal sublimation, to explain when and how sub-mesoscale flows influence near-surface fluxes of water vapor, heat, and momentum; and to understand the importance of sensible heat advection for the melt of patchy snow.

5.2 Broader Impacts

Each of the scientific advancements outlined in Chapters 2–4 has implications for future scientific research or water resource management.

In Chapter 2, we constrained total sublimation in a headwater catchment of the Colorado River, and contributed to the conversation about what could be causing decreasing streamflow efficiency in the Colorado River basin. In 2021, the snowpack in the basin was 80%

of the historical average, but spring streamflow was 25%. Some have attributed declining streamflows to increasing sublimation rates [*Xiao et al.*, 2018], a plausible explanation considering some models estimate that sublimation removes 20–40% of the seasonal snowpack [*Abatzoglou et al.*, 2021]. Our observations indicate sublimation is a less important part of the water balance than models would suggest. Additionally, our work in Chapter 2 examined sublimation measurements made by 12 vertically and horizontally distributed eddy covariance systems. This deployment represents a rare opportunity to compare eddy covariance measurements in complex terrain. We found that over short periods, sublimation rates can vary significantly across instrument heights. We suggest that future field campaigns consider the depth of the blowing snow layer before choosing a height to deploy an eddy covariance system. We conclude that a single EC instrument near the top of the blowing snow layer, 10 meters at our measurement site, is sufficient to measure sublimation as long as the instrument is deployed for the entire winter season.

In Chapter 3, we observed atmospheric turbulence in complex terrain using a suite of instruments that are rarely deployed in unison. The combined surface and scanning Doppler wind lidar measurements provided a unique look at the turbulent kinetic energy (TKE) budget in the mountain atmosphere. The observations demonstrated that TKE transport can play a major role in the near-surface turbulence budget, as previous researchers have hypothesized [*Litt et al.*, 2017]. The possibility of TKE transport also helps explain when and why Monin-Obukhov similarity theory (MOST) fails in complex terrain. When synoptic winds were oriented perpendicular to ridges, TKE was transported from above the valley floor to the valley floor, near-surface mixing was elevated, and MOST underestimated surface fluxes. Previous research has suggested parameterizing increased mixing in complex terrain by simply increasing the roughness length parameter used in surface flux models (e.g. an "effective roughness length") [*Rotach et al.*, 2015]. Our research suggests that such an approach would need to consider the relative orientation of synoptic winds and topography. Our observations of mixing across the valley atmosphere also identified downdrafts that traveled from elevated shear layers to the valley floor. These downdrafts, and their apparent ability to

carry dry upper-atmosphere air down into the valley, resembles the ability of convective cells to carry near-surface air rapidly upward (updrafts). We propose that one potential path for improving estimates of surface fluxes in complex terrain could involve modifying the Eddy-Diffusivity/Mass-Flux model [*Soares et al.*, 2004], which was designed to model updrafts, to model downdrafts.

In Chapter 4, we combined energy balance measurements from a single site with snow melt observations on two distinct snow patches and satellite. We concluded that in a Colorado River headwater catchment, sensible heat advection can considerably accelerate snow melt — by up to two times — and should be parameterized in land surface and snowpack models [e.g. *Harder et al.*, 2019].

5.3 Open Questions

Our findings in Chapter 2 suggested that during horizontally-homogenous snow cover, vertical and lateral advection of water vapor may influence the accuracy of EC measurements of sublimation. However, the conditions under which EC measurements during horizontally-homogenous snow cover are significantly affected by the advection processes during remains unclear. We do not know what processes caused the mean downward motion observed at Kettle Ponds. Future studies could potentially answer this question by examining valley-scale circulations, either with the measurements available from the three field campaigns, or with large eddy simulations [e.g. *Weigel et al.*, 2007]. Additionally, we do not know the magnitude of lateral water vapor advection. Future studies may have to rely on large eddy simulations or novel measurement techniques to estimate lateral water vapor advection on the valley-scale. Presently, studies that have successfully measured lateral water vapor advection have used tubes to carry air from different lateral locations to a single gas analyzer, a method that may not work to measure valley-scale advection. One possible way to measure valley-scale horizontal gradients could be deploying multiple, horizontally distributed tethered balloons, which can measure tall, high-resolution vertical profiles of temperature and humidity without the height restrictions associated with setting up a tower. Another solu-

tion could be to use multiple unmanned aerial vehicles (drones) to simultaneously measure vertical profiles at different points in the complex terrain. Additionally, while our extensive measurements at the Kettle Ponds site suggest that only 10% of the seasonal snowpack is lost to sublimation, these estimates pertain to only one, unvegetated valley-floor site. Previous studies have demonstrated that nearly all other locations in a headwater catchment — steeper slopes, ridges, and forested valley floors — have higher sublimation rates [*Strasser et al.*, 2008]. Future studies should deploy vertically distributed EC systems in other areas of headwater catchments to better constrain sublimation rates in the upper Colorado River basin, and to understand how vertical flux divergence may affect sublimation estimates above other land cover types.

In Chapter 3, we observed increased turbulent mixing on the valley floor, the production of turbulence within elevated shear layers above the valley floor, and the formation of lee-rotors and sub-rotor vortices behind a windward ridge. While our observations suggest the elevated shear layers resulted in the transport of TKE towards the valley floor, it is not clear if lee-rotors and/or sub-rotor vortices are a requirement for downward transport. Additionally, it remains unclear exactly how TKE is transported downwards (turbulent versus mean advective transport of TKE), how often such transport events occur, or how much those transport events are responsible for increased near-surface mixing. Future work will have to answer these questions if they hope to implement improved parameterizations for surface fluxes that incorporate non-local exchange across large distances. Large eddy simulation is a promising method for further investigating these phenomena [e.g. *Weigel and Rotach*, 2004; *Weigel et al.*, 2006].

In Chapter 4, we found that sensible heat advection contributed to the accelerated melt out of snow patches. However, previous studies have found the stable boundary layer over snow patches can decouple, thereby protecting snow from sensible heat advection [*Mott et al.*, 2011, 2013]. While we did not observe decoupling, our direct measurements of sensible heat advection were limited to one 30-minute period. These differences highlight that the influence of advection may vary significantly across different alpine environments. Future studies

should try to implement the same techniques we used to measure sensible heat advection over larger snow patches that may decouple. Additionally, the importance of sensible heat advection at larger scales also remains unclear. While we found that sensible heat advection was important for snow melt over one week at a single study plot, other studies found that the effects of advection do not have a large impact on the water shed scale [*Harder et al.*, 2019]. Future studies should incorporate advection into distributed snow hydrology models [e.g. *Harder et al.*, 2019] to elucidate if advective heat transport matters in some environments more than others.

5.4 Final Thoughts

We found, like previous researchers, that fluxes in complex terrain are, well, complex. On the applied side of things, we found that the height of a deployed eddy covariance instrument can significantly modify estimates of surface water vapor fluxes. This fact should be noted by future measurement campaigns. Additionally, we found that bulk solutions for sensible heat advection provide a promising path for predicting patchy snow melt. Future researchers attempting to improve snow melt models should therefore consider the model of *Harder et al.* [2019]. On the theoretical side, we identified that non-local transport can significantly impact surface water vapor fluxes. In Chapter 1, we saw that vertical advection at the site-scale carried dry air to the surface, and in Chapter 2, we observed large eddies carrying dry air from high above the valley down to the surface. Parameterizing non-local transport should therefore be a priority for those seeking to improve surface flux parameterizations in complex terrain, though doing so remains one of the great challenges in boundary layer meteorology [*LeMone et al.*, 2019].

We hope that this work highlights the value of coordinated, multi-scale observations, and reminds us that progress in understanding complex systems requires complex observations. We also hope that observations collected by the SOS, SPLASH, and SAIL campaigns will continue to yield scientific insight for decades to come. However, we should not consider the observational work done. Despite the historic deployment represented by the three

campaigns, the atmosphere above the East River Valley remained inevitably under-sampled. To improve weather models and our understanding of the water cycle, we must continue to pursue intensive observational campaigns.

This dissertation sought to unravel how water vapor, heat, and momentum are exchanged near the earth's surface in complex terrain. Though motivated by questions about water resources, this research involved meteorology, fluid physics, and snow science. This work is a reminder that the distinctions we imagine between scientific disciplines are, indeed, imaginary.

BIBLIOGRAPHY

Abatzoglou, J., A. Rallings, L. Bernacci, J. Viers, and J. Medellín-Azuara, California's missing forecast flows in spring 2021 – challenges for seasonal flow forecasting, 2021.

Adler, B., et al., Impact of Seasonal Snow-Cover Change on the Observed and Simulated State of the Atmospheric Boundary Layer in a High-Altitude Mountain Valley, *Journal of Geophysical Research: Atmospheres*, *128*(12), e2023JD038,497, doi:10.1029/2023JD038497, 2023.

Adler, B., et al., The Short Life of Upvalley Wind in a High-Altitude Valley in the Colorado Rocky Mountains, *Journal of Geophysical Research: Atmospheres*, *130*(11), e2025JD043,455, doi:10.1029/2025JD043455, 2025.

Aksamit, N. O., and J. W. Pomeroy, Near-surface snow particle dynamics from particle tracking velocimetry and turbulence measurements during alpine blowing snow storms, *The Cryosphere*, *10*(6), 3043–3062, doi:10.5194/tc-10-3043-2016, 2016.

Aksamit, N. O., and J. W. Pomeroy, The Effect of Coherent Structures in the Atmospheric Surface Layer on Blowing-Snow Transport, *Boundary-Layer Meteorology*, doi:10.1007/s10546-017-0318-2, 2017.

Aksamit, N. O., and J. W. Pomeroy, Scale Interactions in Turbulence for Mountain Blowing Snow, *Journal of Hydrometeorology*, *19*(2), 305–320, doi:10.1175/JHM-D-17-0179.1, 2018.

Alduchov, O. A., and R. E. Eskridge, Improved Magnus Form Approximation of Saturation Vapor Pressure, *Journal of Applied Meteorology*, *35*(4), 601–609, doi:10.1175/1520-0450(1996)035⟨0601:IMFAOS⟩2.0.CO;2, 1996.

Andreas, E. L., A theory for the scalar roughness and the scalar transfer coefficients over snow and sea ice, *Boundary-Layer Meteorology*, *38*(1-2), 159–184, doi:10.1007/BF00121562, 1987.

Andreas, E. L., R. E. Jordan, and A. P. Makshtas, Simulations of Snow, Ice, and Near-Surface Atmospheric Processes on Ice Station Weddell, *Journal of Hydrometeorology*, *5*(4), 611–624, doi:10.1175/1525-7541(2004)005⟨0611:SOSIAN⟩2.0.CO;2, 2004.

Andreas, E. L., P. O. G. Persson, A. A. Grachev, R. E. Jordan, T. W. Horst, P. S. Guest, and C. W. Fairall, Parameterizing Turbulent Exchange over Sea Ice in Winter, *Journal of Hydrometeorology*, *11*(1), 87–104, doi:10.1175/2009JHM1102.1, 2010.

Babić, N., B. Adler, A. Gohm, N. Kalthoff, M. Haid, M. Lehner, P. Ladstätter, and M. W. Rotach, Cross-valley vortices in the Inn valley, Austria: Structure, evolution and governing force imbalances, *Quarterly Journal of the Royal Meteorological Society*, *147*(740), 3835–3861, doi:10.1002/qj.4159, 2021.

Babić, N., B. Adler, A. Gohm, M. Lehner, and N. Kalthoff, Exploring the daytime boundary layer evolution based on Doppler spectrum width from multiple coplanar wind lidars during CROSSINN, *Weather and Climate Dynamics*, *5*(2), 609–631, doi:10.5194/wcd-5-609-2024, 2024.

Bell, T. M., P. Klein, N. Wildmann, and R. Menke, Analysis of flow in complex terrain using multi-Doppler lidar retrievals, *Atmospheric Measurement Techniques*, *13*(3), 1357–1371, doi:10.5194/amt-13-1357-2020, 2020.

Bhatnagar, P. L., E. P. Gross, and M. Krook, A Model for Collision Processes in Gases. I. Small Amplitude Processes in Charged and Neutral One-Component Systems, *Physical Review*, *94*(3), 511–525, doi:10.1103/PhysRev.94.511, 1954.

Boer, G. D., et al., Supporting Advancement in Weather and Water Prediction in the Upper

Colorado River Basin: The SPLASH Campaign, *Bulletin of the American Meteorological Society*, doi:10.1175/BAMS-D-22-0147.1, 2023.

Brutsaert, W., *Evaporation into the Atmosphere*, Springer Netherlands, Dordrecht, doi:10.1007/978-94-017-1497-6, 1982.

Chen, S., and G. D. Doolen, LATTICE BOLTZMANN METHOD FOR FLUID FLOWS, *Annual Review of Fluid Mechanics*, *30*(1), 329–364, doi:10.1146/annurev.fluid.30.1.329, 1998.

Chiu, I., S. Pestana, K. Yang, E. T. Boudreau, L. Setiawan, J. Pflug, and N. Cristea, PlanetSCA: A Python package implementing snow-covered area mapping PlanetScope imagery with machine learning, doi:10.5281/ZENODO.17380192, 2025.

Christensen, N. S., A. W. Wood, N. Voisin, D. P. Lettenmaier, and R. N. Palmer, The Effects of Climate Change on the Hydrology and Water Resources of the Colorado River Basin, *Climatic Change*, *62*(1-3), 337–363, doi:10.1023/B:CLIM.0000013684.13621.1f, 2004.

Chritin, V., R. Bolognesi, and H. Gubler, FlowCapt: A new acoustic sensor to measure snow-drift and wind velocity for avalanche forecasting, *Cold Regions Science and Technology*, *30*(1-3), 125–133, doi:10.1016/S0165-232X(99)00012-9, 1999.

Claussen, M., Local advection processes in the surface layer of the marginal ice zone, *Boundary-Layer Meteorology*, *54*(1-2), 1–27, doi:10.1007/BF00119409, 1991.

Cox, C., M. Gallagher, J. Intrieri, B. Butterworth, T. Meyers, and O. Persson, Atmospheric Surface Flux Station #50 measurements (level 2 Processed), Study of Precipitation, the Lower Atmosphere and Surface for Hydrometeorology (SPLASH), October 2021-June 2023, doi:10.5281/ZENODO.10313363, 2025a.

Cox, C. J., B. Adler, B. J. Butterworth, and E. Schwat, Processes modulating snowpack sublimation after peak storage in the East River Valley of Colorado: Application of surface renewal theory, doi:10.22541/essoar.174742839.97375040/v1, in review.

Cox, C. J., et al., Observations of surface energy fluxes and meteorology in the seasonally snow-covered high-elevation East River watershed during SPLASH, 2021–2023, *Earth System Science Data*, *17*(4), 1481–1499, doi:10.5194/essd-17-1481-2025, 2025b.

Déry, S. J., and M. K. Yau, Large-scale mass balance effects of blowing snow and surface sublimation, *Journal of Geophysical Research: Atmospheres*, *107*(D23), doi:10.1029/2001JD001251, 2002.

Doyle, J. D., and D. R. Durran, Rotor and Subrotor Dynamics in the Lee of Three-Dimensional Terrain, *Journal of the Atmospheric Sciences*, *64*(12), 4202–4221, doi:10.1175/2007JAS2352.1, 2007.

Doyle, J. D., V. Grubišić, W. O. J. Brown, S. F. J. De Wekker, A. Dörnbrack, Q. Jiang, S. D. Mayor, and M. Weissmann, Observations and Numerical Simulations of Subrotor Vortices during T-REX, *Journal of the Atmospheric Sciences*, *66*(5), 1229–1249, doi:10.1175/2008JAS2933.1, 2009.

Essery, R., R. Granger, and J. Pomeroy, Boundary-layer growth and advection of heat over snow and soil patches: Modelling and parameterization, *Hydrological Processes*, *20*(4), 953–967, doi:10.1002/hyp.6122, 2006.

Falge, E., et al., Gap filling strategies for long term energy flux data sets, *Agricultural and Forest Meteorology*, *107*(1), 71–77, doi:10.1016/S0168-1923(00)00235-5, 2001.

Farina, S., and D. Zardi, Understanding Thermally Driven Slope Winds: Recent Advances and Open Questions, *Boundary-Layer Meteorology*, *189*(1-3), 5–52, doi:10.1007/s10546-023-00821-1, 2023.

Feldman, D., et al., The Surface Atmosphere Integrated Field Laboratory (SAIL) Campaign, *Bulletin of the American Meteorological Society*, doi:10.1175/BAMS-D-22-0049.1, 2023.

Finnigan, J., A comment on the paper by Lee (1998): "On micrometeorological observations of surface-air exchange over tall vegetation", *Agricultural and Forest Meteorology*, *97*(1), 55–64, doi:10.1016/S0168-1923(99)00049-0, 1999.

Foken, T., 50 Years of the Monin–Obukhov Similarity Theory, *Boundary-Layer Meteorology*, *119*(3), 431–447, doi:10.1007/s10546-006-9048-6, 2006.

Foken, T., F. Wimmer, M. Mauder, C. Thomas, and C. Liebethal, Some aspects of the energy balance closure problem, *Atmospheric Chemistry and Physics*, *6*(12), 4395–4402, doi:10.5194/acp-6-4395-2006, 2006.

Foken, T., M. Aubinet, J. J. Finnigan, M. Y. Leclerc, M. Mauder, and K. T. Paw U, Results Of A Panel Discussion About The Energy Balance Closure Correction For Trace Gases, *Bulletin of the American Meteorological Society*, *92*(4), ES13–ES18, doi:10.1175/2011BAMS3130.1, 2011.

Foken, Th., and B. Wichura, Tools for quality assessment of surface-based flux measurements, *Agricultural and Forest Meteorology*, *78*(1-2), 83–105, doi:10.1016/0168-1923(95)02248-1, 1996.

Fujita, K., K. Hiyama, H. Iida, and Y. Ageta, Self-regulated fluctuations in the ablation of a snow patch over four decades, *Water Resources Research*, *46*(11), 2009WR008,383, doi:10.1029/2009WR008383, 2010.

Gordon, M., and P. A. Taylor, Measurements of blowing snow, Part I: Particle shape, size distribution, velocity, and number flux at Churchill, Manitoba, Canada, *Cold Regions Science and Technology*, *55*(1), 63–74, doi:10.1016/j.coldregions.2008.05.001, 2009.

Grachev, A. A., C. W. Fairall, P. O. G. Persson, E. L. Andreas, and P. S. Guest, Stable Boundary-Layer Scaling Regimes: The Sheba Data, *Boundary-Layer Meteorology*, *116*(2), 201–235, doi:10.1007/s10546-004-2729-0, 2005.

Grachev, A. A., L. S. Leo, S. D. Sabatino, H. J. S. Fernando, E. R. Pardyjak, and C. W. Fairall, Structure of Turbulence in Katabatic Flows Below and Above the Wind-Speed Maximum, *Boundary-Layer Meteorology*, *159*(3), 469–494, doi:10.1007/s10546-015-0034-8, 2016.

Granger, R. J., J. W. Pomeroy, and J. Parviainen, Boundary-layer integration approach to advection of sensible heat to a patchy snow cover, *Hydrological Processes*, *16*(18), 3559–3569, doi:10.1002/hyp.1227, 2002.

Granger, R. J., R. Essery, and J. W. Pomeroy, Boundary-layer growth over snow and soil patches: Field observations, *Hydrological Processes*, *20*(4), 943–951, doi:10.1002/hyp.6123, 2006.

Groot Zwaaftink, C. D., R. Mott, and M. Lehning, Seasonal simulation of drifting snow sublimation in Alpine terrain, *Water Resources Research*, *49*(3), 1581–1590, doi:10.1002/wrcr.20137, 2013.

Harder, P., J. W. Pomeroy, and W. Helgason, Local-Scale Advection of Sensible and Latent Heat During Snowmelt, *Geophysical Research Letters*, *44*, doi:10.1002/2017GL074394., 2017.

Harder, P., J. W. Pomeroy, and W. D. Helgason, A simple model for local-scale sensible and latent heat advection contributions to snowmelt, *Hydrology and Earth System Sciences*, *23*(1), 1–17, doi:10.5194/hess-23-1-2019, 2019.

Haugeneder, M., M. Lehning, D. Reynolds, T. Jonas, and R. Mott, A Novel Method to Quantify Near-Surface Boundary-Layer Dynamics at Ultra-High Spatio-Temporal Resolution, *Boundary-Layer Meteorology*, *186*(2), 177–197, doi:10.1007/s10546-022-00752-3, 2023.

Haugeneder, M., M. Lehning, I. Stiperski, D. Reynolds, and R. Mott, Turbulence in the Strongly Heterogeneous Near-Surface Boundary Layer over Patchy Snow, *Boundary-Layer Meteorology*, *190*(2), 7, doi:10.1007/s10546-023-00856-4, 2024.

Helgason, W., and J. Pomeroy, Problems Closing the Energy Balance over a Homogeneous Snow Cover during Midwinter, *Journal of Hydrometeorology*, *13*(2), 557–572, doi:10.1175/JHM-D-11-0135.1, 2012.

Hertenstein, R. F., and J. P. Kuettner, Rotor types associated with steep lee topography: Influence of the wind profile, *Tellus A: Dynamic Meteorology and Oceanography*, *57*(2), 117, doi:10.3402/tellusa.v57i2.14625, 2005.

Hogan, D., and J. D. Lundquist, Recent Upper Colorado River Streamflow Declines Driven by Loss of Spring Precipitation, *Geophysical Research Letters*, *51*(16), doi:10.1029/2024GL109826, 2024.

Hogan, D., E. Schwat, J. Lundquist, E. Gutmann, and J. Vano, SOS: Weather Blog. Version 1.0, doi:10.26023/E1WQ-JRNX-8205, 2023.

Howell, J. F., and L. Mahrt, Multiresolution Flux Decomposition, *Boundary-Layer Meteorology*, *83*(1), 117–137, doi:10.1023/A:1000210427798, 1997.

Jackson, S. I., and T. D. Prowse, Spatial variation of snowmelt and sublimation in a high-elevation semi-desert basin of western Canada, *Hydrological Processes*, *23*(18), 2611–2627, doi:10.1002/hyp.7320, 2009.

Kaimal, J. C., and J. J. Finnigan, *Atmospheric Boundary Layer Flows: Their Structure and Measurement*, Oxford University Press, Oxford University Press, New York, New York, doi:10.1093/oso/9780195062397.001.0001, 1994.

Keeler, E., K. Burk, and J. Kyrouac, Balloon-borne sounding system (BBSS), WNPN output data, doi:10.5439/1595321, 2022a.

Keeler, E., K. Burk, and J. Kyrouac, Balloon-borne sounding system (BBSS), WNPN output data, doi:10.5439/1595321, 2022b.

Kochendorfer, J., and K. T. Paw U, Field estimates of scalar advection across a canopy edge, *Agricultural and Forest Meteorology*, *151*(5), 585–594, doi:10.1016/j.agrformet.2011.01.003, 2011.

Kötsche, A., M. Maahn, V. Ettrichrätz, and H. Kalesse-Los, Snow microphysical processes in orographic turbulence revealed by cloud radar and in situ snowfall camera observations, doi:10.5194/egusphere-2025-4517, 2025.

Lapo, K., B. Nijssen, and J. D. Lundquist, Evaluation of Turbulence Stability Schemes of Land Models for Stable Conditions, *Journal of Geophysical Research: Atmospheres*, *124*(6), 3072–3089, doi:10.1029/2018JD028970, 2019.

Lee, X., On micrometeorological observations of surface-air exchange over tall vegetation, *Agricultural and Forest Meteorology*, *91*(1-2), 39–49, doi:10.1016/S0168-1923(98)00071-9, 1998.

Lehner, M., C. D. Whiteman, S. W. Hoch, B. Adler, and N. Kalthoff, Flow Separation in the Lee of a Crater Rim, *Boundary-Layer Meteorology*, *173*(2), 263–287, doi:10.1007/s10546-019-00466-z, 2019.

LeMone, M. A., et al., 100 Years of Progress in Boundary Layer Meteorology, *Meteorological Monographs*, *59*, 9.1–9.85, doi:10.1175/AMSMONOGRAPHS-D-18-0013.1, 2019.

Liston, G., and M. Sturm, The role of winter sublimation in the Arctic moisture budget, *Hydrology Research*, *35*(4-5), 325–334, doi:10.2166/nh.2004.0024, 2004.

Liston, G. E., Local Advection of Momentum, Heat, and Moisture during the Melt of Patchy Snow Covers, *Journal of Applied Meteorology*, *34*(7), 1705–1715, doi:10.1175/1520-0450-34.7.1705, 1995.

Litt, M., J.-E. Sicart, W. D. Helgason, and P. Wagnon, Turbulence Characteristics in the Atmospheric Surface Layer for Different Wind Regimes over the Tropical Zongo Glacier

(Bolivia, $$16ˆ\circ $$ 16 ∘ S), *Boundary-Layer Meteorology*, *154*(3), 471–495, doi:10.1007/s10546-014-9975-6, 2015.

Litt, M., J.-E. Sicart, D. Six, P. Wagnon, and W. D. Helgason, Surface-layer turbulence, energy balance and links to atmospheric circulations over a mountain glacier in the French Alps, *The Cryosphere*, *11*(2), 971–987, doi:10.5194/tc-11-971-2017, 2017.

López-Moreno, J., S. Fassnacht, J. Heath, K. Musselman, J. Revuelto, J. Latron, E. Morán-Tejeda, and T. Jonas, Small scale spatial variability of snow density and depth over complex alpine terrain: Implications for estimating snow water equivalent, *Advances in Water Resources*, *55*, 40–52, doi:10.1016/j.advwatres.2012.08.010, 2013.

Lundquist, J. D., S. Dickerson-Lange, E. Gutmann, T. Jonas, C. Lumbrazo, and D. Reynolds, Snow interception modelling: Isolated observations have led to many land surface models lacking appropriate temperature sensitivities, *Hydrological Processes*, *35*(7), e14,274, doi:10.1002/hyp.14274, 2021.

Lundquist, J. D., et al., Sublimation of Snow, *Bulletin of the American Meteorological Society*, doi:10.1175/BAMS-D-23-0191.1, 2024.

Mahrt, L., and D. Vickers, Boundary-Layer Adjustment Over Small-Scale Changes of Surface Heat Flux, *Boundary-Layer Meteorology*, *116*(2), 313–330, doi:10.1007/s10546-004-1669-z, 2005.

Mahrt, L., C. K. Thomas, A. A. Grachev, and P. O. G. Persson, Near-Surface Vertical Flux Divergence in the Stable Boundary Layer, *Boundary-Layer Meteorology*, *169*(3), 373–393, doi:10.1007/s10546-018-0379-x, 2018.

Mahrt, L., E. Nilsson, A. Rutgersson, and H. Pettersson, Vertical Divergence of the Atmospheric Momentum Flux near the Sea Surface at a Coastal Site, *Journal of Physical Oceanography*, *51*(11), 3529–3537, doi:10.1175/JPO-D-21-0081.1, 2021.

Mauder, M., M. Cuntz, C. Drüe, A. Graf, C. Rebmann, H. P. Schmid, M. Schmidt, and R. Steinbrecher, A strategy for quality and uncertainty assessment of long-term eddy-covariance measurements, *Agricultural and Forest Meteorology*, *169*, 122–135, doi:10.1016/j.agrformet.2012.09.006, 2013.

Mauder, M., T. Foken, M. Aubinet, and A. Ibrom, Eddy-Covariance Measurements, in *Springer Handbook of Atmospheric Measurements*, edited by T. Foken, pp. 1473–1504, Springer International Publishing, Cham, doi:10.1007/978-3-030-52171-4_55, 2021.

Molotch, N. P., P. D. Blanken, M. W. Williams, A. A. Turnipseed, R. K. Monson, and S. A. Margulis, Estimating sublimation of intercepted and sub-canopy snow using eddy covariance systems, *Hydrological Processes*, *21*(12), 1567–1575, doi:10.1002/hyp.6719, 2007.

Monin, A. S., and A. M. Obukhov, Basic laws of turbulent mixing in the surface layer of the atmosphere, *Tr. Akad. Nauk SSSR Geophiz. Inst*, *24*(151), 163–187, 1954.

Morrison, T. J., M. Calaf, and E. R. Pardyjak, A full three-dimensional surface energy balance over a desert playa, *Quarterly Journal of the Royal Meteorological Society*, *149*(750), 102–114, doi:10.1002/qj.4397, 2023.

Mott, R., L. Egli, T. Grünewald, N. Dawes, C. Manes, M. Bavay, and M. Lehning, Micrometeorological processes driving snow ablation in an Alpine catchment, *The Cryosphere*, *5*(4), 1083–1098, doi:10.5194/tc-5-1083-2011, 2011.

Mott, R., C. Gromke, T. Grünewald, and M. Lehning, Relative importance of advective heat transport and boundary layer decoupling in the melt dynamics of a patchy snow cover, *Advances in Water Resources*, *55*, 88–97, doi:10.1016/j.advwatres.2012.03.001, 2013.

Mott, R., M. Daniels, and M. Lehning, Atmospheric Flow Development and Associated Changes in Turbulent Sensible Heat Flux over a Patchy Mountain Snow Cover, *Journal of Hydrometeorology*, *16*(3), 1315–1340, doi:10.1175/JHM-D-14-0036.1, 2015.

Mott, R., E. Paterna, S. Horender, P. Crivelli, and M. Lehning, Wind tunnel experiments: Cold-air pooling and atmospheric decoupling above a melting snow patch, *The Cryosphere*, *10*(1), 445–458, doi:10.5194/tc-10-445-2016, 2016.

Mott, R., S. Schlögl, L. Dirks, and M. Lehning, Impact of Extreme Land Surface Heterogeneity on Micrometeorology over Spring Snow Cover, *Journal of Hydrometeorology*, *18*(10), 2705–2722, doi:10.1175/JHM-D-17-0074.1, 2017.

Mott, R., V. Vionnet, and T. Grünewald, The Seasonal Snow Cover Dynamics: Review on Wind-Driven Coupling Processes, *Frontiers in Earth Science*, *6*, 197, doi:10.3389/feart.2018.00197, 2018.

Nakai, Y., T. Sakamoto, T. Terajima, K. Kitamura, and T. Shirai, The effect of canopy-snow on the energy balance above a coniferous forest, *Hydrological Processes*, *13*(14-15), 2371–2382, doi:10.1002/(SICI)1099-1085(199910)13:14/15⟨2371::AID-HYP871⟩3.0.CO;2-1, 1999.

Newsom, R., and R. Krishnamurthy, Doppler Lidar (DL) Instrument Handbook, *Tech. Rep. DOE/SC-ARM/TR-101, 1034640, PNNL-21141*, doi:10.2172/1034640, 2022.

Newsom, R., Y. Shi, and R. Krishnamurthy, Dlrhi, doi:10.5439/1046188, 2011.

Newsom, R. K., W. A. Brewer, J. M. Wilczak, D. E. Wolfe, S. P. Oncley, and J. K. Lundquist, Validating precision estimates in horizontal wind measurements from a Doppler lidar, *Atmospheric Measurement Techniques*, *10*(3), 1229–1240, doi:10.5194/amt-10-1229-2017, 2017.

NSF NCAR/EOL ISFS Team, SOS: ISFS Surface Meteorology and Flux Products. Version 1.1, doi:10.26023/CYK2-SR3N-880J, 2024.

Palm, S. P., Y. Yang, J. D. Spinhirne, and A. Marshak, Satellite remote sensing of blowing snow properties over Antarctica, *Journal of Geophysical Research*, *116*(D16), D16,123, doi:10.1029/2011JD015828, 2011.

Palm, S. P., Y. Yang, V. Kayetha, and J. P. Nicolas, Insight into the Thermodynamic Structure of Blowing-Snow Layers in Antarctica from Dropsonde and CALIPSO Measurements, *Journal of Applied Meteorology and Climatology*, *57*(12), 2733–2748, doi: 10.1175/JAMC-D-18-0082.1, 2018.

Paw U, K. T., D. D. Baldocchi, T. P. Meyers, and K. B. Wilson, Correction Of Eddy-Covariance Measurements Incorporating Both Advective Effects And Density Fluxes, *Boundary-Layer Meteorology*, *97*(3), 487–511, doi:10.1023/A:1002786702909, 2000.

PBC, P. L., Planet Application Program Interface: In Space for Life on Earth, 2020/2025.

Peltola, O., K. Lapo, and C. K. Thomas, A Physics-Based Universal Indicator for Vertical Decoupling and Mixing Across Canopies Architectures and Dynamic Stabilities, *Geophysical Research Letters*, *48*(5), e2020GL091,615, doi:10.1029/2020GL091615, 2021.

Pestana, S., C. C. Chickadel, A. Harpold, T. S. Kostadinov, H. Pai, S. Tyler, C. Webster, and J. D. Lundquist, Bias Correction of Airborne Thermal Infrared Observations Over Forests Using Melting Snow, *Water Resources Research*, *55*(12), 11,331–11,343, doi:10.1029/2019WR025699, 2019.

Pflug, J. M., and J. D. Lundquist, Inferring Distributed Snow Depth by Leveraging Snow Pattern Repeatability: Investigation Using 47 Lidar Observations in the Tuolumne Watershed, Sierra Nevada, California, *Water Resources Research*, *56*(9), e2020WR027,243, doi:10.1029/2020WR027243, 2020.

Pomeroy, J. W., and R. L. H. Essery, Turbulent fluxes during blowing snow: Field tests of model sublimation predictions, *Hydrological Processes*, *13*(18), 2963–2975, doi:10.1002/(SICI)1099-1085(19991230)13:18⟨2963::AID-HYP11⟩3.0.CO;2-9, 1999.

Pomeroy, J. W., and D. M. Gray, *Snowcover Accumulation, Relocation and Management*, no. 7 in National Hydrology Research Institute Science Report, National Hydrology Research Institute, Saskatoon, Saskatchewan, Canada, 1995.

Raleigh, M. S., C. C. Landry, M. Hayashi, W. L. Quinton, and J. D. Lundquist, Approximating snow surface temperature from standard temperature and humidity data: New possibilities for snow model and remote sensing evaluation, *Water Resources Research*, *49*(12), 8053–8069, doi:10.1002/2013WR013958, 2013.

Reba, M. L., J. Pomeroy, D. Marks, and T. E. Link, Estimating surface sublimation losses from snowpacks in a mountain catchment using eddy covariance and turbulent transfer calculations, *Hydrological Processes*, *26*(24), 3699–3711, doi:10.1002/hyp.8372, 2012.

Reba, M. L., D. Marks, T. E. Link, J. Pomeroy, and A. Winstral, Sensitivity of model parameterizations for simulated latent heat flux at the snow surface for complex mountain sites, *Hydrological Processes*, *28*(3), 868–881, doi:10.1002/hyp.9619, 2014.

Rotach, M. W., M. Andretta, P. Calanca, A. P. Weigel, and A. Weiss, Boundary layer characteristics and turbulent exchange mechanisms in highly complex terrain, *Acta Geophysica*, *56*(1), 194–219, doi:10.2478/s11600-007-0043-1, 2008.

Rotach, M. W., A. Gohm, M. N. Lang, D. Leukauf, I. Stiperski, and J. S. Wagner, On the Vertical Exchange of Heat, Mass, and Momentum Over Complex, Mountainous Terrain, *Frontiers in Earth Science*, *3*, doi:10.3389/feart.2015.00076, 2015.

Schirmer, M., V. Wirz, A. Clifton, and M. Lehning, Persistence in intra-annual snow depth distribution: 1. Measurements and topographic control, *Water Resources Research*, *47*(9), 2010WR009,426, doi:10.1029/2010WR009426, 2011.

Schmidli, J., Daytime Heat Transfer Processes over Mountainous Terrain, *Journal of the Atmospheric Sciences*, *70*(12), 4041–4066, doi:10.1175/JAS-D-13-083.1, 2013.

Schotanus, P., F. Nieuwstadt, and H. De Bruin, Temperature measurement with a sonic anemometer and its application to heat and moisture fluxes, *Boundary-Layer Meteorology*, *26*(1), 81–93, doi:10.1007/BF00164332, 1983.

Schwat, E., D. Hogan, K. T. Paw U, C. J. Cox, B. J. Butterworth, E. Gutmann, J. A. Vano, and J. D. Lundquist, Estimating snow sublimation in complex terrain: A season of intensive field measurements and the role of vertical water vapor flux divergence, *Journal of Hydrometeorology*, doi:10.1175/JHM-D-25-0022.1, 2025.

Serafin, S., et al., Exchange Processes in the Atmospheric Boundary Layer Over Mountainous Terrain, *Atmosphere*, *9*(3), 102, doi:10.3390/atmos9030102, 2018.

Sexstone, G. A., D. W. Clow, D. I. Stannard, and S. R. Fassnacht, Comparison of methods for quantifying surface sublimation over seasonally snow-covered terrain: Comparison of Methods for Quantifying Surface Snow Sublimation, *Hydrological Processes*, *30*(19), 3373–3389, doi:10.1002/hyp.10864, 2016.

Sexstone, G. A., D. W. Clow, S. R. Fassnacht, G. E. Liston, C. A. Hiemstra, J. F. Knowles, and C. A. Penn, Snow Sublimation in Mountain Environments and Its Sensitivity to Forest Disturbance and Climate Warming, *Water Resources Research*, *54*(2), 1191–1211, doi:10.1002/2017WR021172, 2018.

Shippert, T., R. Newsom, L. Riihimaki, and D. Zhang, Dlprofwstats4news.c1, doi:10.5439/1178583, 2010.

Shippert, T., R. Newsom, L. Riihimaki, and D. Zhang, Dlprofwind4news.c1, doi:10.5439/1178582, 2022.

Sigmund, A., J. Dujardin, F. Comola, V. Sharma, H. Huwald, D. B. Melo, N. Hirasawa, K. Nishimura, and M. Lehning, Evidence of Strong Flux Underestimation by Bulk Parametrizations During Drifting and Blowing Snow, *Boundary-Layer Meteorology*, *182*(1), 119–146, doi:10.1007/s10546-021-00653-x, 2022.

Singh, D. K., S. W. Hoch, I. Gultepe, and E. R. Pardyjak, A case study of the life cycle of a stratus-lowering coastal-fog event in Newfoundland, Canada, *Quarterly Journal of the Royal Meteorological Society*, *150*(759), 641–662, doi:10.1002/qj.4615, 2024.

Slater, A. G., et al., The Representation of Snow in Land Surface Schemes: Results from PILPS 2(d), *Journal of Hydrometeorology*, *2*(1), 7–25, doi:10.1175/1525-7541(2001)002⟨0007:TROSIL⟩2.0.CO;2, 2001.

Soares, P. M. M., P. M. A. Miranda, A. P. Siebesma, and J. Teixeira, An eddy-diffusivity/mass-flux parametrization for dry and shallow cumulus convection, *Quarterly Journal of the Royal Meteorological Society*, *130*(604), 3365–3383, doi:10.1256/qj.03.223, 2004.

Sorteberg, H., R. Engeset, and H. Udnæs, A national network for snow monitoring in Norway: Snow pillow verification using observations and models, *Physics and Chemistry of the Earth, Part C: Solar, Terrestrial & Planetary Science*, *26*(10-12), 723–729, doi:10.1016/S1464-1917(01)95016-0, 2001.

Stiperski, I., and M. Calaf, Generalizing Monin-Obukhov Similarity Theory (1954) for Complex Atmospheric Turbulence, *Physical Review Letters*, *130*(12), 124,001, doi:10.1103/PhysRevLett.130.124001, 2023.

Stiperski, I., and M. W. Rotach, On the Measurement of Turbulence Over Complex Mountainous Terrain, *Boundary-Layer Meteorology*, *159*(1), 97–121, doi:10.1007/s10546-015-0103-z, 2016.

Stiperski, I., M. Calaf, and M. W. Rotach, Scaling, Anisotropy, and Complexity in Near-Surface Atmospheric Turbulence, *Journal of Geophysical Research: Atmospheres*, *124*(3), 1428–1448, doi:10.1029/2018JD029383, 2019.

Strasser, U., M. Bernhardt, M. Weber, G. E. Liston, and W. Mauser, Is snow sublimation important in the alpine water balance?, *The Cryosphere*, *2*(1), 53–66, doi:10.5194/tc-2-53-2008, 2008.

Strauss, L., S. Serafin, S. Haimov, and V. Grubišić, Turbulence in breaking mountain waves and atmospheric rotors estimated from airborne *in situ* and Doppler radar measurements,

Quarterly Journal of the Royal Meteorological Society, *141*(693), 3207–3225, doi:10.1002/qj.2604, 2015.

Stull, R. B., *An Introduction to Boundary Layer Meteorology*, Atmospheric Sciences Library, Kluwer Academic Publishers, Dordrecht; Boston, 1988.

Sullivan, R., D. Billesbach, E. Keeler, B. Ermold, and S. Pal, Eddy Correlation Flux Measurement System, doi:10.5439/1025039, 1997a.

Sullivan, R., D. Billesbach, E. Keeler, B. Ermold, and S. Pal, Eddy Correlation Flux Measurement System, doi:10.5439/1025039, 1997b.

Sun, J., Tilt corrections over complex terrain and their implication for CO2 transport, *Boundary-Layer Meteorology*, *124*(2), 143–159, doi:10.1007/s10546-007-9186-5, 2007.

Sun, J., L. Mahrt, R. M. Banta, and Y. L. Pichugina, Turbulence Regimes and Turbulence Intermittency in the Stable Boundary Layer during CASES-99, *Journal of the Atmospheric Sciences*, *69*(1), 338–351, doi:10.1175/JAS-D-11-082.1, 2012.

Sun, J., et al., Review of wave-turbulence interactions in the stable atmospheric boundary layer, *Reviews of Geophysics*, *53*(3), 956–993, doi:10.1002/2015RG000487, 2015.

Svoma, B. M., Difficulties in Determining Snowpack Sublimation in Complex Terrain at the Macroscale, *Advances in Meteorology*, *2016*, 1–10, doi:10.1155/2016/9695757, 2016.

Thomas, C. K., Variability of Sub-Canopy Flow, Temperature, and Horizontal Advection in Moderately Complex Terrain, *Boundary-Layer Meteorology*, *139*(1), 61–81, doi:10.1007/s10546-010-9578-9, 2011.

Tillman, F. D., N. K. Day, M. P. Miller, O. L. Miller, C. A. Rumsey, D. R. Wise, P. C. Longley, and M. C. McDonnell, A Review of Current Capabilities and Science Gaps in Water Supply Data, Modeling, and Trends for Water Availability Assessments in the Upper Colorado River Basin, *Water*, *14*(23), 3813, doi:10.3390/w14233813, 2022.

Trouvilliez, A., F. Naaim-Bouvet, H. Bellot, C. Genthon, and H. Gallée, Evaluation of the FlowCapt Acoustic Sensor for the Aeolian Transport of Snow, *Journal of Atmospheric and Oceanic Technology*, *32*(9), 1630–1641, doi:10.1175/JTECH-D-14-00104.1, 2015.

Turnipseed, A. A., D. E. Anderson, S. Burns, P. D. Blanken, and R. K. Monson, Airflows and turbulent flux measurements in mountainous terrain, *Agricultural and Forest Meteorology*, *125*(3-4), 187–205, doi:10.1016/j.agrformet.2004.04.007, 2004.

UCAR/NCAR-Earth Observing Laboratory, NCAR Integrated Surface Flux System (ISFS), doi:10.5065/D6ZC80XJ, 1990.

Udall, B., and J. Overpeck, The twenty-first century Colorado River hot drought and implications for the future, *Water Resources Research*, *53*(3), 2404–2418, doi:10.1002/2016WR019638, 2017.

Van Der Valk, L. D., A. J. Teuling, L. Girod, N. Pirk, R. Stoffer, and C. C. Van Heerwaarden, Understanding wind-driven melt of patchy snow cover, *The Cryosphere*, *16*(10), 4319–4341, doi:10.5194/tc-16-4319-2022, 2022.

Vickers, D., and L. Mahrt, The Cospectral Gap and Turbulent Flux Calculations, *Journal of Atmospheric and Oceanic Technology*, *20*(5), 660–672, doi:10.1175/1520-0426(2003)20⟨660:TCGATF⟩2.0.CO;2, 2003.

Vionnet, V., G. Guyomarc'h, F. Naaim Bouvet, E. Martin, Y. Durand, H. Bellot, C. Bel, and P. Puglièse, Occurrence of blowing snow events at an alpine site over a 10-year period: Observations and modelling, *Advances in Water Resources*, *55*, 53–63, doi:10.1016/j.advwatres.2012.05.004, 2013.

Virtanen, P., et al., SciPy 1.0: Fundamental algorithms for scientific computing in Python, *Nature Methods*, *17*(3), 261–272, doi:10.1038/s41592-019-0686-2, 2020.

Viviroli, D., H. H. Dürr, B. Messerli, M. Meybeck, and R. Weingartner, Mountains of the world, water towers for humanity: Typology, mapping, and global significance, *Water Resources Research*, *43*(7), 2006WR005,653, doi:10.1029/2006WR005653, 2007.

Vosper, S. B., A. N. Ross, I. A. Renfrew, P. Sheridan, A. D. Elvidge, and V. Grubišić, Current Challenges in Orographic Flow Dynamics: Turbulent Exchange Due to Low-Level Gravity-Wave Processes, *Atmosphere*, *9*(9), 361, doi:10.3390/atmos9090361, 2018.

Vugrin, K. W., L. P. Swiler, R. M. Roberts, N. J. Stucky-Mack, and S. P. Sullivan, Confidence region estimation techniques for nonlinear regression in groundwater flow: Three case studies, *Water Resources Research*, *43*(3), 2005WR004,804, doi:10.1029/2005WR004804, 2007.

Wainwright, H., and K. Williams, LiDAR collection in August 2015 over the East River Watershed, Colorado, USA, doi:10.21952/WTR/1412542, 2017.

Wallace, J. M., and P. V. Hobbs, *Atmospheric Science: An Introductory Survey*, no. v. 92 in International Geophysics Series, 2nd ed ed., Elsevier Academic Press, Amsterdam; Boston, 2006.

Wang, T., et al., How advection affects the surface energy balance and its closure at an irrigated alfalfa field, *Agricultural and Forest Meteorology*, *357*, 110,196, doi:10.1016/j.agrformet.2024.110196, 2024.

Webb, E. K., G. I. Pearman, and R. Leuning, Correction of flux measurements for density effects due to heat and water vapour transfer, *Quarterly Journal of the Royal Meteorological Society*, *106*(447), 85–100, doi:10.1002/qj.49710644707, 1980.

Weigel, A. P., and M. W. Rotach, Flow structure and turbulence characteristics of the daytime atmosphere in a steep and narrow Alpine valley, *Quarterly Journal of the Royal Meteorological Society*, *130*(602), 2605–2627, doi:10.1256/qj.03.214, 2004.

Weigel, A. P., F. K. Chow, M. W. Rotach, R. L. Street, and M. Xue, High-Resolution Large-Eddy Simulations of Flow in a Steep Alpine Valley. Part II: Flow Structure and Heat Budgets, *Journal of Applied Meteorology and Climatology*, *45*(1), 87–107, doi:10.1175/JAM2323.1, 2006.

Weigel, A. P., F. K. Chow, and M. W. Rotach, The effect of mountainous topography on moisture exchange between the "surface" and the free atmosphere, *Boundary-Layer Meteorology*, *125*(2), 227–244, doi:10.1007/s10546-006-9120-2, 2007.

Weisman, R. N., Snowmelt: A two-dimensional turbulent diffusion model, *Water Resources Research*, *13*(2), 337–342, doi:10.1029/WR013i002p00337, 1977.

Whiteman, C. D., *Terrain-Forced Flows*, Oxford University Press, doi:10.1093/oso/9780195132717.003.0018, 2000.

Whiteman, C. D., and J. C. Doran, The Relationship between Overlying Synoptic-Scale Flows and Winds within a Valley, *Journal of Applied Meteorology*, *32*(11), 1669–1682, doi:10.1175/1520-0450(1993)032⟨1669:TRBOSS⟩2.0.CO;2, 1993.

Wieringa, J., Representativeness of Wind Observations at Airports, *Bulletin of the American Meteorological Society*, *61*(9), 962–971, doi:10.1175/1520-0477(1980)061⟨0962:ROWOAA⟩2.0.CO;2, 1980.

Wilczak, J. M., S. P. Oncley, and S. A. Stage, Sonic Anemometer Tilt Correction Algorithms, *Boundary-Layer Meteorology*, *99*(1), 127–150, doi:10.1023/A:1018966204465, 2001.

Xia, Y., D. Mocko, M. Huang, B. Li, M. Rodell, K. E. Mitchell, X. Cai, and M. B. Ek, Comparison and Assessment of Three Advanced Land Surface Models in Simulating Terrestrial Water Storage Components over the United States, *Journal of Hydrometeorology*, *18*(3), 625–649, doi:10.1175/JHM-D-16-0112.1, 2017.

Xiao, M., B. Udall, and D. P. Lettenmaier, On the Causes of Declining Colorado River Streamflows, *Water Resources Research*, *54*(9), 6739–6756, doi:10.1029/2018WR023153, 2018.

Xie, Z., Y. Ma, W. Ma, Z. Hu, G. Sun, and Y. Wang, Analysis of Multiyear Blowing Snow Occurrences in the French Alps, *Journal of Hydrometeorology*, *24*(1), 3–19, doi:10.1175/JHM-D-22-0029.1, 2023.

Yang, K., A. John, D. Shean, J. D. Lundquist, Z. Sun, F. Yao, S. Todoran, and N. Cristea, High-resolution mapping of snow cover in montane meadows and forests using Planet imagery and machine learning, *Frontiers in Water*, *5*, 1128,758, doi:10.3389/frwa.2023.1128758, 2023.

Zardi, D., and C. D. Whiteman, Diurnal Mountain Wind Systems, in *Mountain Weather Research and Forecasting*, edited by F. K. Chow, S. F. De Wekker, and B. J. Snyder, pp. 35–119, Springer Netherlands, Dordrecht, doi:10.1007/978-94-007-4098-3_2, 2013.